DEVELOPMENT AND ASSESSMENT OF ADVANCED R_2^* RELAXOMETRY AND SUSCEPTIBILITY BASED QUANTITATIVE BODY MRI

By

Ante Zhu

A dissertation submitted in partial fulfillment of

the requirements for the degree of

Doctor of Philosophy

(Biomedical Engineering)

at the

UNIVERSITY OF WISCONSIN-MADISON

2019

Date of final oral examination: December 13, 2019

The dissertation is approved by the following members of the Final Oral Committee:

Scott Reeder, Professor, Biomedical Engineering, Medical Physics and Radiology

Diego Hernando, Assistant Professor, Medical Physics, Radiology and Biomedical Engineering

Walter Block, Professor, Biomedical Engineering and Medical Physics

Oliver Wieben, Professor, Medical Physics, Radiology and Biomedical Engineering

Kevin Johnson, Assistant Professor, Medical Physics and Radiology

Abstract

Quantitative magnetic resonance imaging (qMRI) techniques have the potential to enable accurate and reproducible characterization of tissue biophysical properties, with broad research and clinical applications. The development of quantitative imaging biomarkers enables reproducible exams across sites, reduces the subjectivity and variability of qualitative evaluation, leading to standardized, evidence-based clinical diagnosis and treatment decisions. In quantitative body MRI, R_2^* relaxometry and tissue magnetic susceptibility have become important biomarkers in assessing diseases including fibrosis, liver iron overload, inflammation, and hyperoxia-related organ dysfunction. In the liver, however, additional factors have recently emerged that limit the accuracy of R_2^* relaxometry and quantitative susceptibility mapping (QSM) based techniques, including the presence of short T_2^* ($=1/R_2^*$) signals in the liver, and the presence of resolution dependent bias in QSM. In this thesis, an advanced relaxometry technique is developed to characterize the short T_2^* component in the liver and assess its correlation with liver fibrosis. Furthermore, the effect of resolution dependent bias on body QSM is characterized in order to develop accurate and reproducible QSM for the assessment of liver iron overload. Additionally, R_2^* relaxometry and susceptibility based qMRI techniques are highly promising for evaluating the health of the placenta, the organ that mediates the maternal-fetal exchange of nutrients, metabolites, oxygen, and waste. In this thesis, the feasibility and safety of volumetric tracking of super-paramagnetic iron oxide (SPIO) deposition using R_2^* mapping and QSM in ferumoxytol-enhanced MRI for detection of placental inflammation are evaluated in a pregnant rhesus macaque model. Finally, the feasibility of R_2^*-based placental oxygenation mapping is evaluated in both animal and human studies.

Acknowledgements

I would first like to thank my advisors, Dr. Scott Reeder and Dr. Diego Hernando, for their constant support and insight as I pursue my PhD degree. I am very fortunate to have their co-mentorship. Their passion on science, rigorous attitude of research and positive understanding of life always motivate me. Thank you to Dr. Scott Reeder for providing support and seeking sources from the university, industry and the MRI society, for my research and professional development. Thank you to Dr. Diego Hernando for his incredible patience on training me through the day-to-day MRI scans, code debugging, and discussions of research, and the line-by-line paper revision. I have developed into independent, confident and responsible researcher under their guidance. They are the role models, who inspire me to continue working as an MRI scientist and deliver my experience to future engineers and researchers.

Thanks to my thesis committee, Dr. Walter Block, Dr. Oliver Wieben, and Dr. Kevin Johnson for their feedback that has helped progress this work. Special thanks to Dr. Oliver Wieben who has encouraged me to attend and present my works in workshops related to placental MRI. The knowledge I learnt from these workshops and conversations I had with peer collogues shape some placental studies in this thesis. And thanks to Dr. Kevin Johnson for his invaluable advices on the ultrashort echo time pulse sequence and reconstruction which have been used for a majority of projects in this thesis.

Thanks also goes to my fellow liver imaging research program (LIRP) and quantitative imaging methods lab (QIML) lab members and alumni. Special thanks to Dr. Samir Sharma, Dr. Curtis Wiens and Dr. Timothy Colgan. Many works in this thesis are developed based on their MRI pulse sequence, reconstruction algorithm, and phantom. Thank you to Dr. Matthias Muhler

and Dr. Jitka Starekova for supplementing clinic aspects to this thesis. I am also grateful to Dr. David Harris for his assistance with manuscript preparation. Additionally, I would like to thank Yuxin (Annie) Zhang, Nathan Roberts, Huiwen Luo, Collin Buelo, Iñaki Rabanillo Viloria, Tom Batan, Dr. Changqing Wang, Dr. Debra Horng, Ashley Hinrichs, Dr. Gesine Knobloch, Ruiqi Geng, Ruvini Navaratna and Yavuz Muslu, for their friendship and collaboration. Being in the lab is a truly enjoyable experience. I hope the collaboration will continue and the friendship will last long.

I would also like to thank all collaborates in UW U01 Teams, Dr. Dinesh Shah, Dr. Thaddeus Golos, Dr. Sean Fain, Dr. Ian Bird, Dr. Christopher Francois and Sydney Nguyen. Their ideas are incredibly important for the placental projects in this thesis.

During my 4.5 years in UW-Madison, it has been a big pleasure to have the opportunity working with brilliant scientists, talented students, and friendly staff in UW MRI group. I would like to express my appreciation to Dr. Kai Ludwig, Dr. Julia Velikina, Dr. Jean Brittain, Dr. Jorge Jimenez, Dr. Wei Zha, Dr. Fang Liu, Dr. David Mummy, Dr. Leonardo Rivera, Daniel Seiter, Philip Corrado, Pingni Wang, Ruiming Chen and Jeff Kammerman. And thanks to all MRI techs and patient coordinators, Kelli Hellenbrand, Sara John, Jenelle Grogan, Haley Jarvi, Martha Garcia, Molly Ellertson and Frances Theisen, who support this research.

This thesis would not have been possible without the funding support from NIH (grants U01-HD087216, R01-DK117354, R01-DK100651, K24-DK102595, R01-DK083380, R01-DK088925) and research support from GE Healthcare. Thanks to Ann Shimakawa for her insightful suggestions on many MRI pulse sequence problems and Dr. Kang Wang who provides great career guidance. I am also grateful to all supports I obtain from Department of Biomedical Engineering, Radiology and Medical Physics in UW-Madison.

Also, I want to thank my past advisor Dr. Yiping Du who introduced me to the MRI field. I started to learn MR physics, write MR pulse sequence and reconstruction codes when I was in his lab. I had the great experience of collaborating with scientists to build an MR system, which would not be possible without his trust.

Lastly, I want to thank my family, my mom Zhongfeng Xie, dad Deyin Zhu, twin sister Anqi Zhu, brother-in-law Wei Dai and my lovely niece Xi Dai, for their endless love throughout my entire life. They are always by my side for sharing happiness and sorrow. They always trust me and encourage me explore what I like without worries. I know they are very proud of me. I am also very proud of being part of this family. In Chinese metaphor, moon evokes homesick. Moon will always shine on my heart no matter where I will be. I will always be there for you when you need me.

Table of Contents

List of Figures

List of Tables

List of Abbreviations

2D – Two-Dimensional

3D – Three-Dimensional

ACQ – ACQuisition

BH – Breath-held

BMI – Body Mass Index

BOLD – Blood Oxygenation Level Dependent

BW – BandWidth

CP – Patient with Cirrhotic live disease

CR – Coefficient of Repeatability

CSE – Chemical Shift-Encoded

DCE – Dynamic Contrast Enhanced

DISCO – Differential Subsampling with Cartesian Ordering

FA – Flip Angle

FB – Free-Breathing

FOV – Field Of View

FP – Patient with hepatic steatosis live disease

GA – Gestational Age

IACUC – Institution's Animal Care and Use Committee

IL-1β - Interleukin 1 beta

IRB - Institutional Review Board

IT - IL-1β treated

LIC – Liver Iron Concentration

LR – Left-Right

MD_{within} – Within-technique Mean Difference

MEDI – Morphology Enabled Dipole Inversion

MRI – Magnetic Resonance Imaging

MRS – Magnetic Resonance Spectroscopy

N/A – Not Available

NAFLD – Non-Alcoholic Fatty Liver Disease

NASH - NonAlcoholic SteatoHepatitis

No. – Number

NOA – Number of Average

PDFF – Proton Density Fat Fraction

PI – Parallel Imaging

qMRI – Quantitative Magnetic Resonance Imaging

QSM – Quantitative Susceptibility Mapping

RMSE – Root-Mean-Square Error

ROI – Region-Of-Interest

SAR – Specific Absorption Rate

SC – Saline Control

SD – Standard Deviation

SD_{within} – Within-technique Standard Deviation

SGRE - Spoiled GRadient-Echo

SI – Superior-Inferior

SNR – Signal-to-Noise Ratio

SPOIN – SuperParamagnetic Oxide Iron Nanoparticle

SQUID - Superconducting QUantum Interference Device

SSFSE – Single-Shot Fast Spin-Echo

ST2 – Short T_2^*

STD – Standard Deviation

STEAM – STimulated Echo Acquisition Mode

TE – Echo Time

TR – Repetition Time

UC – Untreated Control

UTE – Ultra-short TE

Chapter

1. Introduction

1.1 Specific Aims

Quantitative MRI (qMRI) techniques have the potential to enable accurate and reproducible characterization of tissue biophysical properties. The development of quantitative imaging biomarkers enables reproducible exams across sites, reduces the subjectivity and variability of qualitative evaluation, leading to standardized, evidence-based clinical diagnosis and treatment decisions. In body imaging applications, commonly used and emerging qMRI biomarkers include quantification of contrast agent pharmacokinetics (perfusion), diffusion, elastography, proton density fat fraction (PDFF), relaxometry, and susceptibility, among others.

Quantitative R_2^* relaxometry and susceptibility mapping have become important biomarkers in qMRI, due to their ability to quantify iron, oxygen and macromolecular content of the tissue. By acquiring gradient-echo images at multiple echoes, R_2^* relaxation and susceptibility-induced B_0 field heterogeneities can be encoded and quantified by post-processing. With correction for all relevant confounding factors, these techniques can lead to accurate and reproducible biomarkers. In the body, quantification of short T_2^* signals (ST2) has been investigated to evaluate myocardial fibrosis and skeletal muscle fibrosis ($T_2^*=1/R_2^*$, using T_2^* here as short T_2^* is the main property of this signal component, compared to signal components with relatively long T_2^* like water). In recent years, R_2^* mapping and quantitative susceptibility

mapping (QSM) have been shown to enable assessment of liver iron overload, and iron-based agent deposition in various body organs. Furthermore, R_2^* measurements of blood oxygenation level dependent (BOLD) effects have been shown to enable detection of hyperoxia-related organ dysfunction.

However, additional factors have recently emerged that limit the accuracy of R_2^* relaxometry and QSM based techniques in the liver, including the presence of short T_2^* signals in the liver, and the presence of resolution dependent bias in QSM. Short T_2^* signals, which have not been adequately characterized, may introduce bias and variability in the liver signal modeling at short echo times (TEs). Importantly, these short T_2^* components might be related to fibrosis due to increased collagen contents. Therefore, in this work, we develop an advanced relaxometry technique to characterize the short T_2^* component in the liver and assess its correlation with liver fibrosis, and to determine its impact on liver fat quantification. Further, we will characterize the effect of resolution dependent bias on body QSM in order to develop accurate and reproducible QSM for the assessment of liver iron overload.

In addition, R_2^* relaxometry and susceptibility based qMRI techniques are highly promising for evaluating the health of the placenta, the organ that mediates the maternal-fetal exchange of nutrients, metabolites, oxygen, and waste. In this work, we will evaluate the feasibility and safety of volumetric tracking of super-paramagnetic iron oxide (SPIO) deposition using R_2^* mapping and QSM in ferumoxytol-enhanced MRI for detection of placental inflammation. Additionally, maternal respiratory motion and fetal motion lead to image artifacts and confound R_2^* and B_0 field measurements. We will develop a motion-robust R_2^* and B_0 mapping technique and evaluate the accuracy and reproducibility in placental MRI. Furthermore, previous studies have demonstrated the feasibility of assessing placental oxygenation and placental health using

BOLD R_2^* measurements in pregnant rhesus macaques and pregnant women. In this work, we will evaluate the feasibility of R_2^*-based placental oxygenation mapping.

In this work, we will address the challenges and opportunities with the following aims:

Aim 1. To characterize the short T_2^* signal components of the liver signal, to determine its impact on liver fat quantification and to improve the accuracy of signal modeling in the liver.

Aim 2. To assess the effect of spatial resolution on the accuracy of QSM in the assessment of liver iron overload.

Aim 3. To assess the longitudinal variation of placental R_2^* and susceptibility in ferumoxytol-enhanced MRI for characterizing placental inflammation.

Aim 4. To evaluate the accuracy and repeatability of a motion-robust 2D R_2^* and B_0 field mapping technique in placental MRI.

Aim 5. To investigate the feasibility of quantifying regional placental oxygenation and assessing longitudinal changes in placental oxygenation using R_2^* mapping.

1.2 Background and Significance

Quantitative MRI (qMRI) biomarkers enable non-invasive and objective measurement of tissue properties in health and disease. Although various qMRI techniques rely on different specific acquisition methods and reconstruction algorithms, many qMRI techniques share on a common overall structure: 1) By acquiring images with appropriate MRI imaging parameters, the desired tissue properties are encoded into the data. 2) Parametric maps reflecting these desired tissue properties are then reconstructed by post-processing the acquired images using an appropriate signal model[1]. Due to the enormous flexibility in achievable imaging parameters, MRI enables quantification of multiple biophysical and biochemical parameters[2]. For instance, two

important parameters, R_2^* relaxation time and magnetic susceptibility, which are sensitive to the paramagnetic effects of iron and deoxyhemoglobin, and the macromolecular content of the tissue, are broadly used in qMRI. With correction for all relevant confounding factors, R_2^* and susceptibility have the potential to provide biomarkers that are accurate† and reproducible across sites, vendors, and platforms. In the body, R_2^* mapping and quantitative susceptibility mapping (QSM) have been developed with multiple applications, including the assessment of hepatic iron overload, hyperoxia-related organ dysfunction, and fibrosis[3,4,5]. The significance of the proposed qMRI technical developments with several specific applications is summarized below.

1.2.1 Characterization of a short T_2^* signal component in the liver

Non-alcoholic fatty liver disease (NAFLD) is the most common cause of diffuse liver disease, afflicting an estimated 100 million people in the US alone, and an estimated 1 billion people world-wide[6]. NAFLD can progress from steatosis, the hallmark of NAFLD with abnormal triglycerides accumulation, to nonalcoholic steatohepatitis (NASH), fibrosis (i.e., formation of excessive scar tissue), and even cirrhosis, liver failure and hepatocellular carcinoma. Thus, accurate quantifications of the liver fat content and liver fibrosis are of great interest for early detection of NAFLD and staging the liver disease.

---

† We clarify several terms used in this thesis. The accuracy of a measurement is the degree of closeness of the measurement to the true value. The precision of a measurement is the degree of variability of the measurement in repeated experiments. The precision is measured by reproducibility and repeatability. The reproducibility measures the variation of measurements under different conditions. The repeatability measures the variation of measurements under same conditions[141].

In the liver, the signal acquired for T_2^* relaxometry has been conventionally modeled as arising from two components with relatively long T_2^*, i.e., mobile water and mobile triglycerides, and can be measured using chemical shift-encoded (CSE) multi-echo gradient-echo MRI[7]. Using prior knowledge on the frequency shifts, water and fat can be separated and proton density fat fraction (PDFF), a well-validated biomarker of tissue triglyceride concentration, can be quantified[8]. However, short T_2^* signals, may degrade the accuracy of the conventional liver signal model at short echo times (TEs), potentially confounding CSE-based liver qMRI. Indeed, a recent study by our group performing CSE-based quantification of PDFF at 1.5T demonstrated that the measured liver signal at TEs less than 1 ms was elevated relative to the expected liver signal, resulting in bias on PDFF measurements acquired using short TEs[9]. Although short T_2^* signals have been described in tissues like skeletal muscles and heart[10,11], short T_2^* signals in the liver (ST2) have not been adequately characterized. Importantly, ST2 might be related to fibrosis due to increased collagen contents[10,12]. Thus, characterizing ST2 is necessary for a comprehensive study of its influence on PDFF estimation and its potential correlation with liver fibrosis.

In this work, we will establish a multi-component signal model in the presence of ST2, assess its influence on PDFF estimation in short-TE CSE, preliminarily quantify ST2 in vivo, and assess its correlation with tissue fibrosis. This work will guide future studies on accurate liver signal modeling at short TEs and may enable improved accuracy of PDFF estimations for the detection of NAFLD. This work will also provide an initial characterization on the origin of ST2.

1.2.2 Quantitative susceptibility mapping of liver iron overload

Excess iron accumulation in the body is toxic and can damage organs where iron deposits. Accurate detection and staging of iron overload are needed to inform clinical iron-reducing

treatments based on therapeutic phlebotomy or chelation therapy. Liver iron concentration (LIC, units = mg Fe/g dry liver) is widely considered as the best available measurement for the evaluation of body iron stores[13]. Thus, accurate and reproducible quantification of LIC is highly desirable for longitudinal treatment monitoring of iron overload.

MRI-measured QSM has enormous promise to provide accurate and reproducible measurements of LIC, based on a fundamental property of tissue (i.e., magnetic susceptibility). Susceptibility results in well-characterized B_0 field heterogeneities. These susceptibility-induced B_0 field heterogeneities are encoded in the phase of gradient-echo images in CSE acquisitions and tissue susceptibility can be demodulated from the reconstructed phase maps by post-processing. The accuracy of the image phase, however, has been found to be resolution dependent by different groups[14,15]. Gibbs phenomenon introduces truncation artifacts in phase images with low resolutions, especially in tissue boundaries. Unlike R_2^* and PDFF estimated from signals pixel-by-pixel, the susceptibility estimation is obtained through the deconvolution of the entire phase map[4,14]. Unfortunately, the Gibbs ringing artifacts are disseminated to the entire susceptibility map, while that only affect the tissue boundaries in R_2^* and PDFF maps. Therefore, the spatial resolution may result in confounded estimation of tissue susceptibility. In abdominal QSM, image resolution is often limited due to restricted scan times (e.g., 20-second breath-hold) used to avoid respiratory motion artifacts and the need for a short initial echo time to measure broad range of LIC. Thus, the effect of resolution on the accuracy of liver QSM in assessment of liver iron overload needs to be characterized.

In this work, we will characterize the effect of spatial resolution on the accuracy of QSM in the assessment of liver iron overload. This assessment will guide subsequent optimization of the imaging protocols and reconstruction algorithms for body QSM. Development of an improved

accurate biomarker of LIC, as enabled by this work, may result in improved clinical management including detection, staging, and treatment monitoring of iron overload, and may also result in improved biomarkers needed for clinical trials used in drug development.

1.2.3 Ferumoxytol-enhanced R_2^* mapping and QSM in placental inflammation

Preeclampsia is an inflammatory condition of pregnancy, that can lead to edema, hypertension, seizures and even death. In the pathologies of preeclampsia, altered immune cell (e.g. macrophage) activation and distribution within the placenta may play an important role[16]. Therefore, detection of macrophage densities in the placenta and connected tissues like decidua is needed for studying the pathogenesis and clinical significance of placental inflammation.

Ferumoxytol is a super-paramagnetic iron oxide (SPIO) nanoparticles. It is used as an FDA-approved intravenous iron-based agent for treatment of anemia and can be phagocytosed by macrophages. Importantly, the concentration of ferumoxytol can be assessed by using either R_2^*-based or susceptibility-based MRI techniques[17,18]. A recent study demonstrated the detection of inflammation in the type-1 diabetic pancreas based on ferumoxytol-enhanced MRI[19], indicating the potential for detecting inflammation in multiple organs including the placenta. Therefore, ferumoxytol-enhanced R_2^* mapping and QSM may enable safe and sensitive detection of increased macrophage density in inflammation.

In this study, we will assess the feasibility and safety of ferumoxytol-enhanced R_2^* mapping and QSM of the placenta in rhesus macaques with a placental inflammation model. The proposed ferumoxytol-enhanced qMRI in the placenta may provide a safe, non-invasive method for detection of inflammatory cells in the placenta and connected tissues, enabling assessment of placental inflammation in clinic.

1.2.4 Motion-robust R_2^* and B_0 field mapping

R_2^* and B_0 mapping-based MRI techniques, obtained in a previously proposed 3D CSE-MRI, have been demonstrated to quantify different iron concentrations in SPION phantoms[20], ferumoxytol-enhanced brain MRI[21,22] and body iron deposition[4,20,23]. Ferumoxytol-enhanced R_2^* and B_0 mapping may enable non-invasive and sensitive detection of increased macrophage density in inflammation at the maternal-fetal interface, similar to what has been shown in other studies including inflammation of the central nervous system, aortic walls, kidneys and pancreas[19,24].

Maternal respiratory and fetal motion in the uterus are challenges for imaging the placenta with MRI[25] and their effects should be addressed in order to minimize bias and maximize precision in CSE-MRI. Compared to 3D CSE-MRI which has a long temporal footprint[26] (e.g., 3~5 minutes), 2D CSE-MRI with sequential phase encoding has a short temporal footprint[27] (e.g., ~3 seconds per slice). This strategy is expected to freeze motion or contain the motion effects to a limited number of slices[28,29]. Therefore, free-breathing 2D CSE-MRI may enable reliable R_2^* and B_0 field measurements in the presence of both maternal respiratory motion and fetal motion. However, the accuracy of the free-breathing 2D CSE-MRI technique for quantification of R_2^* and B_0 field in ferumoxytol-enhanced MRI of the placenta has not yet been validated.

In this study, we will evaluate the accuracy and repeatability of 2D CSE-MRI technique for quantification of R_2^* and B_0 field in ferumoxytol-enhanced MRI of the placenta in sedated pregnant rhesus macaques, ferumoxytol phantoms and pregnant women without ferumoxytol administration. Upon successful validation, the motion-robust technique may provide a reliable approach for R_2^*- and B_0 mapping-based evaluation of placental health in ferumoxytol-enhanced placental MRI and BOLD-based placental functional imaging[30].

1.2.5 R_2^* mapping-based placental oxygenation imaging

The placenta, which interfaces with the uterine wall and supports the growth of the fetus, regulates the maternal-fetal exchange of nutrients, oxygen, and waste. Importantly, the placenta is anatomically organized into cotyledons[30,31]. Each cotyledon is supported by its own functional unit (or functional domain) via regional perfusion and oxygenation. Regional placental oxygenation within each domain is product of the maternal blood delivery from the spiral artery and transport in the intervillous space, and oxygen consumption by the fetus and placenta. Deficiencies in placental oxygenation within a domain may impair its function and consequently impede fetal growth. Maternal obesity is associated with increased risk for hypertension and preeclampsia with resulting vascular malformation and reduced placental blood flow, leading to fetal growth restriction[32]. Therefore, assessment of regional differences in blood delivery and oxygenation is needed in order to enable the assessment of different states of placental disease.

Two MRI techniques have shown promise to quantify blood flow and oxygenation in functional perfusion domains of the nonhuman primate placenta: dynamic contrast enhanced (DCE) MRI[31] and R_2^* mapping-based measurement of blood oxygen level-dependent (BOLD) effects[30]. In contrast to the exogenous contrast required for DCE-MRI, R_2^*-based BOLD relies on endogenous contrast. The deoxygenated hemoglobin is paramagnetic whereas oxygenated hemoglobin is not, such that the former causes signal dephasing and thus leads to increased R_2^* of the tissues. Therefore, R_2^*-based BOLD potentially enables the quantification of placental function without the use of contrast agent. In animals, the functional domains identified in R_2^* maps have been found to be spatially correlated to the functional perfusion domains identified in DCE-MRI[31], the imaging standard for quantitative perfusion measurements. In pregnant women, placental R_2^*

mapping has shown promise for longitudinally assessing placental health and predicting pregnancy outcomes[33,34,35,36].

In this work, we will assess regional placental oxygenation using R_2^*-based BOLD measurements in both animal and human studies. This approach will enable quantitative assessment of regional placental function with endogenous contrast, providing a comprehensive assessment of hyperoxia-related placental dysfunction.

1.3 Innovation

This work will develop and optimize novel quantitative MRI techniques and perform characterization and validation of recently proposed techniques. The innovation of this work is five-fold, summarized next:

Characterization of a short T_2^* signal component in the liver. This is the first characterization of liver signals at short TEs using a proposed ultra-short TE CSE (UTE-CSE) acquisitions with radial trajectory, which are capable of capturing the fast decaying signals from ST2 and being motion robust. The application and optimization of radial UTE-CSE in the liver have not been performed before despite the enormous interest and development of liver CSE methods.

Quantitative susceptibility mapping of liver iron overload. This is the first characterization on the effect of anisotropic spatial resolution in liver QSM. The assessment will guide subsequent optimization of the imaging protocols and reconstruction algorithms for body QSM.

Ferumoxytol-enhanced R_2^* mapping and QSM in placental inflammation. This is the first application of ferumoxytol-enhanced MRI for the assessment of placental inflammation. Ferumoxytol-enhanced MRI has been applied in assessment of inflammation in other organs like pancreas but not in the placenta.

Motion-robust R_2^* and B_0 field mapping. This work is the first in vivo assessment of the accuracy of 2D CSE-MRI by comparing to the reference 3D CSE-MRI in the absence of fetal motion, enabled by the unique experiment design which sedates animals.

R_2^* mapping-based placental oxygenation imaging. This work is the first to apply a 3D multi-echo CSE acquisition along with an image registration of R_2^* map to reduce motion-induced image mis-registration in BOLD placental oxygenation imaging. Additionally, this work is the first assessment of longitudinal placental R_2^* and its correlation with pregnancy outcome in obese pregnant women.

1.4 Thesis Outline

In accordance with the aforementioned aims of this work, the thesis is organized as follows:

- **Chapter 2**: A multi-component liver signal model and a UTE-CSE acquisition with optimized echo times are introduced for characterizing the short T_2^* signal in the liver. In vivo experiments are described to demonstrate the consistent existence of ST2 in the liver as well as the confounding effects of ST2 on PDFF quantification using CSE acquisition with short echo times.
- **Chapter 3**: A numerical abdominal phantom is developed to analyze the anisotropic imaging resolution effects on liver QSM. QSM-based liver susceptibility measurements of subjects with suspected liver iron overload using different imaging resolutions are compared. Reduced image resolution is demonstrated to introduce bias on susceptibility estimates in both phantom and in vivo.
- **Chapter 4**: Two hypotheses, 1) maternal ferumoxytol exposure will not lead to increased iron deposition in fetal tissues and 2) ferumoxytol will be taken up by macrophages at

maternal-fetal interface in inflammation with macrophage homing and will be detectable by MRI, are introduced. The preliminary experiments of ferumoxytol-enhanced R_2^* and QSM mapping in a pregnant rhesus macaque model are described to demonstrate the feasibility of longitudinal tracking of iron content in ferumoxytol-enhanced placental MRI.

- **Chapter 5**: A 2D free-breathing CSE-MRI technique which enables motion-robust R_2^* and B_0 field mapping in placental imaging is introduced. Evaluation of the accuracy of R_2^* and B_0 measurements in MRI scans of pregnant animals under general anesthesia and preliminary reader studies on motion artifacts in MRI scans of pregnant women are described. 2D free-breathing CSE-MRI is demonstrated to provide accurate R_2^* and B_0 measurements in ferumoxytol-enhanced placental MRI of animals in the presence of respiratory motion, and motion-robustness in human placental imaging.
- **Chapter 6**: R_2^*-mapping based segmentation of functional domain and quantification of placental oxygenation in individual domains of rhesus macaques, and longitudinal analysis of placental R_2^* over gestational ages in pregnant women are described. Results of oxygenation quantification in different animals and placental R_2^* changes over gestational ages in human subjects are described and compared with previous studies.
- **Chapter 7**: A final summary of this work and discusses on potential future works are described.

Chapter

2. Characterizing a Short T_2^* Signal Component in the Liver Using Ultrashort TE Chemical Shift-Encoded MRI**

2.1 Introduction

Non-alcoholic fatty liver disease (NAFLD) is the most common cause of diffuse liver disease, afflicting an estimated 100 million people in the US alone[37], and an estimated 1 billion people world-wide[38]. Abnormal intracellular accumulation of triglycerides in hepatocytes, steatosis, is the hallmark and the earliest histological feature of NAFLD. In some patients, steatosis can progress to nonalcoholic steatohepatitis (NASH), fibrosis, and even cirrhosis, liver failure and hepatocellular carcinoma[6]. Thus, accurate quantification of liver fat content is of great interest for early detection and treatment monitoring of NAFLD. MR-based chemical shift encoded (CSE-MRI) techniques enable non-invasive measurement of the proton density fat fraction (PDFF), an established non-invasive biomarker of tissue triglyceride concentration[8].

** This work has been published in: Zhu A, Hernando D, Johnson KM, Reeder SB. Characterizing a short T_2^* signal component in the liver using ultrashort TE chemical shift-encoded MRI at 1.5T and 3.0T. *Magn Reson Med.* 2019;82:2032-2045.

CSE-MRI methods have recently emerged as an accurate and reproducible approach for quantification of PDFF in the liver[7,39,40]. The liver signal in gradient-echo images is generally modeled as arising from protons in mobile water and mobile triglycerides. Using prior knowledge of the frequency shifts in the signal model, water and fat can be separated and the signal fraction of each component can be quantified. CSE-MRI methods enable rapid three-dimensional (3D) fat fraction mapping of the whole liver within a single breath-hold, and thus enable a quantitative evaluation of the distribution of liver fat. Advanced CSE-MRI methods correct for multiple confounding factors in the quantification of PDFF, including T_1 bias, noise bias, spectral complexity of fat, T_2^* decay, noise related bias[41,42,43], and phase errors resulting from eddy currents and concomitant gradients[44,45].

The majority of multi-echo CSE-MRI acquisition methods are based on Cartesian k-space sampling patterns and are typically utilized with first echo times exceeding 1 ms. There has, however, been increased interest in acquisitions with shorter first echo time achieved using standard Cartesian CSE-MRI acquisitions with lower spatial resolution[46] or using non-Cartesian ultra-short TE (UTE) acquisitions[47,48,49]. These techniques may enable improved signal-to-noise ratio (SNR) and precision of PDFF estimation, as well as reduce artifacts by using motion-robust radial acquisitions.

However, it is unknown whether the liver signal models typically used with standard CSE acquisitions remain valid for acquisitions with short echo times. Indeed, a recent study using Cartesian CSE-MRI at 1.5T demonstrated that the measured liver signal at echo times less than 1 ms was elevated relative to the expected liver signal, resulting in confounded estimates of PDFF using the short-TE CSE-MRI acquisition[46]. The presence of short-T_2^* signal components in the liver that are only detectable at short echo times would lead to the elevated signal and the

confounded estimation of PDFF in short-TE CSE. Liver signals at short echo times have been measured using UTE imaging[50], however, the quantitative MR properties of the signal components have not been characterized. Therefore, characterization of short T_2^* signal components in the liver is necessary in order to determine their confounding effects on liver PDFF quantification.

In addition, short T_2^* signal components have been reported to provide potential biomarkers of disease in vivo[10,51,52,53]. In tissues such as skeletal muscles and heart, short T_2^* signal components have been suggested to correlate with collagen fibers in diseased models[10,51]. Therefore, characterization of short T_2^* signal components in the liver for disease detection and staging is also of great interest.

The purpose of this study is to characterize the short T_2^* signal components of the liver signal, to determine its impact on liver fat quantification and to improve the accuracy of signal modeling in the liver at short echo times at both 1.5T and 3.0T.

2.2 Theory

2.2.1 Liver signal model for PDFF quantification

Multiple gradient-echo CSE-MRI is commonly used for confounder-corrected PDFF and T_2^* quantification in the liver[54]. The complex liver signal $S(TE_n)$, without considering the signal noise, is generally considered as arising from water and fat, and is expressed as

$$S(TE_n) = \left(W + F \sum_{p=1}^{P} \alpha_p e^{i2\pi \cdot \Delta f_p \cdot TE_n} \right) \cdot e^{-TE_n/T_2^*} \cdot e^{i2\pi \cdot \Delta f_B \cdot TE_n} \cdot e^{i\emptyset_0} \quad (1)$$

where TE_n is the n^{th} echo time, W is the signal amplitude of water, F is the sum of the signal amplitudes of P fat peaks with amplitude α_p and chemical shift frequencies Δf_p, ϕ_0 is the initial

phase, which are assumed to be the same for water and fat, T_2^* is the relaxation rate of water and fat, and Δf_B is the off-resonance frequency due to inhomogeneities of the main magnetic field. The magnitude of the signal $S(TE_n)$ can be expressed as

$$|S(TE_n)| = \left| W + F \sum_{p=1}^{P} \alpha_p e^{i2\pi \cdot \Delta f_p \cdot TE_n} \right| \cdot e^{-TE_n/T_2^*} \quad (2)$$

by taking the amplitude of the complex signal.

Post-processing these multi-echo signals with correcting confounding factors enables measurement of PDFF η, which is defined as

$$\eta = \frac{F}{W + F} \quad (3)$$

i.e., the ratio of unconfounded proton signal from mobile triglycerides to the unconfounded proton signal from mobile triglycerides and mobile water.

2.2.2 Multi-component liver signal model

At short echo times, short T_2^* signals in the liver (ST2) are detectable. Signal components with multiple exponentially decaying rates, with different off-resonance frequencies relative to water, or with different T_1 relaxation rates may exist, as shown in previous studies in other tissues[10,51,52,53]. To simplify the model in this preliminary study, we hypothesized that ST2 is: 1) mono-exponential signal decay; 2) on resonance with water. T_1 relaxation is also not considered. The liver signal $S(TE_n)$ is then modified to a multi-component signal model, described as,

$$S(TE_n) = \left(\left(W + F \sum_{p=1}^{P} \alpha_p e^{i2\pi \cdot \Delta f_p \cdot TE_n} \right) e^{-TE_n/T_2^*} + \zeta e^{-TE_n/T_{2,\zeta}^*} \right) \cdot e^{i2\pi \cdot \Delta f_B \cdot TE_n} \cdot e^{i\emptyset_0} \quad (4)$$

where ζ and $T_{2,\zeta}^{*}$ are the signal amplitudes and the relaxation rate of ST2, separately. The magnitude of the signal can be expressed as

$$|S(TE_n)| = \left| \left(W + F \sum_{p=1}^{P} \alpha_p e^{i2\pi \cdot \Delta f_p \cdot TE_n} \right) e^{-TE_n/T_2^*} + \zeta e^{-TE_n/T_{2,\zeta}^*} \right| \quad (5)$$

by taking the amplitude of the complex signal.

2.2.3 Estimation of the Signal Fraction and T_2^* of ST2

In this study, we seek to characterize the MRI properties of ST2, including $T_{2,\zeta}^{*}$ and the ST2 fraction, which is defined as,

$$\mu = \frac{\zeta}{\zeta + W + F} \quad (6)$$

i.e., the signal fraction of ST2 to all observable signals in the liver. The unknown parameters in the proposed multi-component liver signal model can be estimated by least-squares fitting the complex signals,

$$\hat{\boldsymbol{\theta}} = \arg\min_{\boldsymbol{\theta}} \sum_{n=1}^{N} (S(TE_n, \boldsymbol{\theta}) - S_{measured}(TE_n))^2 \quad (7)$$

where $\hat{\boldsymbol{\theta}} = [\phi_0, \Delta f_B, W, F, \zeta, T_2^*, T_{2,\zeta}^*]$ is the vector of unknown parameters in **Equation 4**, or by fitting the complex signals,

$$\hat{\theta} = \arg\min_{\theta} \sum_{n=1}^{N} (|S(TE_n, \theta)| - |S_{measured}(TE_n)|)^2 \quad (8)$$

where $\hat{\theta} = [W, F, \zeta, T_2^*, T_{2,\zeta}^*]$ is the vector of unknown parameters in **Equation 5**.

2.3 Method

Five sub-studies were performed to characterize ST2 and assess its impact on PDFF, as summarized in the flow diagram in **Figure 1**. In order to initially characterize ST2, the liver signals at short echo times using a proposed UTE-CSE MRI acquisition were obtained in healthy volunteers at 1.5T and 3.0T (**Section 2.3.1**). The feasibility of the proposed multi-component liver signal model and the approximate MRI properties of ST2 were inspected using the in vivo liver signals. In order to assess the effects of ST2 on the accuracy of PDFF estimation at short echo times, we performed in vivo CSE acquisitions for PDFF estimation at 1.5T and 3.0T (**Section 2.3.2**). In order to further validate the impact of ST2 on PDFF estimation, a simulation was performed at 1.5T and 3.0T based on the proposed signal model (**Sections 2.3.3**) and jointly analyzed with in vivo results in **Section 2.3.2**. In order to provide preliminary quantification of the ST2 signals, we optimized echo times used in the proposed UTE-CSE using simulations (**Section 2.3.4**) and performed in vivo validation studies at 3.0T (**Section 2.3.5**).

All in vivo studies were HIPAA compliant and were approved by the local Institutional Review Board (IRB). Healthy subjects and patients were recruited and imaging was performed after obtaining informed written consent. Exclusion criteria included subjects with iron overload, subjects injected with gadolinium-based contrast agent within the past two weeks, or subjects ever injected with ferumoxytol-based contrast agent, in order to avoid any potential confounding effects on measurements of ST2. MR images were obtained on clinical 1.5T MRI systems (Signa HDxt and Optima MR450w, GE Healthcare, Waukesha, WI) and a clinical 3.0T MRI system (Discovery MR 750, GE Healthcare, Waukesha, WI).

Given that the PDFF estimation using CSE-MRI is sensitive to phase errors especially at short echo times[55], the magnitude of signals was used in estimation of in vivo PDFF and

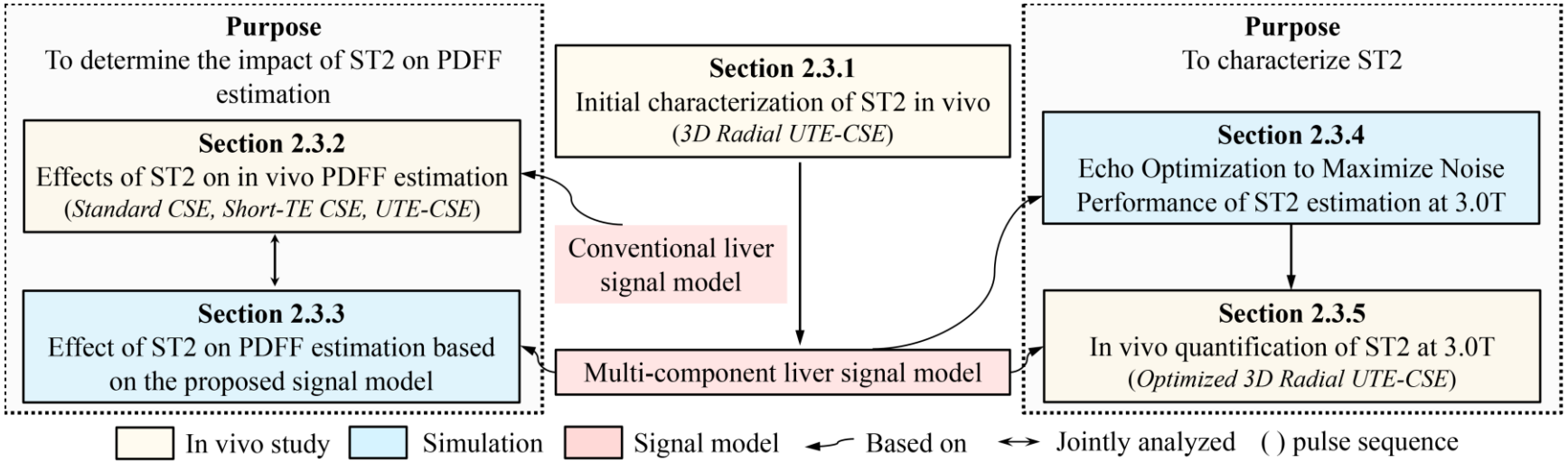

Figure 1. Flow chart of the liver short T_2^* studies. The flow diagram of the five experiments in this work, including three sets of in vivo studies (yellow boxes) and two sets of simulations (blue boxes) under the two purposes of this work. A multi-component liver signal model (red box), which was based on the observed in vivo results in Section 2.3.1, was proposed and used as the signal model in Sections 2.3.3, 2.3.4 and 2.3.5. The conventional liver signal model was used in Sections 2.3.2. MRI pulse sequence used in each of the three in vivo studies were listed in the parentheses.

quantification of ST2 signals. However, using the complex signals has gained increased attention due to better noise performance. Therefore, we also analyzed the PDFF estimation in simulations (**Section 2.3.3**) with the liver complex signal model.

2.3.1 Initial characterization of ST2 in vivo

In order to perform initial characterization of ST2, healthy subjects were recruited and imaged at 1.5T and 3.0T using 3D radial UTE-CSE[48,49] with a multi-echo acquisition. Raw data were acquired during end expiration using a previously described adaptive respiratory compensation method, with a 50% acceptance window[49]. A minimum phase Shinnar-Le Roux radiofrequency pulse[49] with a duration of 112 μs and bandwidth of 50 kHz was used for selective excitation. A single echo was acquired after each radiofrequency excitation for each TR, using real time randomization of the echo times to reduce the effects of eddy currents[53]. The same radial k-space trajectory was sampled at multiple echo times in a randomized order to minimize motion related artifacts[49]. 10,000 radial projections were sampled for each echo. Other imaging parameters are listed in **Table 1**. In addition, a $MnCl_2$-doped water phantom with a known PDFF of 0% was imaged at 1.5T and 3.0T, using the same in vivo UTE-CSE acquisitions, to assess the signal fluctuation in UTE acquisitions[53].

UTE-CSE images were reconstructed offline using an adaptive coil combination technique[56]. The liver signals were measured in a ~3.5 cm^2 circular region-of-interest (ROI) in the right lobe of the liver placed to avoid large blood vessels and bile ducts. The magnitude signal was averaged first and then fit to the proposed multi-component liver signal model (**Equation 5**) to estimate the ST2 fraction and $T_{2,\zeta}^*$.

Table 1. Imaging parameters and subjects of short T_2^* studies.

	Cohorts		# TE	TE (ms)	TR (ms)	FA (°)	ACQ resolution(mm^3)	Scan Time
Section 2.3.1 Initial characterization of ST2 in vivo	Healthy (N=6 at 1.5T, N=6 at 3.0T)	**1.5T & 3.0T**						
		Radial UTE-CSE	11	0.1, 0.2, 0.4, 0.6, 0.8, 1.0, 2.0, 3.0, 4.0, 5.0, 6.0	8.7	4	1.2×1.2×1.2	~30 mins (FB)
Section 2.3.2 Effect of ST2 on in vivo PDFF estimation	Healthy (N=14[×]) Steatosis (N=5)	**1.5T**						
		Standard CSE	6	$TE_{init}/\Delta TE$ = 1.2/2.0	14.5	5	1.6×2.3×8 or 2.1×2.8×8	21 s (BH)
		Short-TE CSE	6	$TE_{init}/\Delta TE$ = 0.7/1.3	8.6	5	1.3×1.9×8 or 3.7×2.7×10	19 s (BH)
	Healthy (N=6[×])	Radial UTE-CSE	11	0.1, 0.2, 0.4, 0.6, 0.8, 1.0, 2.0, 3.0, 4.0, 5.0, 6.0	8.7	4	1.2×1.2×1.2	~30 mins (FB)
	Healthy (N=6[×]) Steatosis (N=5) Cirrhosis (N=5)	**3.0T**						
		Standard CSE	6	$TE_{init}/\Delta TE$ = 1.2/1.0	8.0	3	1.6×2.2×8	18 s (BH)
		Short-TE CSE	8	$TE_{init}/\Delta TE$ = 0.6/1.0	8.0	3	2.8×2.5×8	17 s (BH)
		Radial UTE-CSE	11	0.10, 0.15, 0.20, 0.25, 1.0, 2.0, 3.0, 4.0, 5.0, 6.0, 7.0	9.6	4	1.6×1.6×1.6	~35 mins (FB)
				or				
			11	0.1, 0.2, 0.4, 0.6, 0.8, 1.0, 2.0, 3.0, 4.0, 5.0, 6.0	8.7	4	1.6×1.6×1.6	~30 mins (FB)
Section 2.3.5 In vivo quantification of ST2 at 3.0T	Healthy (N=6[×]) Steatosis (N=5[+]) Cirrhosis (N=5[#])	**3.0T**						
		Optimized UTE-CSE	11	0.10, 0.15, 0.20, 0.25, 1.0, 2.0, 3.0, 4.0, 5.0, 6.0, 7.0	9.6	4	1.6×1.6×1.6	~35 mins (FB)

[×]Data from the same 6 healthy subjects imaged at 1.5T in Section 2.3.1; [+]Data from the same 5 patients with steatosis imaged at 3.0T in Section 2.3.2; [#]Data form the same 5 patients with cirrhosis in Section 2.3.2; UTE: ultrashort TE; CSE: chemical shift-encoded; FA: flip angle; ACQ: acquisition; BW: bandwidth; FB: free-breathing; BH: breath-held

2.3.2 Effect of ST2 on in vivo PDFF estimation

In order to assess the effect of ST2 on the accuracy of PDFF estimation at short echo times, healthy subjects and patients with hepatic steatosis (but no cirrhosis) were recruited and imaged at 1.5T and 3.0T using three CSE-MRI acquisitions with different echo time combinations. Two single-breath-hold 3D CSE-MRI Cartesian acquisitions with relatively long echo times (Standard CSE) and with a short initial echo time (Short-TE CSE), and a free-breathing radial UTE-CSE acquisition were obtained. The acquisition trajectory and respiratory gating were the same as in the UTE-CSE in **Section 2.3.1**. Imaging parameters of the three CSE-MRI acquisitions are listed in **Table 1**. A single-voxel multi-TE stimulated echo acquisition mode (STEAM) MR spectroscopy[57] (MRS) acquisition was also obtained as the reference for a T_2-corrected T_1-independent PDFF estimate. Imaging parameters of STEAM-MRS included: prescribed within the right lobe of the liver to avoid large vessels or bile ducts and the dome of the liver, five echoes with $TE_{init}/\Delta TE$ = 10/5 ms, 3500 ms TR, 20×20×20 mm^3 or 24×24×24 mm^3 voxel size, 1 average, ±2.5 kHz spectral width, 2048 readout points, and 5 ms mixing time.

PDFF was calculated twice in each CSE acquisition using a CSE reconstruction[6], either with all echoes or excluding short echoes (<1 ms). PDFF was quantified by measuring the average PDFF in the ROI co-localized with the MRS voxel. Measurements of PDFF made with CSE-MRI and MRS were compared using Bland-Altman analysis. In addition, PDFF was also estimated in the UTE-CSE acquisition of the $MnCl_2$-doped water phantom in **Section 2.3.1** to assess bias on PDFF estimation due to signal fluctuations in UTE acquisitions[53].

2.3.3 Effect of ST2 on PDFF estimation based on the proposed signal model

The effects of ST2 on PDFF estimation depend on the signal fraction of ST2, the relaxation time $T_{2,\zeta}^*$, the chemical shift frequency of the fat at different field strengths, and also the choice of echo times. We performed simulation to jointly analyze the bias on PDFF introduced by the presence of ST2 at 1.5T and 3.0T, along with the in vivo study in **Section 2.3.2**. We estimated PDFF and compared with the true PDFF, using signals including ST2 (**Equations 5 and 6**). The simulation parameters include: six-peak fat spectrum[58] with frequency shift = [0.6, -0.5, -1.95, -2.6, -3.4, -3.8] ppm and relative amplitude = [4.7, 3.9, 0.6, 12, 70, 8.8]%, T_2^* = 25 ms for both water and fat, PDFF = [0%, 10%], $T_{2,\zeta}^*$ = 0.01~1.00 ms, ST2 fraction = 10% retrospectively used based on the preliminary in vivo estimation in **Section 2.3.1**, and no noise. Echo times of three combinations from in vivo acquisitions in **Section 2.3.2** were used: 1) Standard CSE: six echoes, $TE_{init}/\Delta TE$ = 1.2/2.0 ms; 2) Short-TE CSE: six echoes, $TE_{init}/\Delta TE$ = 0.7/1.3 ms; 3) UTE-CSE: eleven echoes, TE = [0.1, 0.2, 0.4, 0.6, 0.8, 1.0, 2.0, 3.0, 4.0, 5.0, 6.0] ms. The signal at each echo was generated using **Equations 5 and 6**. PDFF was then estimated using **Equations 2 and 3** and compared with the true PDFF.

2.3.4 Echo Time Optimization to Maximize Noise Performance of ST2 estimation

Optimization of echo times has been shown to improve the noise performance of quantitative estimates in CSE-MRI techniques[59]. In this work, echo times were optimized to reduce minimize the maximum bias and the maximum root-mean-square error (RMSE) of the estimated ST2 fraction and $R_{2,\zeta}^*$ ($R_{2,\zeta}^*$=1/ $T_{2,\zeta}^*$) over the combinations within a range of ST2 fraction and

$T_{2,\zeta}^*$. A Monte-Carlo simulation with 1000 trials was used with parameters including: $T_{2,\zeta}^*$ = 0.20-0.33 ms, ST2 fraction = [5.0, 10.0, 15.0]%, PDFF = [0, 10.0, 20.0, 30.0, 40.0]%, T_2^* = 50 ms. The ranges of $T_{2,\zeta}^*$ and the ST2 fraction were retrospectively chosen based on our preliminary in vivo estimation at 3.0T described in **Section 2.3.1** above. A SNR of 200 was used, which was similar to the SNR measured using the ROI-based approach (i.e., signal average first and then fit) with the in vivo data as stated in **Section 2.3.1**. An upper bound of 1.25 ms and a lower bound of 0.07 ms were applied on $T_{2,\zeta}^*$ estimation to stabilize the estimation process.

Eleven echo images were acquired to restrict acquisition time within 40 minutes. The potential choices of echo time combinations were narrowed down in this work with the following constraints: 1) eleven echoes were divided into two groups, one with short echo times (<1 ms) for capturing ST2 signals, one with relative long echo times (≥1 ms) for quantifying water and fat, 2) echo spacing was kept the same in individual echo time groups, 3) the first echo time in short echo time group was fixed to be the minimum echo time achievable with the pulse sequence (TE_0 = 100 us), 4) the first echo time in the long echo time group was fixed to be 1 ms, which is a standard first echo time used for liver CSE imaging at 3.0T. The four terms lead to an echo time combination,

$$TE = \begin{cases} TE_0 + \Delta TE_s \cdot n, & 0 \le n < N, \\ 1\ ms + \Delta TE_l \cdot (n - N), & n \le N \le 11. \end{cases} \quad (9)$$

where ΔTE_s (0.02 ms ≤ ΔTE_s ≤ 0.23 ms) and ΔTE_l (0.5 ms ≤ ΔTE_l ≤ 1.5 ms) are the echo spacing in short and long echo time groups, respectively, N ($3 \le N \le 7$) is the number of short echo times.

2.3.5 In vivo quantification of ST2 at 3.0T

In order to investigate whether ST2 might correlate with the presence of liver disease, especially collagen fibers as has been found in diseased models of other tissues[10,51], we preliminarily quantified the signal fraction and T_2^* of ST2 and compared the quantification between healthy and cirrhotic livers. Three cohorts consisting of healthy subjects, patients with liver cirrhosis, and patients with hepatic steatosis (but no cirrhosis) were recruited and imaged at 3.0T using a 3D UTE-CSE acquisition with the optimized echo times in simulation (**Section 2.3.4**). The acquisition trajectory and respiratory gating were the same as in the UTE-CSE in **Section 2.3.1**. Imaging parameters are listed in **21**. The liver signals were measured and the ST2 fraction and $T_{2,\zeta}^*$ were estimated in the same way as that in **Section 2.3.1**. The average values of the ST2 fraction and $T_{2,\zeta}^*$ in three cohorts were compared. The *P* value was calculated by using a two-tailed Mann-Whitney *U* test, and $P<0.05$ was considered significant.

2.4 Results

2.4.1 Initial characterization of ST2 in vivo

Six healthy subjects were recruited and imaged at 1.5T and 3.0T. **30** shows the UTE-CSE images and plots of the liver signal intensity of two different healthy subjects at 1.5T (top) and 3.0T (bottom). No obvious motion artifacts are shown in the UTE multi-echo images. The measured liver signals at echo times less than 1 ms (hollow circles) are elevated and show faster decay rate than the signals at echo times larger than 1 ms, compared with the extrapolated signals of water and fat from **Equation 3** using echo times larger than 1 ms (solid circles). In the $MnCl_2$-

doped water phantom, the measured signals at short echo times less than 1ms are not elevated in the UTE-CSE acquisition (**Figure 3**), demonstrating that the elevated liver signal at short echoes originate from the tissue itself and not from acquisition artifacts.

In the six volunteers as shown in **Table 2**, a ST2 fraction of 9.6±1.8% with a $T_{2,\zeta}^{*}$ of 0.21±0.08 ms were observed at 3.0T, and a ST2 fraction of 14.2±1.1% with a $T_{2,\zeta}^{*}$ of 0.80±0.24 ms were observed at 1.5T. The ST2 fraction of subjects estimated at 1.5T are all higher than that estimated at 3.0T with $P<0.01$. $T_{2,\zeta}^{*}$ at 1.5T are all longer than that at 3.0T with $P<0.01$.

2.4.2 Effect of ST2 on in vivo PDFF estimation

Fourteen healthy subjects and five patients with suspected hepatic steatosis were recruited and imaged at 1.5T, and six healthy subjects, five patients with suspected liver cirrhosis and five patients with hepatic steatosis were recruited and imaged at 3.0T. Portions of the data at 1.5T have been previously reported[46]. At 1.5T, six healthy subjects out of the fourteen healthy subjects were imaged with 3D radial UTE-CSE.

The plots of the liver signal intensity of a healthy subject acquired in standard CSE and short-TE CSE acquisitions at 1.5T are shown in **Figure 4**. **Figure 5** and **Figure 6** depict the Bland-Altman analysis of fat quantification using CSE-MRI compared to MRS at 1.5T and 3.0T, respectively.

At 1.5T, PDFF estimation is accurate using all six echoes or when the first echo is discarded in standard CSE (Figure 5A). A 1.7% positive bias of the estimated PDFF ($P<0.01$) is observed when all echoes are used in short-TE CSE ("×" in Figures 5B and 5C). This bias can be reduced by discarding the first echo in short-TE CSE (diamond in Figures 5B and 5C). In addition, a 3.4%

positive bias of the estimated PDFF (P<0.01) is observed in UTE-CSE using all echoes ("×" in Figure 5D) and the bias can be reduced by discarding the short echoes (diamond in Figure 5D).

At 3.0T, however, the PDFF estimation in short-TE CSE is not significantly different when all echoes are used or when the first echo is discarded (Figures 6B and 6C). A bias of 0.9%, respect to PDFF estimated in STEAM-MRS, is observed and reduced to 0.2% in standard CSE using all six echoes and when the first echo is discarded, respectively (Figure 6A). In UTE-CSE, a 3.2% positive bias of the estimated PDFF (P<0.01) is also observed using all echoes ("×" in Figure 6D) and the bias can be reduced by discarding the short echoes (diamond in Figure 6D).

The plots of the liver signal intensity of a healthy subject acquired in standard CSE and short-TE CSE acquisitions at 1.5T are shown in **Figure 4**. **Figure 5** and **Figure 6** depict the Bland-Altman analysis of fat quantification using CSE-MRI compared to MRS at 1.5T and 3.0T, respectively.

At 1.5T, PDFF estimation is accurate using all six echoes or when the first echo is discarded in standard CSE (Figure 5A). A 1.7% positive bias of the estimated PDFF (P<0.01) is observed when all echoes are used in short-TE CSE ("×" in Figures 5B and 5C). This bias can be reduced by discarding the first echo in short-TE CSE (diamond in Figures 5B and 5C). In addition, a 3.4% positive bias of the estimated PDFF (P<0.01) is observed in UTE-CSE using all echoes ("×" in Figure 5D) and the bias can be reduced by discarding the short echoes (diamond in Figure 5D).

At 3.0T, however, the PDFF estimation in short-TE CSE is not significantly different when all echoes are used or when the first echo is discarded (Figures 6B and 6C). A bias of 0.9%, respect to PDFF estimated in STEAM-MRS, is observed and reduced to 0.2% in standard CSE using all six echoes and when the first echo is discarded, respectively (Figure 6A). In UTE-CSE, a 3.2%

positive bias of the estimated PDFF (P<0.01) is also observed using all echoes ("×" in Figure 6D) and the bias can be reduced by discarding the short echoes (diamond in Figure 6D).

In the $MnCl_2$-doped water phantom, the estimated PDFF is 0.01% at 1.5T and -0.06% at 3.0T using all echoes, and 0.05% at 1.5T and 0.33% at 3.0T discarding the short echoes in UTE-CSE (**Figure 7**). It demonstrates that the bias of the estimated in vivo PDFF using all echoes in UTE-CSE is due to factors other than eddy currents, and originates from short echo time signals from the tissue itself.

2.4.3 Effect of ST2 on PDFF estimation based on the proposed signal model

Figure 8 shows the simulation results of the bias on PDFF with a true PDFF of 0% (solid lines and dashed lines) or 10% (lines with cross and solid circles) at 1.5T (Figure 8A, 8C) and 3.0T (Figure 8B, 8D) in the presence of ST2 with a fraction of 10%. Using standard CSE and short-TE CSE (Figure 8A, 8B), the bias in PDFF estimates increases as $T_{2,\zeta}^*$ increases at both 1.5T and 3.0T, i.e., when the ST2 signals decay slower, leading to more residual signals at longer echo times used for water and fat estimation. At 1.5T, the bias is eliminated when estimating PDFF using long echo times, i.e., standard CSE (dashed lines and lines with solid circles), compared to the estimations using short echo times, i.e., short-TE CSE (solid lines and lines with cross). At 3.0T, however, the bias in standard CSE and short-TE CSE is smaller than that at 1.5T for a given $T_{2,\zeta}^*$. Moreover, the bias in standard CSE (dashed lines and lines with solid circles) is not substantially reduced compared to the short-TE CSE (solid lines and lines with cross).

In UTE-CSE (Figure 8C and 8D), the bias on PDFF is observed using all echo times (solid lines and lines with cross) and can be substantially reduced in the estimations using echo times

longer than 1 ms (dashed lines and lines with solid circles). The effects of ST2 on PDFF estimation based on the complex signal model is shown in **Figure 9**.

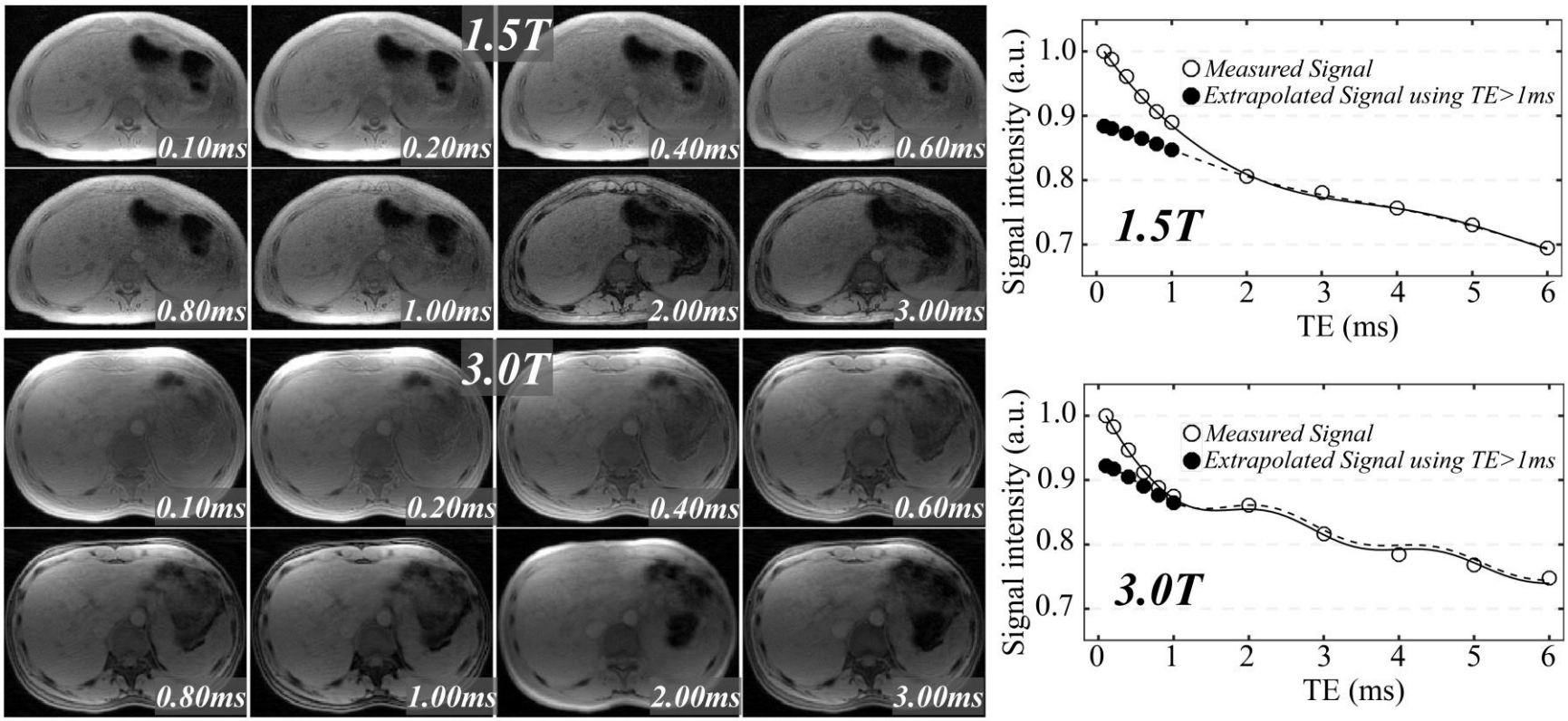

Figure 2. The liver signal of two different healthy volunteers. The liver signal of two different healthy volunteers at multiple echo times in UTE-CSE imaging (upper left: 1.5T, lower left: 3.0T) shows dramatically faster decaying rate at echo times less than 1ms than the decaying rate of water and fat signals echo times larger than 1ms at both 1.5T (upper right) and 3.0T (lower right), suggesting the presence of an unknown liver signal component with a short T_2^* value. A ST2 fraction of 17.3%, a $T_{2,\zeta}^*$ of 0.87 ms, a fat fraction of 0.8% and a T_2^* of 39.0 ms were estimated in the subject at 1.5T based on the proposed liver signal model (**Equation 3**). A ST2 fraction of 10.5%, a $T_{2,\zeta}^*$ of 0.53 ms, a fat fraction of 1.9% and a T_2^* of 33.0 ms were estimated in the subject at 3.0T based on **Equation 3**.

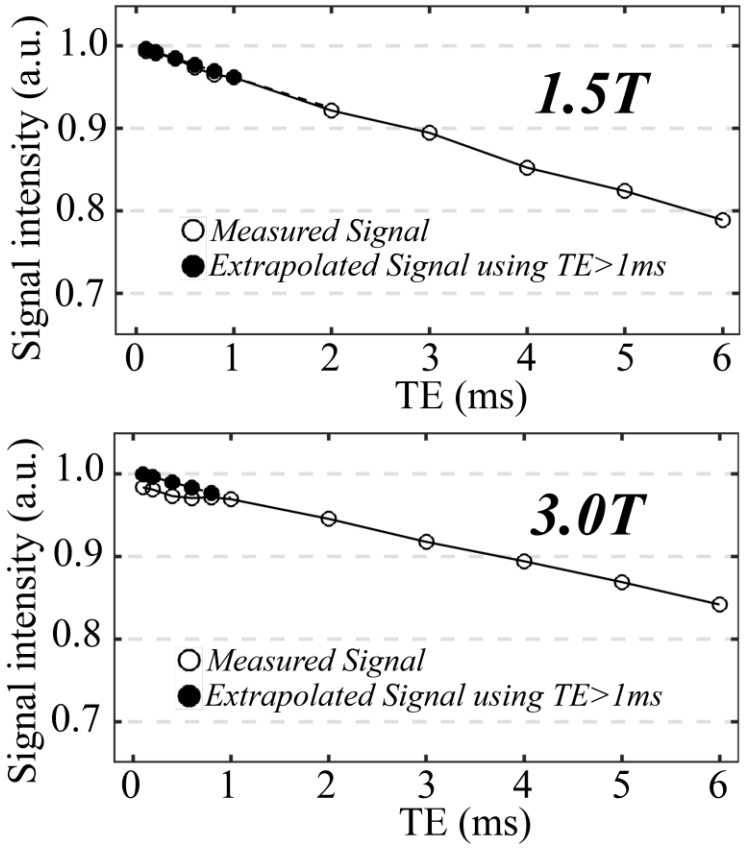

Figure 3. The UTE-CSE signal of a water phantom. The signal intensity of a $MnCl_2$-doped (0.2 mM) water phantom in radial UTE-CSE acquisition imaged at both 1.5T (upper) and 3.0T (lower). The measured signals at short echo times (hollow circles) are not elevated compared to the extrapolated signals of water and fat using echo times larger than 1 ms (solid circles). In the $MnCl_2$-doped water phantom we did not observe elevated signals at short echoes suggesting that factors other than eddy currents, likely originating from the tissue itself, resulted in the elevated in vivo liver signal at short echoes we observed (**30**). The image parameters of the radial UTE-CSE acquisition are those used in the in vivo UTE-CSE acquisitions in **Section 2.3.1**.

Table 2. Subjects information and ST2 quantification. Subjects information and the estimation of the ST2 signals at 1.5T and 3.0T.

Subject ID	Gender	Age (year)	Cirrhosis Stage	ST2 Fraction 3.0T Optimized TE^{+} (%)	$T_{2,\zeta}^{*}$ 3.0T^{+} (ms)	ST2 Fraction 3.0T$^{\times}$ (%)	$T_{2,\zeta}^{*}$ 3.0T$^{\times}$ (ms)	ST2 Fraction 1.5T$^{\times}$ (%)	$T_{2,\zeta}^{*}$ 1.5T$^{\times}$ (ms)
CP1	F	55	A	5.8	0.25	N/A	N/A	N/A	N/A
CP2	M	57	B	4.9	0.13	N/A	N/A	N/A	N/A
CP3	M	60	A	9.3	0.16	N/A	N/A	N/A	N/A
CP4	F	70	B	7.7	0.24	N/A	N/A	N/A	N/A
CP5	F	51	B	7.4	0.23	N/A	N/A	N/A	N/A
mean±std				7.0±1.7	0.20±0.05				
FP1	F	59	N/A	5.5	0.08	N/A	N/A	N/A	N/A
FP2	M	58	N/A	9.1	0.10	N/A	N/A	N/A	N/A
FP3	F	29	N/A	6.3	0.10	N/A	N/A	N/A	N/A
FP4	M	57	N/A	8.6	0.13	N/A	N/A	N/A	N/A
mean±std				7.4±1.7	0.10±0.02				
H1	F	23	N/A	10.7	0.25	11.0	0.29	14.0	0.99
H2	M	39	N/A	7.3	0.14	7.6	0.11	13.8	0.48
H3	M	33	N/A	9.2	0.23	7.0	0.16	15.2	0.65
H4	F	26	N/A	10.7	0.28	11.1	0.32	15.9	1.14
H5	M	31	N/A	11.2	0.22	10.3	0.18	13.2	0.67
H6	F	26	N/A	8.6	0.23	10.9	0.23	13.3	0.84
mean±std				9.6±1.5	0.23±0.05	9.6±1.8	0.21±0.08	14.2±1.1	0.80±0.24

$^{\times}$Data in Section 2.3.1; $^{+}$Data in Section 2.3.5; CP, patient with diagnosed cirrhotic liver disease; FP, patient with hepatic steatosis (but no cirrhosis); F, female; M, male; H, healthy volunteer; N/A, not available; std, standard deviation

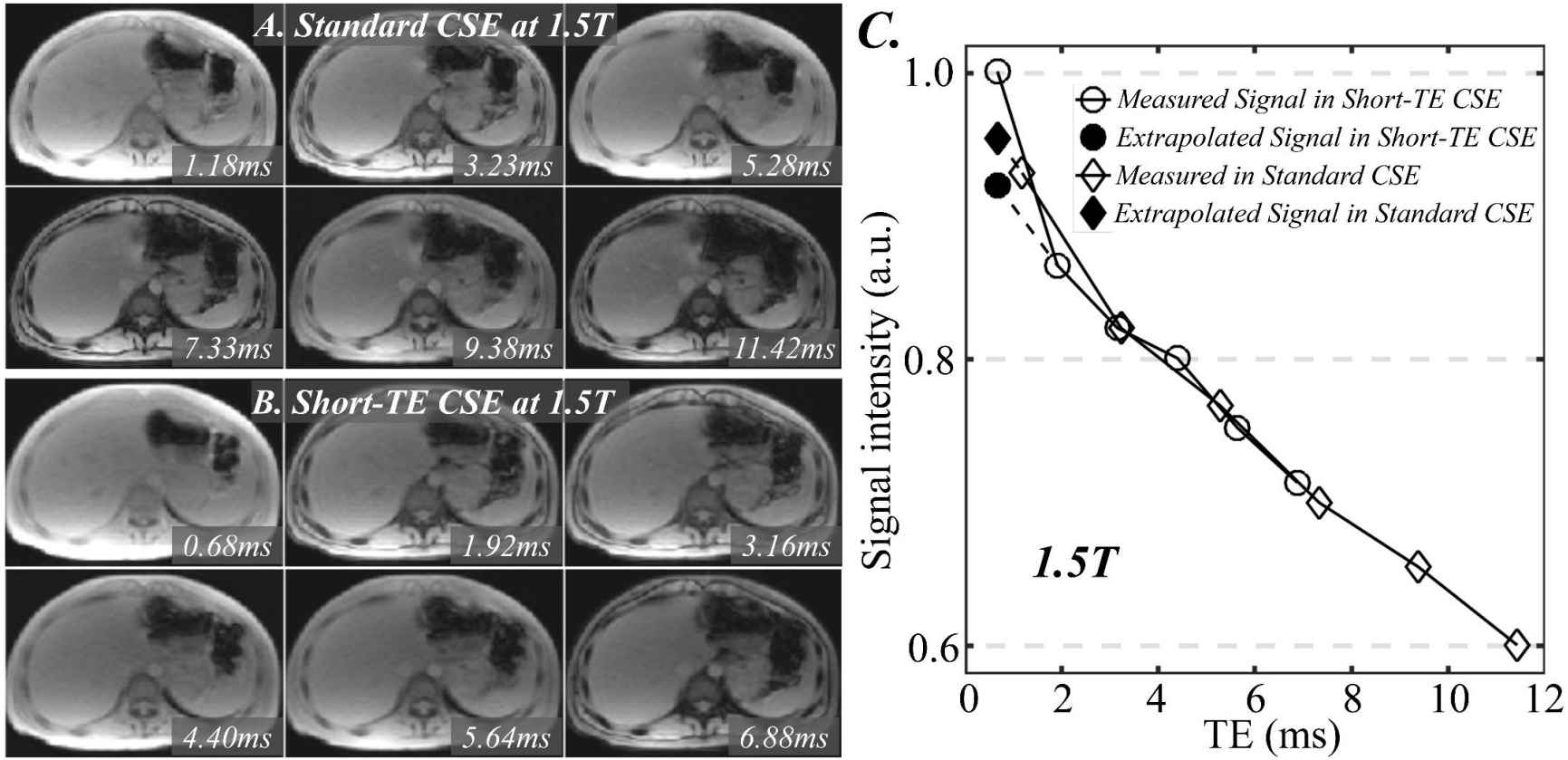

Figure 4. Liver CSE signals of a healthy subject at 1.5T. At 1.5T, representative images of a healthy subject at multiple echo times from standard CSE (A) and short-TE (B) acquisitions and the liver signals across echo times (C). The measured signal at the first TE in short-TE CSE (hollow circle) is elevated compared to the extrapolated signal of the water and fat using long echo times based on **Equation 2** (solid circle), suggesting the presence of a rapidly decaying signal component. The images are from the same subject shown in **30** at 1.5T. The elevated signals at short echo times in short-TE CSE, compared to the extrapolated signal of water and fat using long echo times based on **Equation 2** are consistent with the signal elevation at the first echo time in UTE-CSE in **30**.

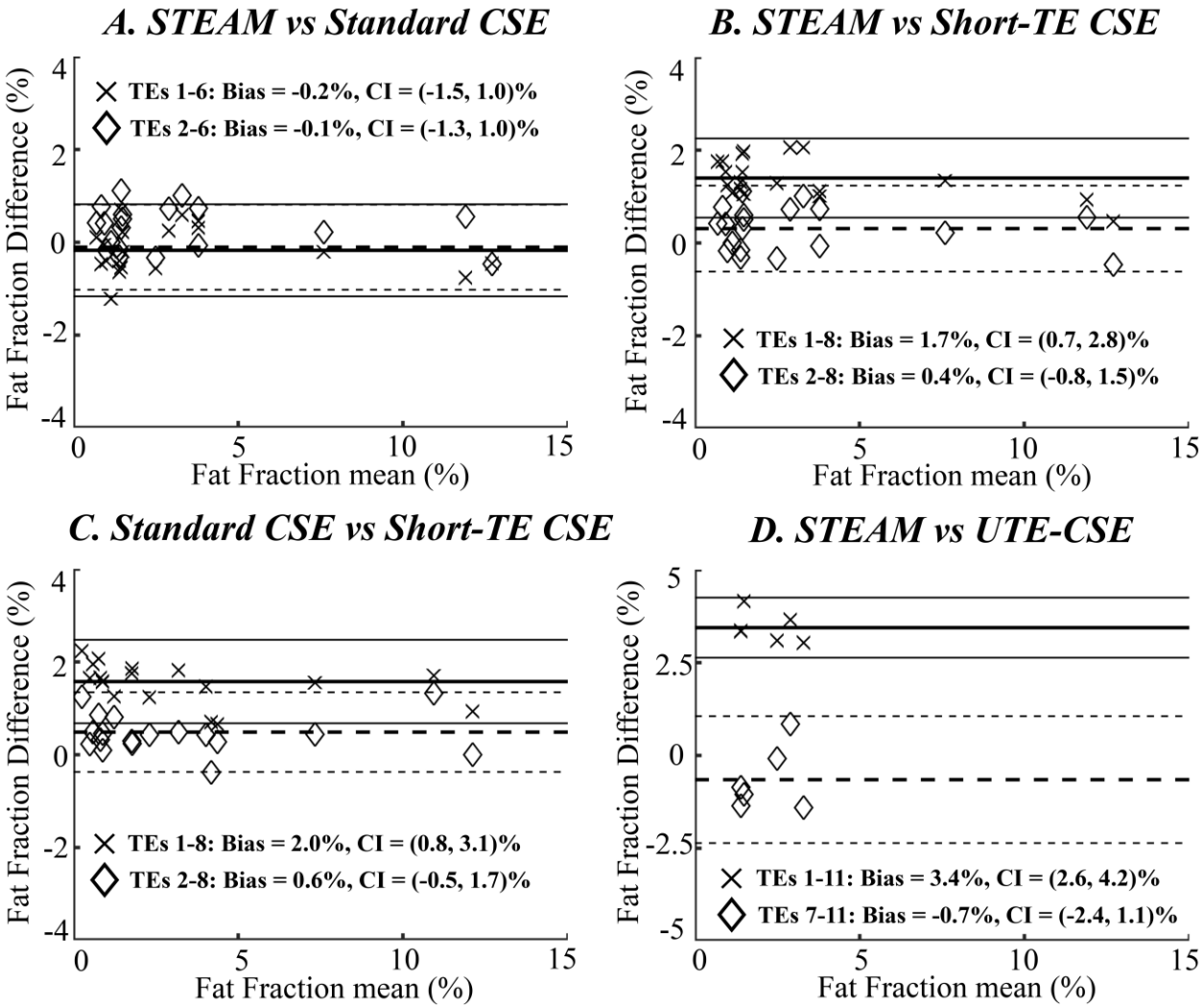

Figure 5. Bland-Altman analysis on PDFF estimation at 1.5T. At 1.5T, Bland-Altman analysis on PDFF estimation shows a positive bias of the estimated PDFF using all echoes in both short-TE CSE ("×" in B and C) and UTE-CSE ("×" in D) and can be eliminated by discarding the short echoes (diamond in B and D). The fat estimation is accurate using standard CSE using all six echoes or when the first echo is discarded (A).

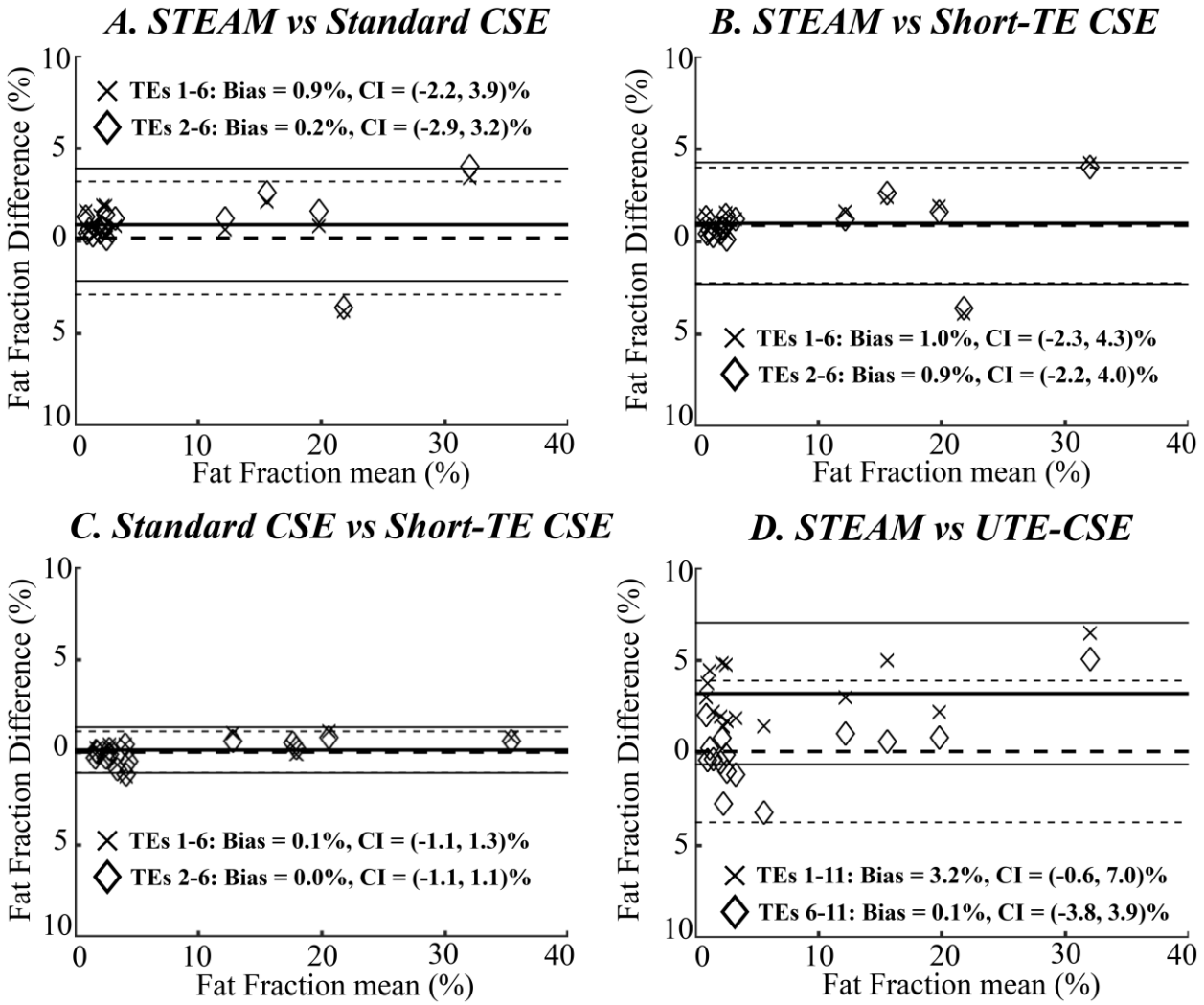

Figure 6. Bland-Altman analysis on PDFF estimation at 3.0T. At 3.0T, Bland-Altman analysis on PDFF estimation shows a positive bias of the estimated PDFF using all echoes in UTE-CSE ("×" in D) and can be eliminated by discarding the short echoes (diamond in D), while the accuracy of the estimated PDFF in short-TE CSE is not improved by discarding the short echoes (B and C). In standard CSE (A), a small bias is observed and reduced in standard CSE using all six echoes and when the first echo is discarded, respectively

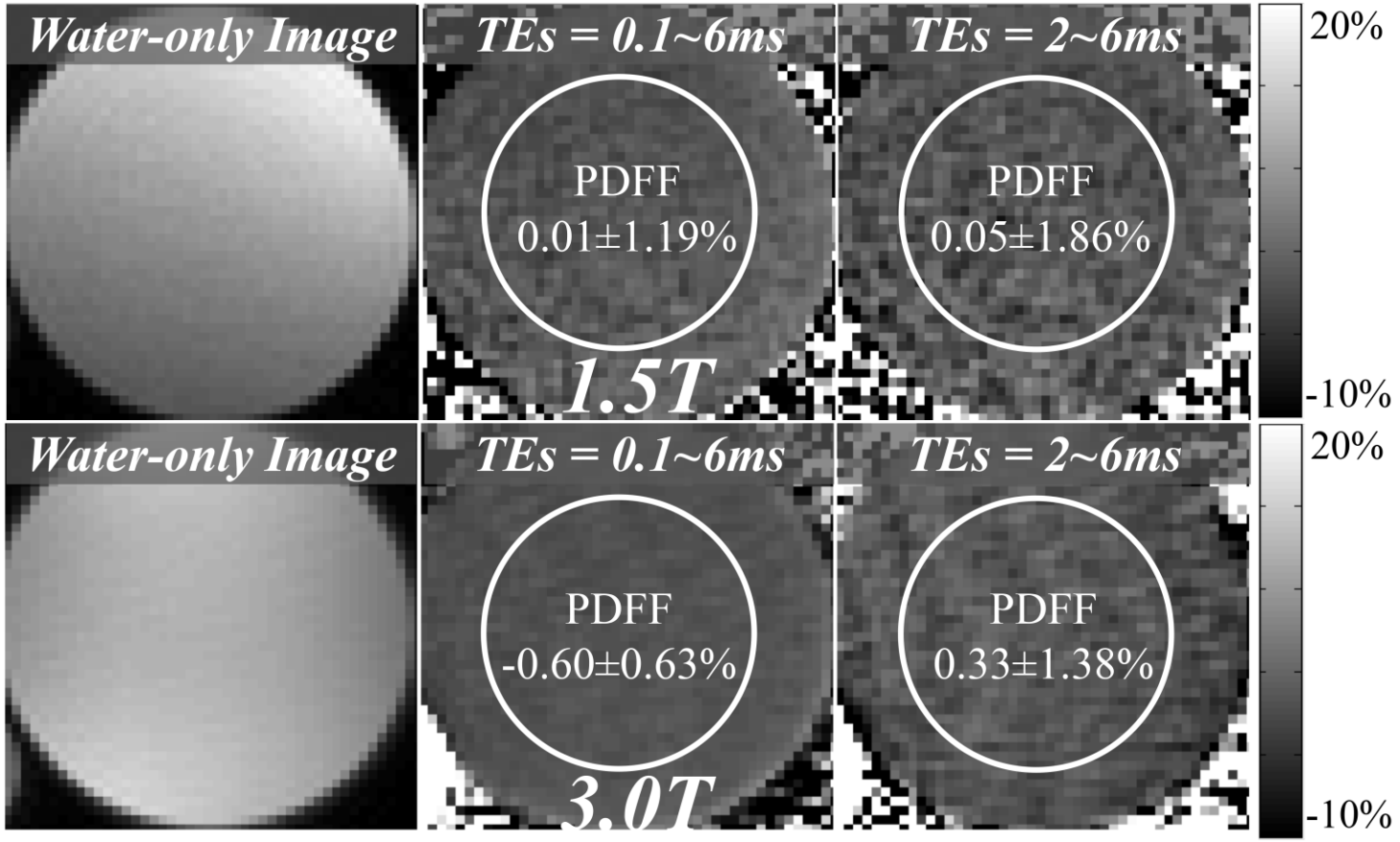

Figure 7. Water and PDFF maps of the water phantom using UTE-CSE. Water structural reference images (left column) and PDFF maps in CSE reconstruction of the $MnCl_2$-doped water phantom using all echo times (middle column: TEs=0.1~6 ms) and excluding short echo times (right column: TEs=2~6 ms) in the radial UTE-CSE acquisitions at both 1.5T and 3.0T. The estimated PDFF using all echoes (0.01% at 1.5T and -0.06% at 3.0T) or using only long echoes (0.05% at 1.5T and 0.33% at 3.0T) is consistent with the true PDFF=0% in this $MnCl_2$-doped water phantom. As in the $MnCl_2$-doped water phantom, we did not observe bias on PDFF using all echoes in UTE-CSE, suggesting that factors other than eddy currents, likely originating from the tissue itself, resulted in the bias on in vivo PDFF using all echoes in UTE-CSE (**Figure 5** and **Figure 6**).

2.4.4 Echo Time Optimization to Maximize Noise Performance of ST2 estimation

Figure 10 shows the maximum RMSE of the ST2 fraction (A, B, C) and $R_{2,\zeta}^{*}$ (D, E, F) in the Monte-Carlo simulation. Figures 10A and 10D show the maximum RMSE with varying echo spacing ΔTE_s and ΔTE_l at number of short echo times N equal to 4. Figures 10C and 10F shows the maximum RMSE with varying echo spacing ΔTE_s and numbers of short echo times N at echo spacing of long echo times ΔTE_l equal to 1.0 ms.

In Figures 10A and 10D, maximum RMSE is large when ΔTE_s is either shorter than 0.02 ms or longer than 0.2 ms, and increase as ΔTE_s increases from 0.08 ms to 0.23 ms. Maximum RMSE decreases as ΔTE_l increases in the range of 0.5 ms to 1.5 ms. Figures 10B and 10E delineate the second and third columns in Figures 10A and 10D, describing RMSE at ΔTE_s=0.05 ms (solid line) and 0.08 ms (dashed line). The influence of ΔTE_l on the maximum RMSE is small when ΔTE_l is in the range of 1.0 ms to 1.5 ms. A ΔTE_l of 1.0 ms is thus used to shorten TR, so as to reduce the acquisition time. In Figures 10C and 10F, maximum RMSE is shown to increase when N increases from 4 to 7. The lowest maximum RMSE is obtained at a N of 4 and a ΔTE_s of 0.05 ms.

According to the RMSE results, the optimized echo times are four ultrashort echo times starting with the 100 μs and having an echo spacing of 0.05 ms, and seven relatively long echo times starting with 1.0 ms and having an echo spacing of 1.0 ms. Moreover, the maximum bias at different echo time combinations follows a similar trend as the maximum RMSE. Consequently, the optimized echo times also favor minimizing the maximum bias of the ST2 fraction and $T_{2,\zeta}^{*}$.

The actual echo times were rounded up to the closest feasible time for UTE MRI, i.e., TE = [0.10, 0.15, 0.20, 0.25, 1.00, 2.00, 3.00, 4.00, 5.00, 6.00, 7.00] ms.

2.4.5 In vivo quantification of ST2 at 3.0T

The six healthy subjects imaged with radial UTE-CSE, the five patients with liver cirrhosis and five patients with hepatic steatosis (but no cirrhosis) imaged at 3.0T in **Section 2.3.2** were also imaged using the optimized UTE-CSE at 3.0T. The UTE-CSE data of one patient with hepatic steatosis were excluded because of excessive motion-related artifacts.

The plot of the liver signal intensity of a healthy subject is shown in **Figure 11**. The estimated ST2 fractions of all subjects are above 4.9% as shown in **Table 2**, demonstrating the consistent existence of the ST2 in the liver in different human cohorts. The ST2 fraction in the five patients with liver cirrhosis and the four patients with hepatic steatosis (but no cirrhosis) are 7.0±1.7% and 7.4±1.7%, respectively, compared to 9.6±1.5% in healthy subjects, although the difference was not statistically significant (P=0.08) as shown in **Figure 12**. $T_{2,\zeta}^{*}$ of 0.20±0.05 ms in patients with liver cirrhosis is not significantly different from that of 0.23±0.05 ms in healthy volunteers (P=0.79), while $T_{2,\zeta}^{*}$ of 0.10±0.02 ms in patients with hepatic steatosis (but no cirrhosis) is significantly lower than that in healthy volunteers (P=0.01) and in patients with liver cirrhosis (P=0.03).

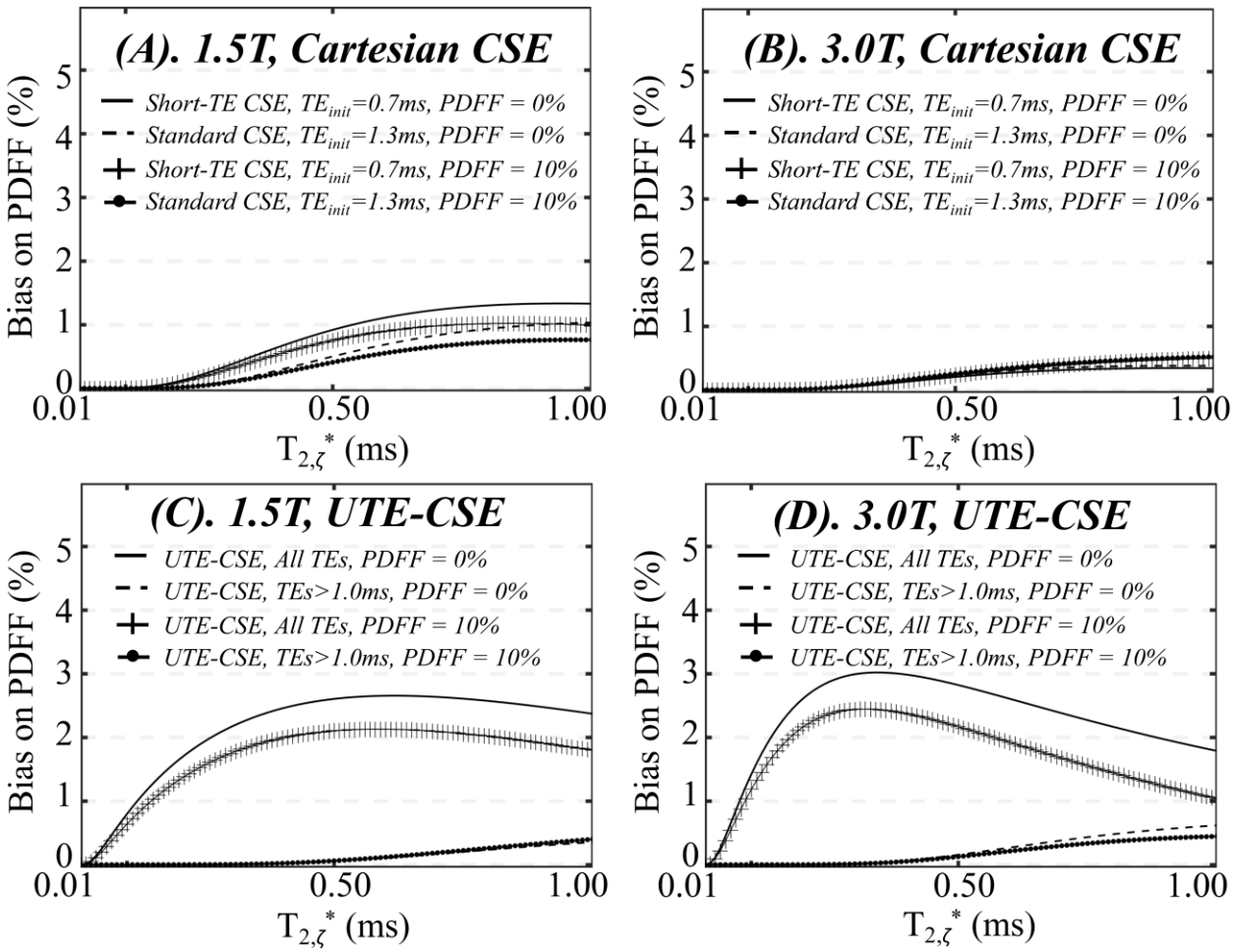

Figure 8. Simulations on the bias on PDFF estimation due to ST2. In simulation, the bias on PDFF estimation due to the presence of ST2 with a signal fraction of 10% is apparent in Short-TE CSE at 1.5T (A) and UTE-CSE at both 1.5T and 3.0T (C and D). The bias is reduced in estimations using only long echo times, i.e., Standard CSE at 1.5T (A) or UTE-CSE with echo times larger than 1ms at both field strengths (C and D). The bias is not obvious in Short-TE CSE or Standard CSE at 3.0T (B).

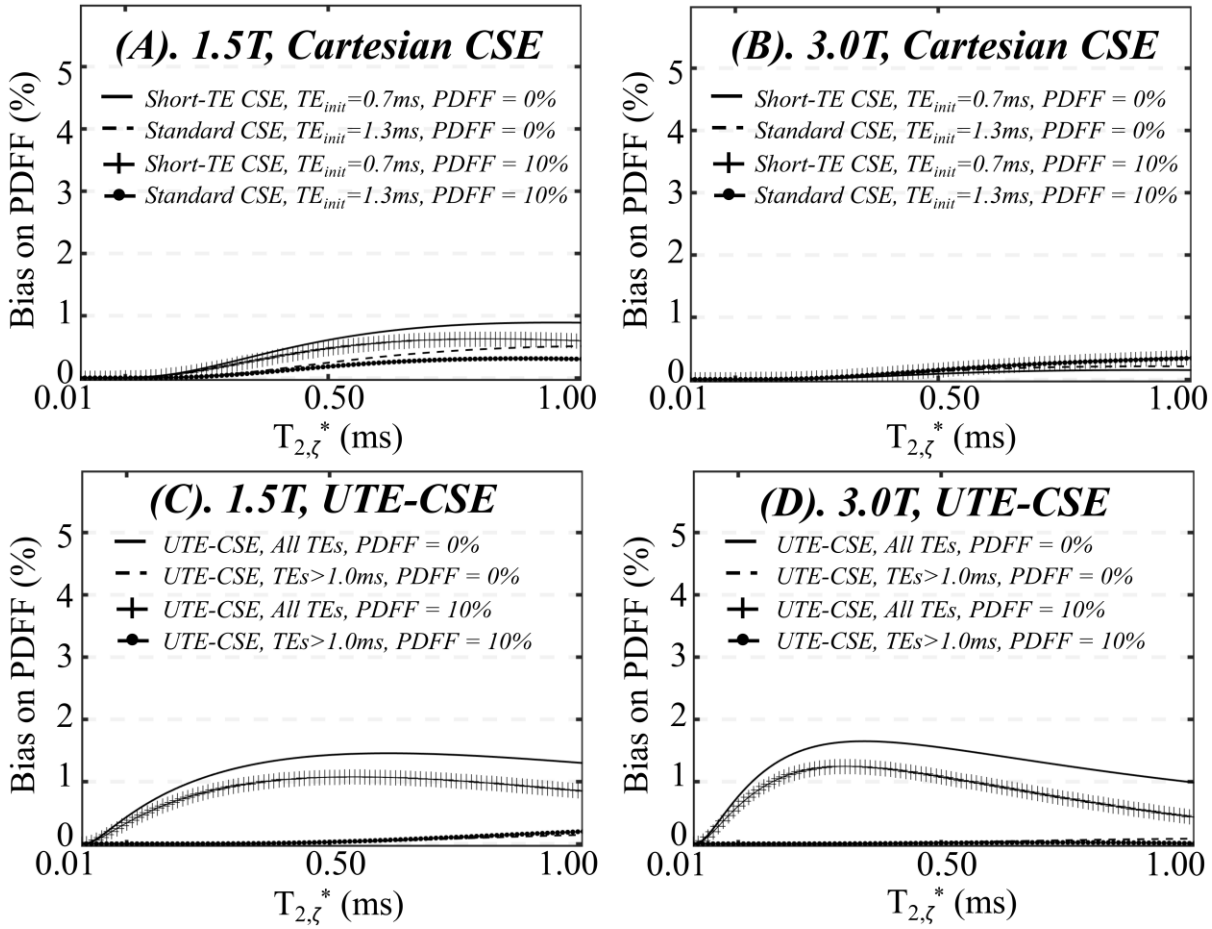

Figure 9. Simulations on the bias on PDFF estimation with complex signals. Simulations of the proposed complex liver signal model. The bias on PDFF estimation due to the presence of ST2 with a signal fraction of 10% is apparent in Short-TE CSE at 1.5T (A) and UTE-CSE at both 1.5T and 3.0T (C and D). The bias is reduced in estimations using only long echo times, i.e., Standard CSE at 1.5T (A) or UTE-CSE with echo times larger than 1ms at both field strengths (C and D). The bias is not obvious using Short-TE CSE or Standard CSE at 3.0T (B). In this simulation analysis, the bias on PDFF due to the presence of ST2 in the complex-based method is reduced but not diminished, compared to the magnitude-based method (**Figure 8**). Thus, the in vivo PDFF estimation using complex-based method may still be confounded by the presence of ST2 if uncounted for.

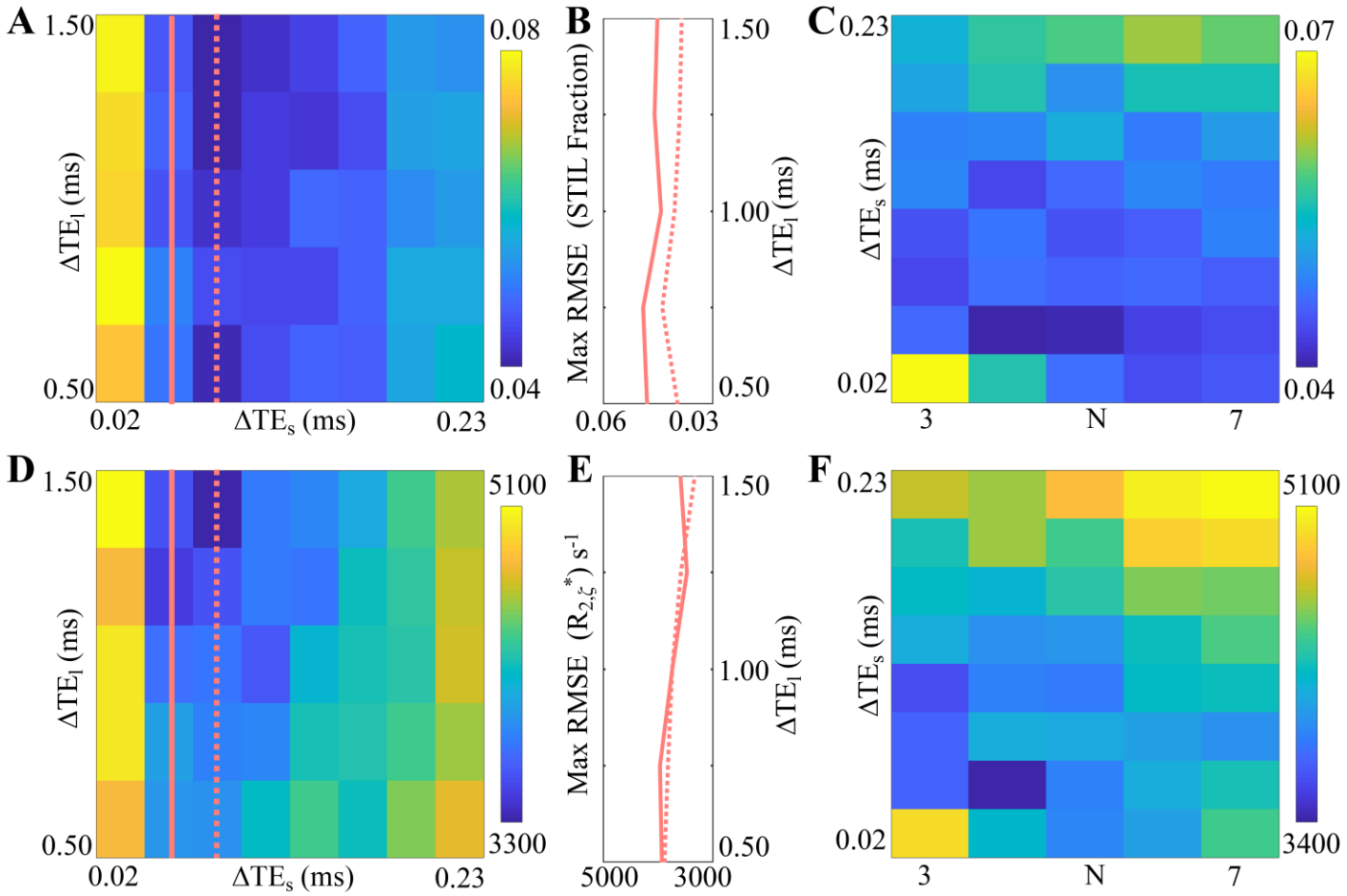

Figure 10. Echo time optimization using Monte-Carlo simulation. At 3.0T, Monte-Carlo simulation at a SNR of 200 shows that the maximum RMSE of the ST2 fraction (A, B, C) and $R_{2,\zeta}^{*}$ (D, E, F, unit: s^{-1}) is reduced at echo spacings ΔTE_s=0.05 ms and ΔTE_l=1.0 ms, and number of short echo times N=4. The maximum RMSE increases when ΔTE_s>0.08 ms or ΔTE_s<0.05 ms, and decreases when ΔTE_s>0.75 ms at number of short echo times N equal to 4 (A, D). The influence of ΔTE_l on the maximum RMSE is small when ΔTE_l is in the range of 1.0 ms to 1.5 ms at ΔTE_s=0.05 ms (solid line) and 0.08 ms (dashed line), as shown in (B) and (E), the profiles of the second and third columns in (A) and (D). A ΔTE_l of 1 ms is used to thus reduce the acquisition time, and the maximum RMSE at ΔTE_l =1 ms (C, F) is minimized at ΔTE_s =0.05 ms and N=4.

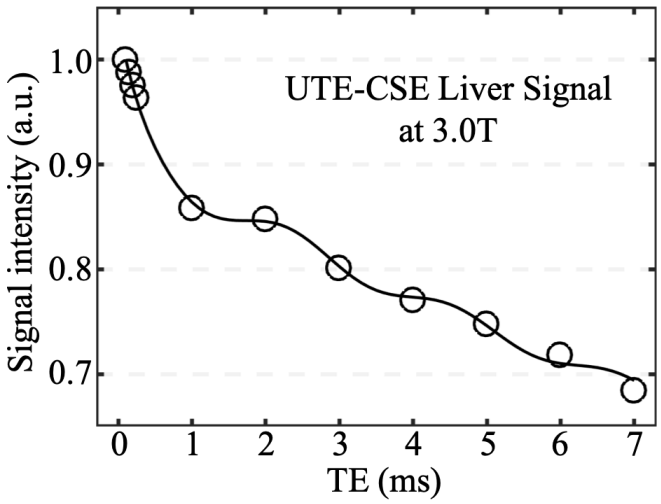

Figure 11. Liver signals of a healthy subject using UTE-CSE with optimized echo times. Fast decaying signals of ST2 (round circles) are successfully captured at the first four ultrashort echo times in the proposed optimized UTE-CSE at 3.0T, as well as the signal variations due to the chemical shift effects of the fat captured at the seven long TEs. The signal fit to the proposed multi-component liver signal model (solid line) shows a ST2 fraction of 11.0%, a $T_{2,\zeta}^{*}$ of 0.32 ms, a fat fraction of 1.8% and a T_2^{*} of 25.5 ms.

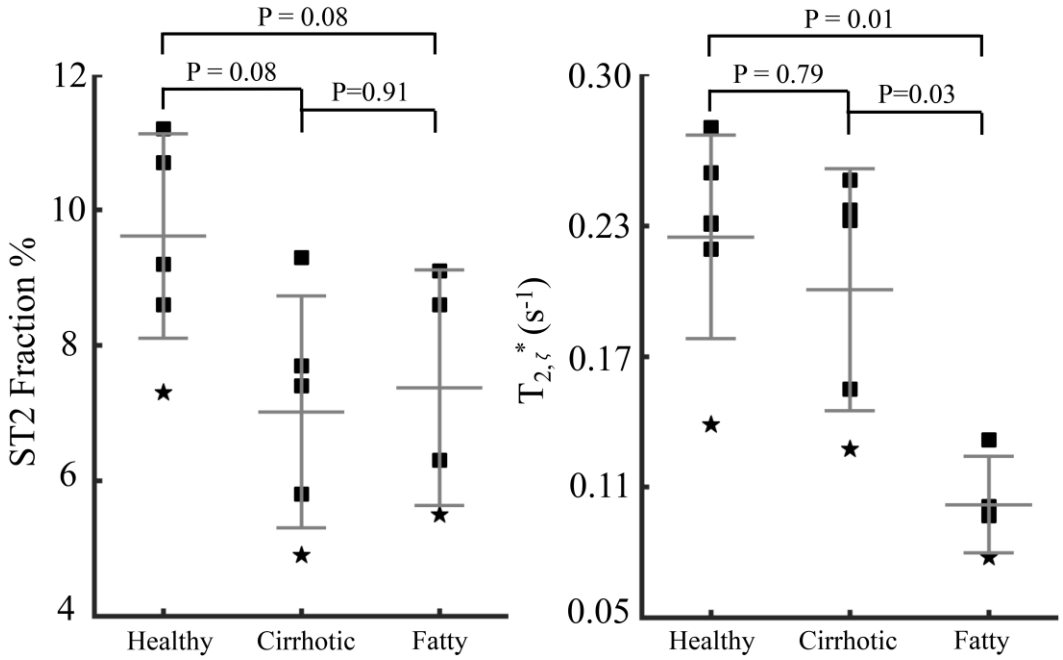

Figure 12. ST2 fraction and T_2^{*} of subjects at 3.0T. At 3.0T, the ST2 fraction (left) and $T_{2,\zeta}^{*}$ (right) of six healthy volunteers, five patients with liver cirrhosis and four patients with hepatic steatosis (but no cirrhosis) estimated in the proposed optimized UTE-CSE acquisitions.

2.5 Discussion

In this work, we have demonstrated the consistent presence of ST2 in the liver of healthy subjects, patients with liver cirrhosis and patients with hepatic steatosis by using a proposed UTE-CSE acquisition. In addition, we have demonstrated the presence of the ST2 signals leads to bias on liver fat quantification using CSE-MRI acquisition with short echo times.

The ST2 signal fraction that is preliminarily quantified at 3.0T is not significantly different between healthy subjects and patients with liver cirrhosis, suggesting that the origin of the ST2 signal may not be related to collagen tissue content, as patients with cirrhosis are expected to have a four- to sevenfold increase in collagen content[60]. In healthy volunteers who were imaged at both 3.0T and 1.5T, a longer $T_{2,\zeta}^*$ was estimated at 1.5T compared to the estimation at 3.0T in the same subject. Although higher SNR may be achieved at 3.0T, the shorter $T_{2,\zeta}^*$ may limit SNR benefit at 3.0T and affect the accuracy of the ST2 quantification, potentially leading to the discrepancy of the ST2 fractions estimated in the same subject at two field strengths.

The elevated in vivo liver signals at short echo times relative to the expected liver signal and the presence of bias in PDFF demonstrated that ST2 signals impact reproducibility of CSE fat quantification if unaccounted for. The confounding effects of the ST2 signals on liver fat quantification in Cartesian CSE using short echo times at 3.0T is not apparent in vivo, compared to the effects at 1.5T. The faster decay of in vivo ST2 signals at 3.0T, indicated by the shorter $T_{2,\zeta}^*$, may result in reduced bias on PDFF compared to that with a longer $T_{2,\zeta}^*$ at 1.5T, as shown in simulations. Furthermore, the water and fat signals at the short initial echo time (0.6 to 0.7 ms) are closer to in-phase at 1.5T compared to that at 3.0T due to the difference of water-fat chemical shift

frequencies. Therefore, the same amount of signal elevation due to ST2 potentially results in a larger error on PDFF estimation at 1.5T, as shown in simulation.

In addition to PDFF estimation, R_2^* ($1/T_2^*$) can be obtained from CSE-MRI acquisitions as a biomarker for liver iron overload[54,61,62]. UTE-based R_2^* mapping has been proposed for quantifying liver iron overload but has not considered the effect of ST2 on R_2^* estimation[62,63]. It is possible that the presence of ST2 signals may confound R2* quantification if not included in the liver signal model at short echo times. Further analysis of this effect is required in future studies.

This study has several limitations. First, patients with a broader range of PDFF need to be studied at 1.5T to evaluate the bias of PDFF estimation using short echo times less than 1 ms. In addition, echo time optimization for the ST2 quantification and the ST2 quantification of patients with liver cirrhosis were performed only at 3.0T in this study. The relatively long $T_{2,\zeta}^*$ at 1.5T, compared to the study at 3.0T in this work, may potentially benefit the ST2 quantification at 1.5T. Optimization of the echo times in UTE-CSE and patient studies at 1.5T are needed in the future. Further, we note that an ROI-based (i.e., signal average first and then fit) magnitude fitting was used in this work in order to estimate the fast decaying signals of ST2 with high SNR and also to avoid the effects of phase errors in the complex data. A homogenous distribution of ST2 in the liver was assumed, although the validity of this assumption is unknown. In future studies, the high spatial resolution used with 3D UTE-CSE in this study may not be necessary and could be reduced to increase SNR and shorten scan time.

In addition, since the T_1 value of ST2 is unknown, it is possible that the images may be slightly T_1-weighted such that the signal fraction of ST2 may contain T_1 bias and may not represent a true proton density fraction. Therefore, the signal fraction may be affected by acquisition parameters that impact T_1 weighting, specifically TR and flip angle. The potential T_1 bias may also

lead to the discrepancy of the ST2 fractions estimated in the same subject at two field strengths since T_1 is field strength dependent.

Exact quantification of short T_2^* signal component is challenging and may be biased by UTE-CSE MRI technique. For example, the radiofrequency pulse duration is known to confound short T_2 excitation, due to appreciable relaxation during the excitation[64]. In this work, we utilized a short duration, high bandwidth pulse to minimize potential excitation errors. However, a higher level of accuracy may be achievable in future studies using a Bloch equation-modeled method[64]. As a further limitation, systematic bias in UTE-CSE MRI can arise from eddy currents and receiver switching fidelity. These effects were evaluated in phantoms but may be sensitive to tissue relaxation properties and patient setup.

Further, the signal model of ST2 proposed in this work is empirical, i.e., based on our preliminary in vivo observations and also from previous studies in other tissues that model the short T_2^* signal as a mono-exponential, on-resonance signal decay. However, the accuracy of this signal model requires further validation. Ex-vivo human liver or small animal NMR experiments may be performed in the future to identify the exact ST2 signal component and improve the signal modeling of the liver. Moreover, echo times used in the ST2 quantification were optimized in simulation following several constrains based on the assumed signal model as well as the preliminarily quantified ST2 fraction and T_2^*. The first echo time in the long echo time group, where the ST2 signals were assumed to have decayed away, could be further optimized in the future based on the ST2 quantification of the larger population in this study.

2.6 Conclusion

We have described and provided preliminarily quantification of the signal fraction and T_2^* of a liver short T_2^* signal component in different human cohorts, and have demonstrated the consistent presence of this signal in vivo. Importantly, quantification of liver PDFF is confounded by ST2 when short echo times are used in CSE-MRI. Future studies are needed to characterize the MRI properties of ST2, to identify its origin, and to develop strategies that mitigate its impact on liver PDFF quantification using CSE-MRI.

Chapter

3. Characterization of Anisotropic Imaging Resolution Induced Bias in Liver Quantitative Susceptibility Mapping

3.1 Introduction

Excess iron accumulation in the body is toxic and can damage organs where iron deposits, such as the liver, pancreas, and heart. Liver iron concentration (LIC, units = mg Fe/g dry liver) is widely considered as the best overall metric of total body iron content[13]. Accurate detection and staging of LIC are needed to inform clinical iron-reducing treatments based on therapeutic phlebotomy or chelation therapy. Liver biopsy is considered the standard for iron quantification[65] but its clinical and research efficacy is limited due to its invasiveness and large sampling variability. Superconducting quantum interference device (SQUID)[66], a non-invasive technique to measure tissue magnetic susceptibility that linearly correlated with the iron concentration, has been validated to accurately quantify LIC. However, the high cost and limited availability of SQUID deter its wide use in clinic and research.

MRI is a non-invasive technique for quantifying iron content due to its sensitivity to the presence of iron[3]. Iron is paramagnetic and introduces field inhomogeneities in the static magnetic field. Tissue T_2 ($=1/R_2$) and T_2^* ($=1/R_2^*$) relaxation rates are shortened and R_2 and R_2^* have been

shown to be strongly correlated with iron concentration[67,68]. However, liver R_2^* may be confounded by other factors including the presence of hemorrhages or the microscopic iron distribution[69,70,71], etc. Importantly, tissue susceptibility, a fundamental property of tissue, is affected by the presence of iron and has been shown to be insensitive to the microscopic iron distribution in phantoms[69,72]. Consequently, MRI-based quantitative susceptibility mapping (QSM) is a promising non-invasive technique to assess LIC in patients with iron overload.

In liver QSM, tissue susceptibility is estimated from the B_0 field which can be encoded and extracted from the image phase in 3D chemical shift-encoded (CSE) MRI[4]. The accuracy of the image phase, however, has been found to be dependent on imaging resolution by different research groups[14,15,73,74]. Indeed, Gibbs phenomenon introduces truncation artifacts in phase images with low resolutions, especially in tissue boundaries. Unlike R_2^* estimated from signals pixel-by-pixel, the susceptibility estimation is obtained through the deconvolution of the entire phase map. Unfortunately, the Gibbs ringing artifacts are disseminated to the entire susceptibility map. Therefore, the spatial resolution may result in confounded estimation of tissue susceptibility.

The range of achievable spatial resolutions in liver QSM is limited by several factors. Acquisition of the 3D liver volume is normally obtained in a single breath-hold to reduce respiratory motion-induced image artifacts. In addition, the range of LIC is relatively broad, leading to high R_2^* especially at high iron content. Subsequently, a short first echo time is needed to capture the fast decaying signal. In Cartesian CSE-MRI, the need for a short scan time limits imaging resolution along the phase-encoding directions, whereas the need for short first echo time limits resolution along the readout direction. Due to these constraints, anisotropic imaging resolution is typically obtained in Cartesian-based liver QSM. Non-Cartesian techniques including cones and radial acquisitions enable ultrashort echo time (UTE) while maintaining high spatial

resolution[75]. The relatively long scan time and the sophisticated calibration and reconstruction algorithms needed to diminish system errors in UTE MRI techniques limit the clinical efficacy without comprehensive validation studies.

Previous studies have demonstrated that the accuracy of susceptibility measurements depend on the acquired image resolution in phantom, simulations and in vivo human brains[14,15,73,74]. Images with reduced isotropic resolution or resolution in the superior-inferior direction (main B_0 field direction) result in reduced susceptibility contrast and errors in susceptibility measurements. Further, it has been noted that resolution-induced QSM errors vary in organs with different shapes and tissue contrasts, as well as depend on the imaging direction and reconstruction methods[15]. The liver is irregular in shape, especially compared to the relatively left-right symmetric brain and is surrounded by organs and tissues with varying MRI properties. Additionally, the anisotropic resolutions obtained in liver QSM also differs from phantom or brain QSM where approximately isotropic resolution is usually achieved. Therefore, the characterization of resolution effects along the different MRI encoding directions is highly desirable.

The purpose of this work was to characterize the bias in liver QSM with anisotropic imaging resolution. This assessment may guide subsequent optimization of the imaging protocols and reconstruction algorithms for accurate and robust liver QSM.

3.2 Methods

3.2.1 Simulation

A numerical abdominal phantom was created by segmenting a high-resolution post-contrast T_1-weighted patient MR image as shown in **Figure 13**. Realistic 1.5T MRI properties

including R_1, R_2^*, PDFF, and susceptibility were assigned to the tissue of liver, arterial blood, muscle, subcutaneous fat, spleen, lung and others, as shown in **Table 3**. A six peak fat spectrum[58] with frequency shift = [0.6, -0.5, -1.95, -2.6, -3.4, -3.8] ppm and relative amplitude = [4.7, 3.9, 0.6, 12.0, 70.0, 8.8]% was used to model the chemical shift effects of the fat. 3D multi-echo spoiled gradient-echo (SGRE) images with 1.5×1.5×1.8 mm^3 resolution were simulated. The simulation parameters include: 6 echoes, $TE_{init}/\Delta TE$ = 1.2/2.0 ms, TR = 14.6 ms, flip angle = 5°. The B0 field map was obtained by calculating the convolution of the tissue susceptibility map and the dipole kernel. The complex signal at each echo was then generated using Equation 1 in Hernando et al[55].

The multi-echo gradient-echo images were downsampled with different ratios, e.g., ×1, ×2, ×3, ×4, along the liver left-right and superior-inferior direction, separately, using zero-padding. Water, PDFF, R_2^*, and field maps were estimated from each dataset of the multi-echo images with different acquired resolutions using a chemical shift-encoded reconstruction[76]. Susceptibility maps were obtained using a liver QSM reconstruction with combined Laplacian background field removal and dipole inversion in one step, with a L_2-norm regularization[4].

We evaluated the susceptibility measurements in regions-of-interest (ROIs) in different regions of the liver. An elliptical ROI in the left liver lobe, in the top liver, and in the bottom liver, separately, were drawn, as shown in **Figure 14**. Adjacent tissues, either subcutaneous fat or nearby water, were used as a susceptibility reference.

3.2.2 In vivo experiments

All in vivo studies were HIPAA compliant and were approved by the local Institutional Review Board (IRB). In total, 27 subjects with known or suspected liver iron overload were

scanned at 1.5T after obtaining informed written consent. MRI data were retrospectively analyzed for 11

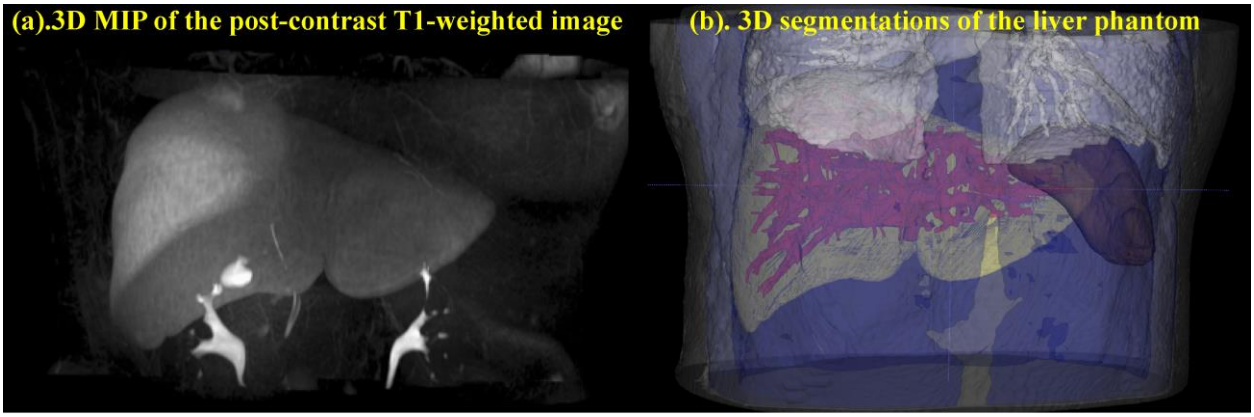

Figure 13. Numerical abdominal phantom.

Table 3. Tissue MRI properties in the numerical phantom.

Tissues / Organs	Susceptibility (ppm)	R_2^* (s^{-1})	PDFF (%)	R_1 (s^{-1})
Liver	-6	206	0	1.68
Muscle	-7.38	20	0	0.88
Subcutaneous Fat	-7	30	100	3.47
Spleen	-7.12	55	0	0.95
Blood (Arterial)	-9	254	0	0.70
Lung (Air)	0	10000	0	10000
Other	-9	10	0	0.25

subjects imaged with two breath-held 3D SGRE-MRI with different left-right imaging resolutions (Protocol-LR #1 and #2), and 16 subjects imaged with two different superior-inferior resolutions (Protocol-SI #1 and #2). The imaging parameters include: Protocol-LR #1: 6 echoes, $TE_{init}/\Delta TE$ = 1.2/2.0 ms, TR = 14.6 ms, flip angle = 5°, acquired resolution = 1.7×2.3×8.0 mm^3; Protocol-LR

#2: 12 echoes, $TE_{init}/\Delta TE$ = 0.8/0.7 ms, TR = 9.6 ms, flip angle = 5°, acquired resolution = 2.5×2.5×8.0 mm^3; Protocol-SI #1: 6 echoes, $TE_{init}/\Delta TE$ = 1.2/2.0 ms, TR = 14.6 ms, flip angle = 5°, acquired resolution = 1.7×2.5×6.0 mm^3, 6 echoes, $TE_{init}/\Delta TE$ = 1.2/2.0 ms, TR = 14.6 ms, flip angle = 5°, acquired resolution = 1.7×2.3×10.0 mm^3.

To isolate the effect of resolution, images of higher acquired resolution (Protocol-LR #1/-SI #1) were downsampled to match the resolution in Protocol-LR #2/-SI#2, respectively, and labeled as Protocol-LR #1/-SI #1 downsampled. Water, PDFF, R_2^*, and field maps were estimated from each dataset using the chemical shift-encoded reconstruction[76]. Susceptibility maps were obtained using the liver QSM reconstruction[4]. The liver susceptibility was measured in a large elliptical ROI drawn at the right lobe of the liver using adjacent subcutaneous fat tissue as a susceptibility reference. In vivo susceptibilities obtained from different protocols were compared using linear regression and Bland-Altman analysis.

3.3 Results

In the numerical simulation (**Figure 14**), ringing artifacts appear at the boundaries in the susceptibility map after downsampling. The low imaging resolution in different directions at a fixed downsampling ratio leads to varying biases in liver susceptibility measurements ($\Delta\chi_{Liver}$) in different ROIs (purple). Downsample-LR (red, $\Delta\chi_{Liver}$=0.6-1.0 ppm) leads to a bigger bias in the ROI at the right of the liver (star marker, true liver susceptibility relative to the subcutaneous fat=1 ppm) compared to that in downsample-SI (blue, $\Delta\chi_{Liver}$=0.9-1.0 ppm) at a fixed downsampling ratio. A similar amount of bias in the ROI at the bottom of the liver (round marker, true liver susceptibility relative to water=3 ppm) is observed in downsample-LR ($\Delta\chi_{Liver}$=1.8-3.0 ppm) or donwsample-SI ($\Delta\chi_{Liver}$=1.7-3.0 ppm). A smaller bias in the ROI at the top of the liver (triangle

marker, true liver susceptibility relative to water=3 ppm) in downsample-LR ($\Delta\chi_{Liver}$=2.6-3.0 ppm) is observed compared to that in donwsampling-SI ($\Delta\chi_{Liver}$=1.7-3.0 ppm).

In the subjects imaged with different LR resolutions, the susceptibility map of one subject in Protocol-LR #2 (lower left-right resolution) is blurred compared to that in Protocol-LR #1 (**Figure 15**A). The estimated liver susceptibility relative to the subcutaneous fat ranges from -0.3 ppm to 4.4 ppm in all 11 subjects. The liver susceptibilities of all subjects measured in the protocol with high LR resolution (Protocol-LR #1) are higher than that measured in protocols with low LR resolution (Protocol-LR #1 downsampled and Protocol-LR #2), especially at high liver susceptibilities (**Figure 15**B). The estimated liver susceptibilities are similar in protocols with same imaging resolution, i.e., Protocol-LR #1 downsampled and Protocol-LR #2 (**Figure 15**B), indicated by a slope of 1.06 in the linear regression analysis.

The estimated liver susceptibility relative to the subcutaneous fat ranges from -0.2 ppm to 2.8 ppm in all 16 subjects, as shown in **Figure 15**D. The liver susceptibilities of all subjects measured in protocols with/without downsampling in SI imaging resolutions are similar, indicated by a slope close to 1 in the linear regression analysis. The liver susceptibilities estimated in the protocol with lower acquired resolution (Protocol-SI #2) are slightly lower than that measured in the protocol with higher acquired resolution (Protocol-SI #2), especially at high liver susceptibilities.

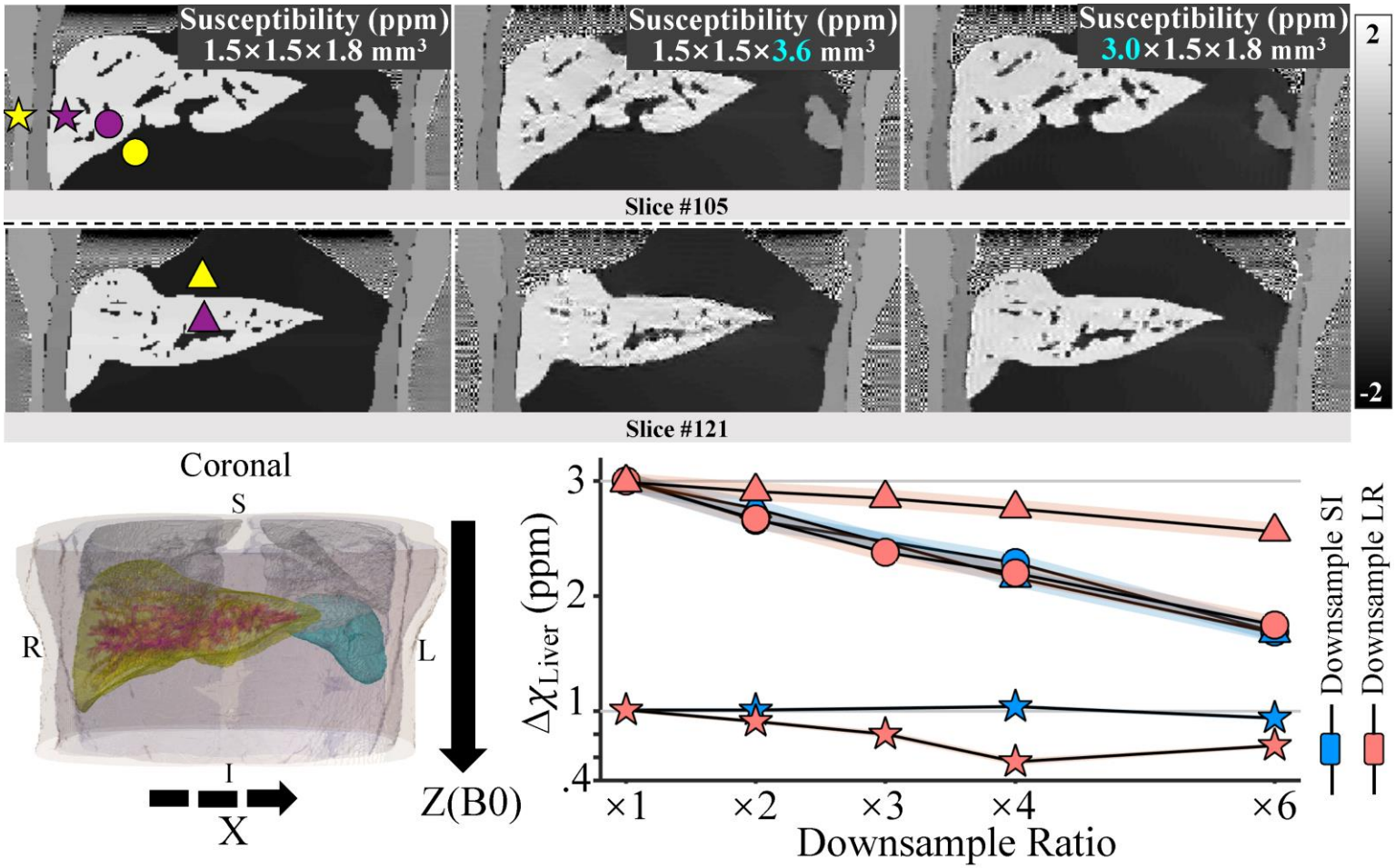

Figure 14. Liver susceptibility measurements in the numerical phantom. In the numerical phantom, ringing artifacts at the tissue boundaries are shown in susceptibility maps obtained with different acquired resolutions. Liver susceptibility (χ) measured from different liver ROIs (purple) using different susceptibility references (yellow) show different amounts of bias when downsampling along different directions. Downsampling-LR (red) leads to a bigger bias in the ROI at the right of the liver (star) compared to that in downsampling-SI (blue) at a fixed downsampling ration. A similar amount of bias in the ROI at the bottom (round) and a smaller bias in the ROI at the top (triangle) in downsampling-LR are observed compared to that in donwsampling-SI, respectively.

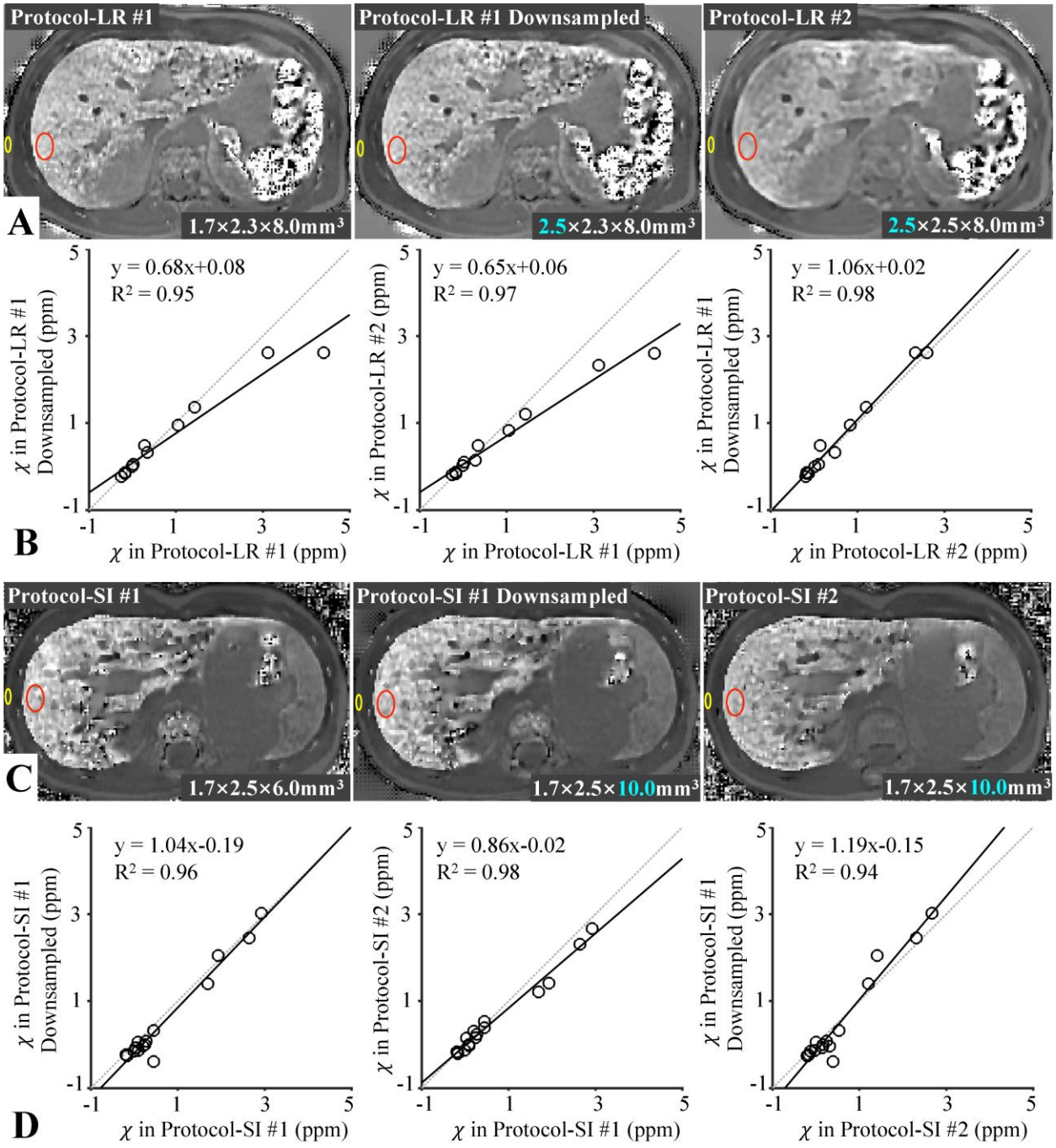

Figure 15. In vivo liver susceptibility measurements. The susceptibility map of one subject in Protocol-LR #2 (lower left-right resolution) is blurred compared to that in Protocol-LR #1 (A). In linear regression (B), the susceptibilities of all subjects measured in Protocol-LR #1 with downsampling and Protocol-LR #2 are similar (which have the same imaging resolution but different TEs and TRs) but are both lower than that measured in Protocol-LR #1, especially at high liver susceptibilities. This strongly suggests the liver left-right imaging resolution affects the QSM estimates. The susceptibilities measurements in the three Protocol-SI are similar, as shown in the susceptibility map of one subject (C) and linear regression of measurements of all subjects (D)

3.4 Discussion

In this study, we thoroughly characterized the effect of low image resolution in two directions separately, i.e., the in-plane left-right direction and the through-slice superior-inferior direction in liver QSM. Compared to previous studies assessing the effects of image resolution on QSM, which have been mainly focused on the through-slice direction, this study of the left-right imaging resolution is particularly necessary for quantification of high LIC, e.g., with severe liver iron overload. The shortening of tissue T_2^* (e.g., <1.5 ms at 1.5T) in the presence of high LIC (e.g., >20 mg/g dry tissue) leads to a fast signal decay. A short first echo time is thus highly desirable, however, this limits the readout resolution which is typically the liver left-right direction. Therefore, assessing the effect of the left-right resolution on the accuracy of QSM provides guidance on joint optimization of the echo time and the imaging resolution in liver QSM.

ROI sampling of quantitative measurements is necessary due to the spatial heterogeneity of LIC[77]. However, the spatial variation of the susceptibility bias caused by low image resolutions suggests that ROI sampling of the liver susceptibility measurements affects the characterization of the resolution effects on liver QSM. Additionally, the susceptibility interface of the liver tissue to the adjacent reference tissue, including the direction of tissue boundaries and the susceptibility contrast, varies spatially as the liver is surrounded by multiple organs with different MRI properties. The low image resolution thus results in different amounts of bias on the susceptibility contrast depending on the downsampling directions and ROI sampling scheme, which has been hypothesized in Karsa et al[15].

In patient studies, the susceptibility measurements from the acquired low-resolution images agrees with that from the retrospectively downsampled images with a same low resolution.

This agreement indicates that the image resolution substantially affect in vivo liver QSM besides other confounding factors like motion and noise. Our results are consistent with the previous study on the effect of spatial resolution in brain QSM[15].

In agreement with previous studies, the effect of image resolution depends on the shape of the object and MRI properties. Thus, whether the observations in liver QSM can be applied to brain QSM is unknown. A comprehensive analysis on the low in-plane imaging resolution in the brain might be valuable, especially in functional QSM where the in-plane resolution is limited due to the need of a fast acquisition[78,79].

High resolution along the superior-inferior direction is potentially achievable by limiting the FOV coverage. However, it has been reported that the reduction of the FOV coverage in the brain may affect the accuracy of QSM, depending on the ratio between the size of the ROI along the superior-inferior direction to the FOV coverage along the superior-inferior direction[15]. The evaluation the FOV coverage in liver QSM is future work.

This study has several limitations. First, the number of in vivo cases is limited, especially at high liver susceptibilities. A larger dataset is needed to further confirm the observations on the susceptibility bias in this study. Similarly, simulations with varying liver susceptibilities are also needed to comprehensively analyze the resolution effects. In addition, the characterization of bias on in vivo liver QSM can be further improved by comparing with standard susceptibility references from SQUID[66]. Moreover, the susceptibility estimate has been shown to depend on the reconstruction algorithm[15]. Therefore, characterization of this resolution-induced bias on liver QSM with different reconstruction algorithms is needed, including morphology enabled dipole inversion (MEDI) based QSM that has been used in brain and body applications[70].

3.5 Conclusion

We have characterized the resolution-induced bias on liver QSM along different imaging directions separately and preliminarily showed that the low image resolution results in different amounts of bias on the susceptibility contrast depending on the downsampling directions. This study may guide future protocol optimization for accurate liver QSM (e.g., k-space sampling approaches in limited scan time).

Chapter

4. Quantitative Ferumoxytol-enhanced MRI in Pregnancy: A Feasibility Study in the Nonhuman Primate††

4.1 Introduction

Preeclampsia is an inflammatory condition of human pregnancy that can lead to peripheral edema, hypertension, seizures and maternal death[80,81]. Maternal vascular dysfunction at the maternal-fetal interface in preeclampsia leads to insufficient placental perfusion and activation of the uteroplacental inflammatory response[82,83]. Altered immune cell (e.g. macrophage) activation and distribution within the maternal-fetal interface may also play an important role in the development of adverse pregnancy outcomes[84]. Evaluation of macrophage distribution may enable early assessment of the developing pathophysiologic conditions in preeclampsia and/or inflammation-induced fetal growth restriction before their clinical manifestation. Thus, evaluation

---

†† This work has been published in: Zhu A, Reeder SB, Johnson KM, Nguyen S, Fain SB, Bird IM, Golos TG, Wieben O, Shah DM, Hernando D. Quantitative ferumoxytol-enhanced MRI in pregnancy: a feasibility study in the nonhuman primate. *Magn Reson Imaging.* 2020;65:100-108.

of macrophage distribution and activity is highly desirable for identifying immune cell homing in pregnancy.

Ferumoxytol is an FDA-approved iron compound for treatment of anemia[85] which recently has received substantial interest as an off-label contrast agent in MRI[86,87]. Ferumoxytol particles are phagocytosed by macrophage in the reticuloendothelial system or sites with activated inflammation responses[88]. Importantly, the presence of ferumoxytol affects MR contrast parameters, including R_2^* ($=1/T_2^*$) and magnetic susceptibility. Quantitative R_2^* mapping and quantitative susceptibility mapping (QSM) have been used for detection of ferumoxytol[20,21,23] and characterization of microscopic iron distribution[69,71]. Ferumoxytol-enhanced MRI has been shown to enable non-invasive assessment of macrophages in applications including pancreatic inflammation in type I diabetes, high-grade gliomas, and inflammation after myocardial infarction[19,89,90]. Therefore, ferumoxytol-enhanced MRI may enable sensitive detection of macrophage homing in inflammation at the maternal-fetal interface.

However, the use of ferumoxytol for the assessment of macrophage distribution in pregnancy, and the safety of the ferumoxytol use, including the potential uptake in the fetus after maternal administration, have not been investigated. Unlike gadolinium-based contrast agents with an approximate diameter of 0.4 nm[88], which cross the placenta into the fetal circulation[91,92], ferumoxytol with an approximate diameter of 30 nm[88] may not transport directly into fetal circulation[93]. The nonhuman primate has the most similar placentation, physiology and immunology with the human reproductive system[94,95,96]. Thus, quantification of iron accumulation at the maternal-fetal interface and in the fetus after ferumoxytol exposure in nonhuman primates would constitute an important step towards evaluating the feasibility and safety of ferumoxytol-enhanced MRI in human pregnancy.

The hypothesis for this work was that maternal ferumoxytol exposure will not lead to increased iron deposition in fetal tissues. Further, we hypothesize that ferumoxytol will be taken up by macrophages in the placenta or the decidua, the endometrium of pregnancy, in inflammation with macrophage homing and will be detectable by MRI. Therefore, the purpose of this study was to assess the feasibility of ferumoxytol-enhanced R_2^* mapping and QSM in a pregnant nonhuman primate model.

4.2 Methods

4.2.1 Animals and Experimental Procedure

This prospective animal study was approved by our institution's animal care and use committee. Interleukin 1 beta (IL-1β), a pro-inflammatory cytokine, was used to generate inflammation at the maternal-fetal interface. Eleven pregnant rhesus macaques at day 98±5 of gestation (average term pregnancy=165 days), equivalent to the late second trimester of human pregnancy, were obtained. Animals were divided into three groups, i.e., untreated control (UC) (n=3), saline control (SC) (n=4), and IL-1β treated (IT) (n=4). For all procedures and MRI scans, the animal was anesthetized by administration of up to 10 mg/kg ketamine and the sedation was prolonged by delivering oxygen with 1.5% isoflurane through inhalation. The animal was monitored during all procedures, and subsequently until fully recovery from the anesthesia. Veterinarian staff were alerted for treatment if the recovery took more than 90 minutes, or if there were symptoms of compromised health.

Each animal in the UC group was imaged first as baseline (Day 0-pre). Subsequently, ferumoxytol (AMAG Pharmaceuticals, Waltham, MA, USA) was administered intravenously at a

dose of 4 mg/kg, diluted 5:1 with sterile saline. Immediately after ferumoxytol administration, the animal was imaged again (Day 0-post) and follow-up MRI scans were performed afterwards at four time points within 25 days (Day 1-25), as shown in the flow chart of **Figure 16**.

Each animal in either the SC or IT group was imaged first as baseline (Day -2/-1). On the same day after the baseline imaging, animals were administered either saline (0.5 mL) or IL-1β (10 μg IL-1β in 0.5mL saline) into the amniotic using a needle inserted through an aseptically prepared site of the abdominal wall and introduced until the tip touched the uterus wall. Subsequent scans were started one or two days later, in order to allow for inflammation to develop. The animals were then imaged before and immediately after ferumoxytol administration (Day 0 pre/post) and follow-up scans were performed afterwards within three days (Day 1-3), as shown in the flow chart of **Figure 16**. Animal information, drug dose, ferumoxytol administration and scan time points are detailed in **Table 4**. Histology and iron quantification analysis on placental and fetal tissues were performed after the last MRI scan.

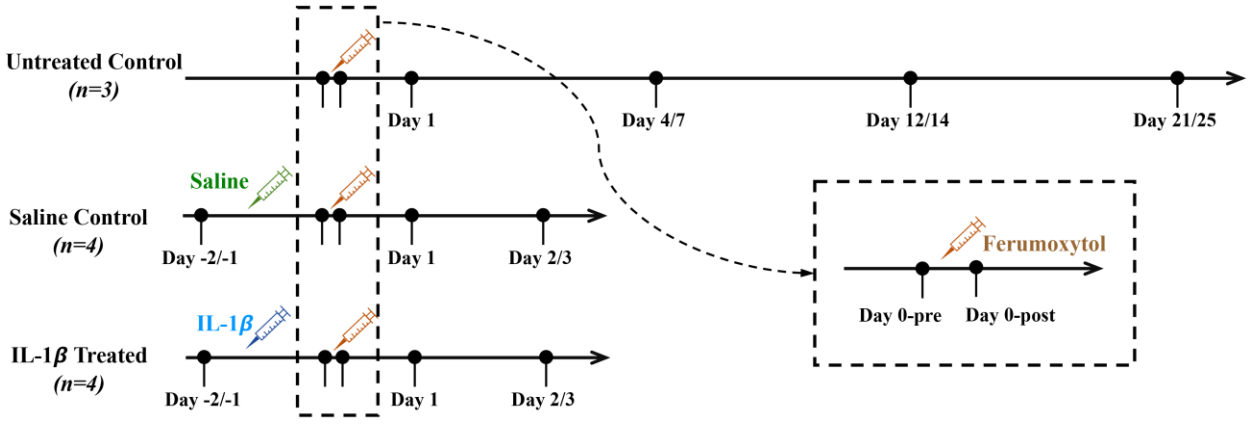

Figure 16. Flow chart of the MRI scan time points. Flow chart of the MRI scan time points relative to the administration of ferumoxytol, saline and IL-1β for all eleven animals.

4.2.2 MRI Acquisition

MRI scans were performed on a 3.0T MRI system (Discovery 750, GE Healthcare, Waukesha, WI, USA) using a 32-channel torso coil (Neocoil, Pewaukee, WI, USA) with the animal in the left lateral decubitus position. An axial 3D multi-echo spoiled gradient-echo (SGRE) acquisition of the maternal pelvis covering the uterus cavity was obtained to evaluate the ferumoxytol distribution at the maternal-fetal interface. Additionally, the ferumoxytol distribution in the maternal reticuloendothelial system including the maternal liver was also evaluated in this study. For this purpose, an axial 3D multi-echo SGRE radial ultra-short TE (UTE-SGRE) acquisition of the maternal abdomen covering the maternal liver was performed. Respiratory-gating[49] was used in both acquisitions. Scan parameters are detailed in **Table 5**.

4.2.3 Imaging Reconstruction and Data Analysis

R_2^* maps of the maternal pelvis were generated from the SGRE images using a chemical shift-encoded reconstruction[97]. R_2^* maps of the maternal abdomen were obtained by using monoexponential fit of echoes in the UTE-SGRE images. In each animal at each scan time point, R_2^* of the amniotic fluid, the fetal liver, the fetal lung, the two separate placental discs, and the maternal liver were measured in oval regions of interest (ROIs). Information on ROIs is detailed in **Table 6**.

Susceptibility maps of the maternal pelvis were generated from the SGRE images using a QSM reconstruction[4]. All susceptibility measurements were calculated relative to the adjacent amniotic fluid, which was used as a susceptibility reference as no ferumoxytol uptake was

observed as shown below. The fetal liver susceptibility was measured by calculating the difference between the susceptibility values in the fetal liver and the amniotic fluid. The placental susceptibility was measured by calculating the difference between the susceptibility values in one of the placental discs and the amniotic fluid.

4.2.4 Statistical Analysis

To investigate the longitudinal variation of R_2^* and susceptibility measurements of the fetal liver and R_2^* measurements of the fetal lung, a linear mixed-effects model was used. The model included the time interval of each scan to the baseline scan as a fixed continuous factor, the animal groups as a fixed classification factor, the interaction of the animal group and the time interval as a fixed factor, and animal as a random classification factor.

To investigate the longitudinal variation of placental R_2^* and susceptibility measurements, and maternal liver R_2^*, respectively, a linear-mixed effects model was used in each animal group, including the scan time point as a fixed classification factor and animal as a random classification factor. The changes at each scan time point from baseline were calculated for placental R_2^* as $\Delta R2^*_p = R2^*_{p,TimePoint} - R2^*_{p,Baseline}$, for placental susceptibility as $\Delta\chi_p = \chi_{p,TimePoint} - \chi_{p,Baseline}$, and for maternal liver R_2^* as $\Delta R2^*_l = R2^*_{l,TimePoint} - R2^*_{l,Baseline}$. To investigate the inter-group difference on the longitudinal variation of MRI measurements, Student's t-test with conservative Bonferroni correction for multiple comparison was used to compare $\Delta R2^*_p$ at each time point between the SC and IT groups, as well as $\Delta\chi_p$ and $\Delta R2^*_l$. Statistical analyses were performed in Matlab (MathWorks, Natick, MA, USA). Statistical significance was selected as a *P* value less than 0.05.

4.2.5 Estimation of iron concentration based on R_2^* and susceptibility measurements

- Liu et al[18] reported R_2^* relaxivity of ferumoxytol as follows:

$$R_2^* = 1562\times[\text{Iron}]+2 \quad (10)$$

where [Iron] is the iron concentration with units of mg/mL, R_2^* has units of s^{-1}, and the slope 1562 has units of $s^{-1}\cdot mL/mg$. Note that ferumoxytol consists of 30 mg/mL elemental iron.

- Barick et al[98] and Laurent et al[99] reported R_2 relaxivity of ferumoxytol (Advanced Magnetics, Cambridge, MA) as follows:

$$R_2 = 84.9\times[\text{Iron}] \quad (11)$$

where [Iron] is the iron concentration with units of mM, R_2 has units of s^{-1}, and the slope 84.9 has units of $s^{-1}\cdot mM^{-1}$. Based on phantom experiments by Knobloch et al[17], we assume that in ferumoxytol $R_2^*\approx R_2$. As the molecular weight of iron is 55.85 g/mol, **Equation 11** can be rewritten as,

$$R_2 = 84.9\times[\text{Iron}]/55.85\times1000 = 1520\times[\text{Iron}] \quad (12)$$

where [Iron] has units of mg/mL and the slope 1520 has units of $s^{-1}\cdot mL/mg$. The slopes in **Equations 10-13** have similar values. We used a slope of 1562 $s^{-1}\cdot mL/mg$ in the following calculations.

- Liu et al[18] reported the susceptibility of the ferumoxytol as follows:

$$\chi = 32.0\times[\text{Iron}] \quad (13)$$

where [Iron] is the iron concentration with units of mg/mL, χ is the susceptibility with units of ppm, and the slope 32.0 has units of ppm·mL/mg.

Table 4. Animal information, drug dose and ferumoxytol administration.

Rhesus No.	Groups	Gestational Age (days)	Maternal Weight (kg)	Scan Time Points	Drug Administration	Ferumoxytol Administration	Administration Rate (ml/s)
1	UC	102	7.0	Day 0 pre/post, 1, 4, 12, 25	N/A	Hand Administrated over 10 mins.	0.009
2	UC	106	10.0	Day 0 pre/post, 1, 7, 14, 21	N/A	Administrated with a power injector over 20s.	0.39
3	UC	91	9.9	Day 0 pre/post, 1, 7, 14, 21	N/A	Administrated with a power injector over 20s.	0.39
4	IT	92	9.8	Day -1, Day 0 pre/post, 1, 3	10 μg IL-1β in 0.5mL sterile saline	Administrated with a power injector over 20s.	0.39
5	SC	103	7.1	Day -1, Day 0 pre/post, 1, 3	0.5mL Saline	Administrated with a power injector over 20s.	0.27
6	IT	98	7.6	Day -1, Day 0 pre/post, 1, 2	10 μg IL-1β in 0.5mL sterile saline	Administrated with a power injector over 20s.	0.30
7	IT	92	8.6	Day -1, Day 0 pre/post, 1, 2	10 μg IL-1β in 0.5mL sterile saline	Administrated with a power injector over 20s.	0.33
8	SC	99	9.1	Day -1, Day 0 pre/post, 1, 3	0.5mL Saline	Administrated with a power injector over 20s.	0.36
9	SC	96	8.6	Day -2, Day 0 pre/post, 1, 2	0.5mL Saline	Administrated with a power injector over 20s.	0.33
10	SC	98	10.0	Day -2, Day 0 pre/post, 1, 2	0.5mL Saline	Administrated with a power injector over 20s.	0.39
11	IT	109	8.7	Day -1, Day 0 pre/post, 1, 2	10 μg IL-1β in 0.5mL sterile saline	Administrated with a power injector over 20s.	0.36

Note – UC=untreated control, IT=interleukin 1beta treated, SC=saline control, IL-1β=interleukin 1beta, No.=number
Day -2/-1: Two or one day before ferumoxytol administration; Day 0 pre/post: Before and immediately after ferumoxytol administration; Day 1/2/4/7/12/14/21/25: 1/2/4/7/12/14/21/25 days after ferumoxytol administration.

Table 5. Scan parameters of animal study in ferumoxytol placental imaging. Scan parameters of maternal pelvic MRI (SGRE) and maternal abdominal MRI (UTE-SGRE) of the animal.

	# TE	$TE_{init}/\Delta TE$ (ms)	TR (ms)	Flip Angle (°)	Field of View (mm^3)	Acquired Resolution (mm^3)	Reconstructed Resolution (mm^3)	Parallel Imaging Acceleration Phase/Slice	Scan Time (minutes)
Maternal pelvic MRI: SGRE	8	1.6/1.3	12.9	9	160×160×140	1.1×1.1×1.9	0.6×0.6×1.9	1.5 / 1.0	4:51
Maternal abdominal MRI: UTE-SGRE	3	0.1/0.2	2.8	3	180×180×180	1.4×1.4×1.4	1.4×1.4×1.4	1.0 / 1.0	5:30

SGRE=spoiled gradient-echo, UTE=ultra-short echo time

Table 6. ROI measurements in the placental imaging.

Parameters	Position	Region of Interest size (cm^2)
Amniotic fluid R_2^*	A region with homogenous R_2^*	~0.6
Fetal liver R_2^*	Right lobe of the liver	~0.1
Fetal lung R_2^*	Central region in one of the fetal lungs	~0.1
Placental R_2^*	Two ROIs in two separate placental discs	~0.6
Maternal liver R_2^*	Right lobe of the liver avoiding large vessels or bile ducts and the dome of the liver	~0.6
Fetal liver susceptibility	One ROI in the fetal liver and one in the adjacent amniotic fluid	~0.1
Placental susceptibility	One ROI in one of the placental discs and one in the adjacent amniotic fluid	~0.1

4.3 Results

One animal in the UC group (Rhesus #9) and one in the IT group (Rhesus #4) which had a history of ocular swelling not associated with ferumoxytol were noted to have moderate periocular swelling/edema following the ferumoxytol administration. They were treated with 10mg diphenhydramine hydrochloride and recovered without further medical intervention. No complications were observed in all the other animals during or after ferumoxytol administration. 3D SGRE acquisitions of the maternal pelvis were successfully obtained without apparent motion artifacts in the reconstructed R_2^* and susceptibility maps, except for the Day 0-pre acquisition in Rhesus #2 when the respiratory gating failed. 3D UTE-SGRE MRI of maternal abdomen was successfully obtained at most time points as listed in **Table 7**.

The MRI scan time points for Rhesus #3 in the UC group, Rhesus #4 in the IT group and Rhesus #5 in the SC group are shown at the top of **Figure 17** and **Figure 18**. Anatomic images, R_2^* maps, and susceptibility maps are shown at each scan time point for each animal. The fetal liver (red lines), the fetal lung (pink lines), the maternal liver (white lines), the uterine cavity (yellow lines), the two separate placental discs (orange lines), and the amniotic fluid (green arrows) are delineated and indicated in **Figure 17** and **Figure 18**. Placental R_2^* and susceptibility measurements of animals in all groups increased substantially after ferumoxytol administration (Day 0-post) and decreased towards baseline at Day 1 and afterwards. Maternal liver R_2^* in Rhesus #3 increased immediately after ferumoxytol administration (Day 0-post), further increased at one-day follow-up (Day 1), and subsequently decreased but remained elevated three weeks afterwards (Days 7-21).

Longitudinal measurements and changes from baseline in R_2^* of the amniotic fluid, R_2^* and susceptibility of fetal liver and R_2^* of fetal lung in all animals are summarized in **Figure 19** and **Table 8**. Stable R_2^* measurements of the amniotic fluid before and after ferumoxytol administration indicated no ferumoxytol deposition there. It further indicated the amniotic fluid to be a reliable reference tissue for the susceptibility measurement. In the UC group, a slope of 0.3 s^{-1}/day (P=0.008) and a slope of 0.00 ppm/day (P=0.699) were observed in fetal liver R_2^* and susceptibility, respectively. A slope of -0.2s^{-1}/day (P=0.023) was observed in fetal lung R_2^*. An intercept of -0.09 ppm (P=0.003) was observed in susceptibility of fetal liver in the IT group compared to the measurements in the UC group. The remaining measurements of R_2^* and susceptibility in the fetal liver and the fetal lung in the SC and IT groups were not significantly different from the reference, i.e., the UC group.

The maximum increase in R_2^* in the amniotic fluid among all animals over all scan time points after ferumoxytol administration was 13.7 s^{-1}. Assuming the change in R_2^* was due to the presence of ferumoxytol, then 13.7 s^{-1} corresponds to an iron concentration of 0.009 mg/mL. Assuming that amniotic fluid has a density of 1 g/cm^3, an iron concentration of 0.009 mg/mL corresponds to 9.0 micrograms iron per gram of tissue. The maximum change in fetal liver R_2^* after ferumoxytol administration among all animals at all scan times was 11.8 s^{-1}. Assuming the change in fetal liver R_2^* was due to the presence of ferumoxytol, then 11.8 s^{-1} corresponds to an iron concentration of 0.008 mg/mL. Using the approximated density 1.15 g/cm^3 for fetal liver tissue[100], an iron concentration of 0.008 mg/mL corresponds to 7.0 micrograms iron per gram of tissue. The maximum change in fetal lung R_2^* after ferumoxytol administration among all animals at all scan times was 7.1 s^{-1}. Assuming the change in fetal lung R_2^* was due to the presence of ferumoxytol, then 7.1 s^{-1} corresponds to an iron concentration of 0.005 mg/mL. Using the

approximated density 1.15 g/cm^3 for fetal lung tissue[101], an iron concentration of 0.005 mg/mL corresponds to 4.3 micrograms iron per gram of tissue. The maximum change in fetal liver susceptibility after ferumoxytol administration among all animals at all scan times was 0.19 ppm. Assuming the change in fetal liver susceptibility was due to the presence of ferumoxytol, then 0.19 ppm corresponds to an iron concentration of 0.006 mg/mL. Using the approximated density 1.15 g/cm^3 for fetal liver tissue[101], an iron concentration of 0.006 mg/mL corresponds to 5.2 micrograms iron per gram of tissue. Based on previous published calibrations in phantoms[18,98,99,101], the additional iron deposition after maternal ferumoxytol exposure, indicated by the MRI measurements, is less than 9.0, 7.0 and 4.3 micrograms iron per gram of tissue in the amniotic fluid, the fetal liver and the fetal lung, respectively**.**

Longitudinal measurements and changes from baseline in placental R_2^* and susceptibility and R_2^* of maternal liver in the UC group are summarized in **Figure 20** and **Table 9**. Example ROIs are shown in a previous study[102]. Placental R_2^* and susceptibility increased significantly after ferumoxytol administration at Day 0-post (P<0.001). Placental R_2^* and susceptibility at Day 1 decreased back to the baseline and showed no significant differences at all four follow-up scans (P=0.395, P=0.627, P=0.905 and P=0.559 in R_2^*, respectively, and P=0.172, P=0.859, P=0.974 and P=0.948 in susceptibility, respectively). Maternal liver R_2^* increased after ferumoxytol administration at Day 0-post (P<0.001), further increased at one-day follow-up (P<0.001) and decreased but remained elevated at all three follow-up scans (P<0.001).

Longitudinal measurements and changes from baseline in placental R_2^* and susceptibility and maternal R_2^* in the SC and IT groups are summarized in **Figure 21** and **Table 10**. After administration of either saline or IL-1β measured at Day 0-pre, placental R_2^* and susceptibility did not significantly change. Immediately after ferumoxytol administration, placental R_2^* and

susceptibility in both groups increased significantly ($P<0.001$). At one-day follow-up, placental R_2^* and susceptibility decreased towards baseline but remained elevated in both groups. At two- or three- day follow-up, placental R_2^* and susceptibility further decreased towards baseline in both groups. At all the time points, the mean change of either placental R_2^* or susceptibility from baseline showed no significant difference between the SC group and the IT group.

The maximum change in placental R_2^* after ferumoxytol administration among all animals at Day 2/3 was 25.0 s^{-1}. Assuming the change of placental R_2^* was due to the presence of ferumoxytol, then 25.0 s^{-1} corresponds to an iron concentration of 0.016 mg/mL. Using the approximated density 0.98 g/cm^3 for the placental tissue[103], an iron concentration of 0.016 mg/mL corresponds to 16.3 micrograms iron per gram of tissue. Based on previous published calibrations in phantoms[18,98,99,100], the maximum increase of R_2^* at Day 2/3 relatively to the baseline in all animals indicated a maximum iron concentration of 16.3 micrograms iron per gram of placental tissue.

Maternal liver R_2^* was not significantly altered after administration of either saline or IL-1β measured at Day 0-pre. Immediately after ferumoxytol administration, maternal liver R_2^* increased significantly in both groups ($P<0.009$). At one-day follow-up, maternal liver R_2^* further increased in both groups. At two- or three- day follow-up, maternal liver R_2^* decreased but remained elevated in both groups. At all the time points, the mean change of maternal liver R_2^* from baseline showed no significant difference between the SC group and the IT group.

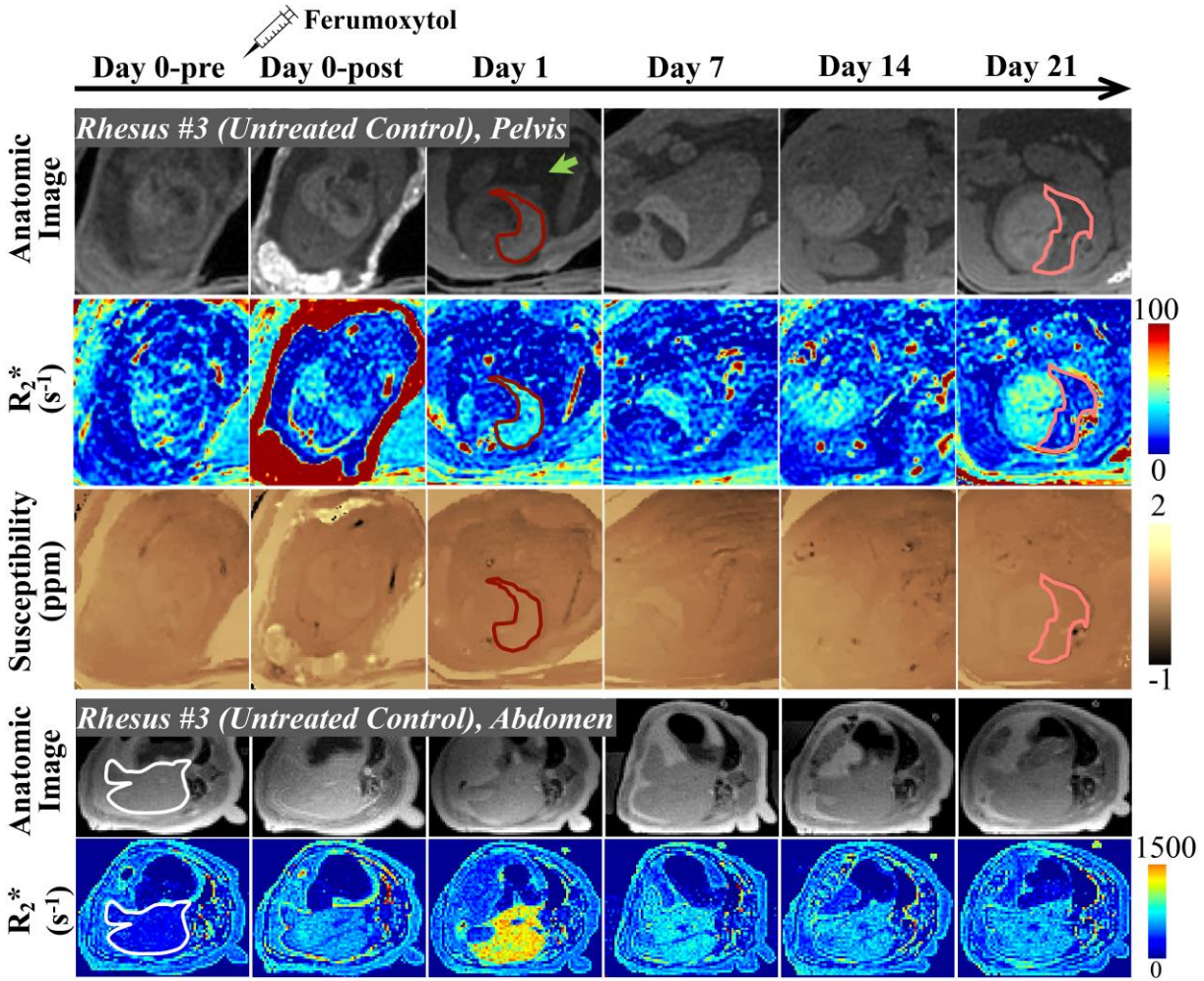

Figure 17. Longitudinal imaging of the fetus after maternal ferumoxytol administration. Longitudinal axial anatomic image (1st and 4th row), R_2^* (2nd and 5th row) and susceptibility (3rd row) maps of fetal liver (red lines), fetal lung (pink lines) and maternal liver (white lines) of Rhesus #3 (day 91 of gestation) in the untreated control group. Stable R_2^* and susceptibility of fetal tissues after maternal ferumoxytol administration were observed. Maternal liver R_2^* increased after ferumoxytol administration, further increased at one-day follow-up (Day 1), and remained elevated at seven-, fourteen, and twenty-one day follow-up.

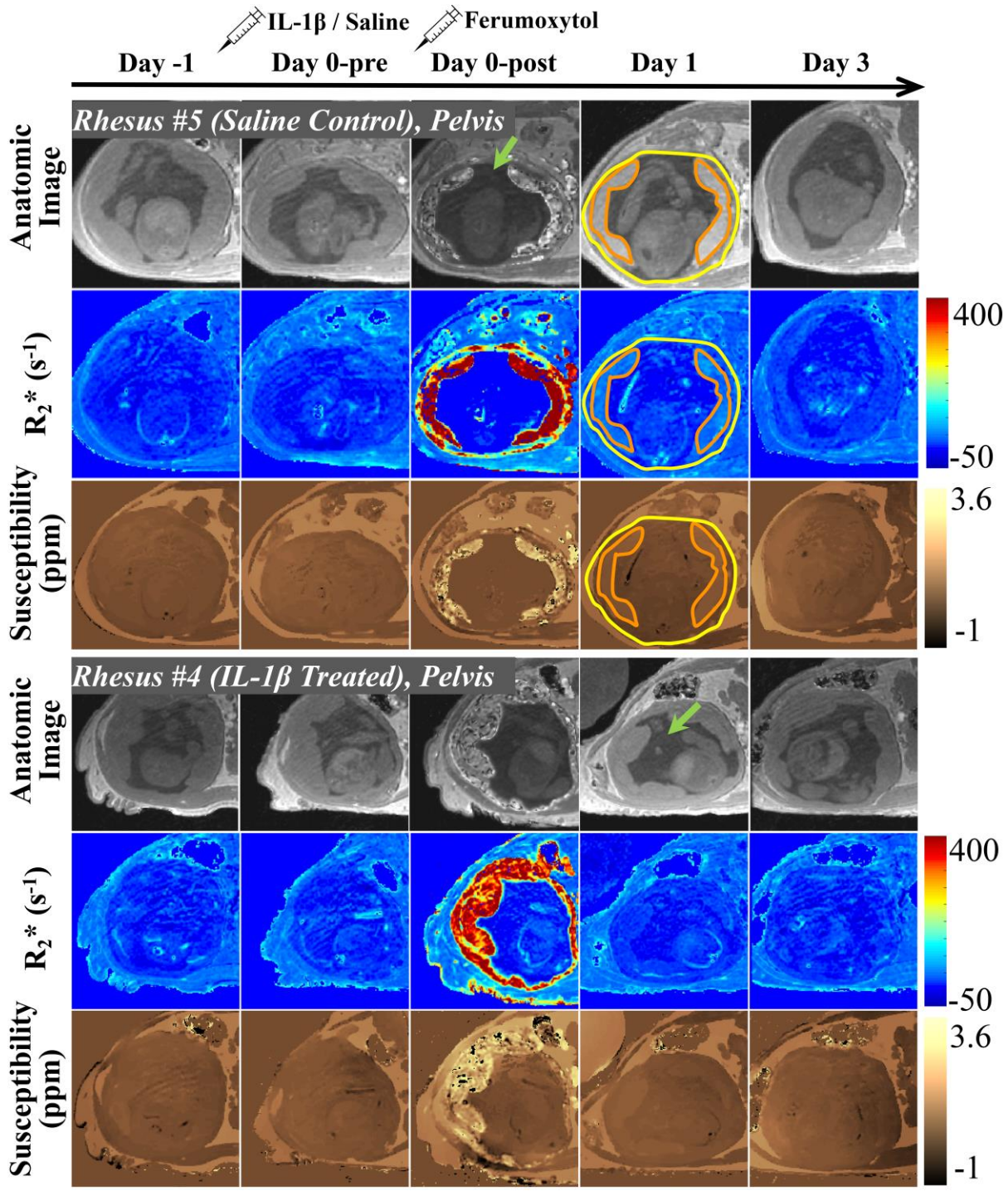

Figure 18. Longitudinal placental R_2^* and susceptibility mapping of animals. Placental R_2^* and susceptibility of Rhesus #5 (day 103 of gestation, bottom three rows) in the saline control group and Rhesus #4 (day 92 of gestation, top three rows) in the interleukin 1 beta (IL-1β) treated group increased after ferumoxytol administration (at Day 0-post) and decreased towards baseline at Day 1 and afterwards. The amniotic fluid is indicated by green arrow. The uterus cavity and the two separate placental discs are delineated by yellow lines and orange lines, respectively.

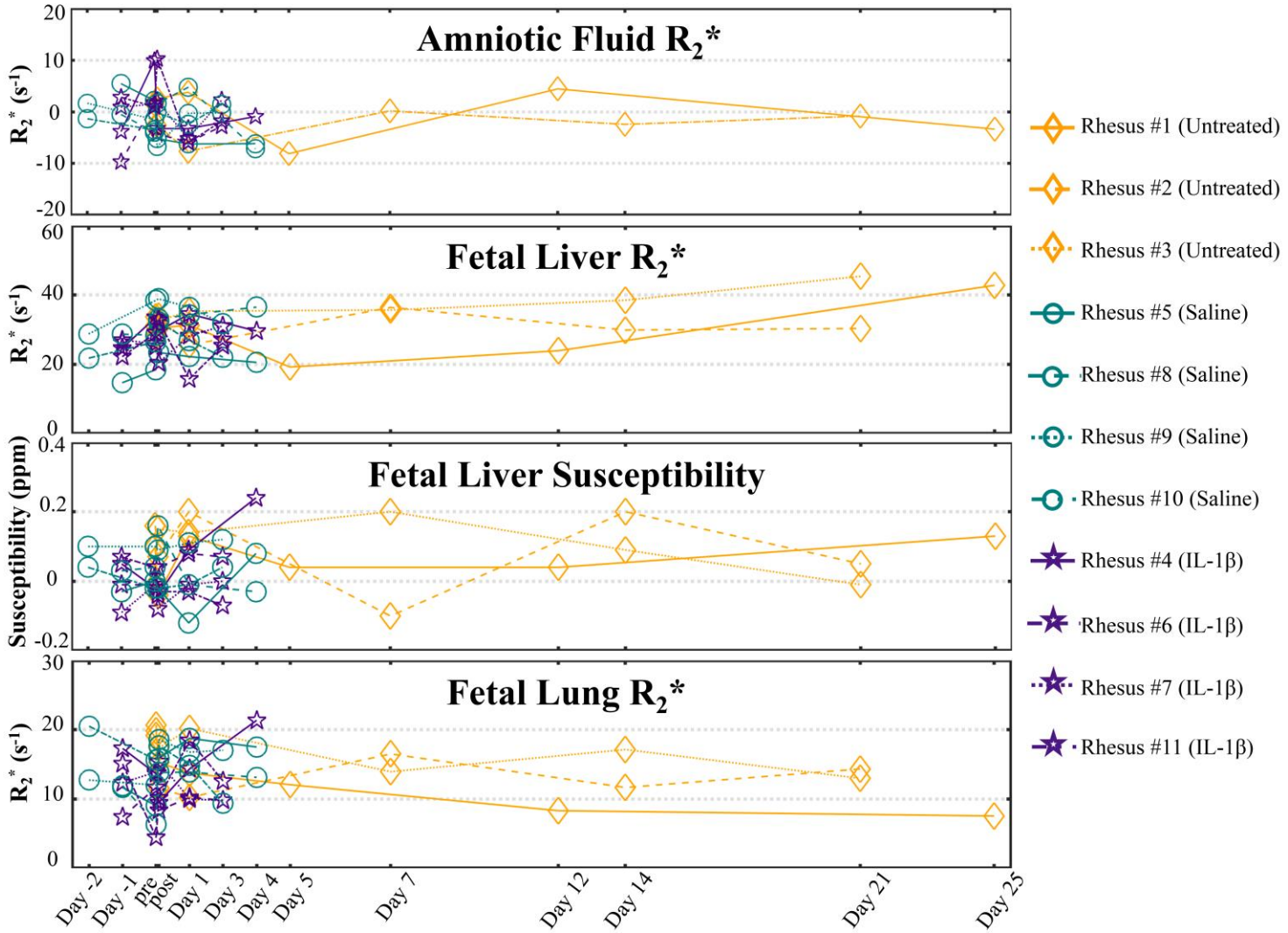

Figure 19. R_2^* and susceptibility measurements of fetal tissues. Stable R_2^* measurements of the amniotic fluid indicate no ferumoxytol uptake, suggesting the amniotic fluid as a reliable reference tissue for the susceptibility measurement. Fetal liver R_2^* and susceptibility measurements and fetal lung R_2^* measurements in all animals are not significantly increased over time after maternal ferumoxytol administration at Day 0-post.

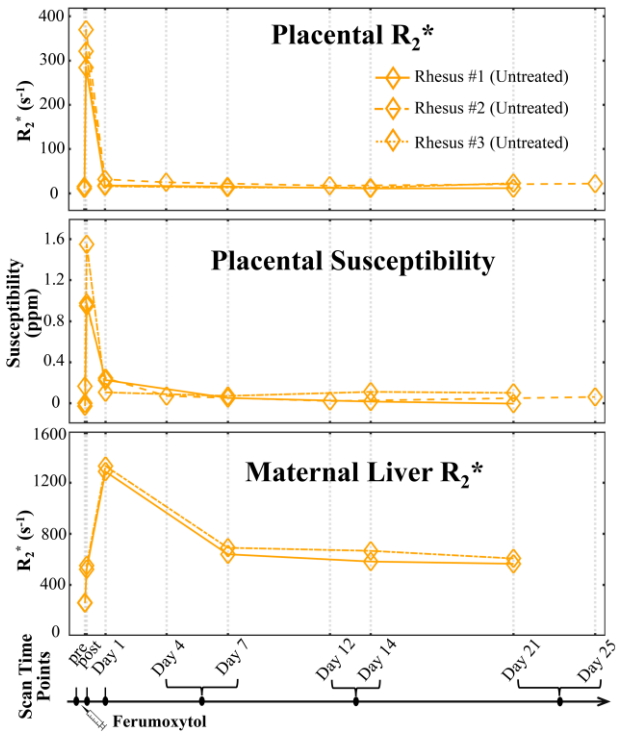

Figure 20. Longitudinal placental MRI measurements in the UC group. Longitudinal measurements of placental R_2^* and susceptibility and maternal liver R_2^* in the untreated control group. Both the placental R_2^* and susceptibility increased significantly after ferumoxytol administration at Day 0-post and decreased back to the baseline at follow-up scans. Maternal liver R_2^* increased after ferumoxytol administration and remained elevated at follow-up scans.

Table 7. Scan time points of maternal pelvic and abdominal MRI.

Rhesus No.	Groups	Day -2	Day -1	Day 0-pre	Day 0-post	Day 1	Day 2	Day 3	Day 4	Day 7	Day 12	Day 21	Day 25
1	UC			✓	✓	✓			✓		✓		✓
2	UC			✓○	✓○	✓○				✓○		✓○	
3	UC			✓○	✓○	✓○				✓○		✓○	
4	IT		✓○	✓○	✓○	✓○		✓○					
5	SC		✓○	✓○	✓○	✓○		✓○					
6	IT		✓○	✓○	✓	✓○	✓○						
7	IT		✓○	✓○	✓○	✓○	✓○						
8	SC		✓○	✓○	✓○	✓○		✓○					
9	SC	✓		✓○	✓	✓○	✓○						
10	SC	✓○		✓○	✓○	✓○	✓○						
11	IT		✓○	✓○	✓	✓○	✓○						

Note – ✓: maternal pelvic images acquired, ○: maternal abdominal images acquired, UC=untreated control, IT=IL-1β treated, SC=saline control, IL-1β=interleukin 1beta, No.=number

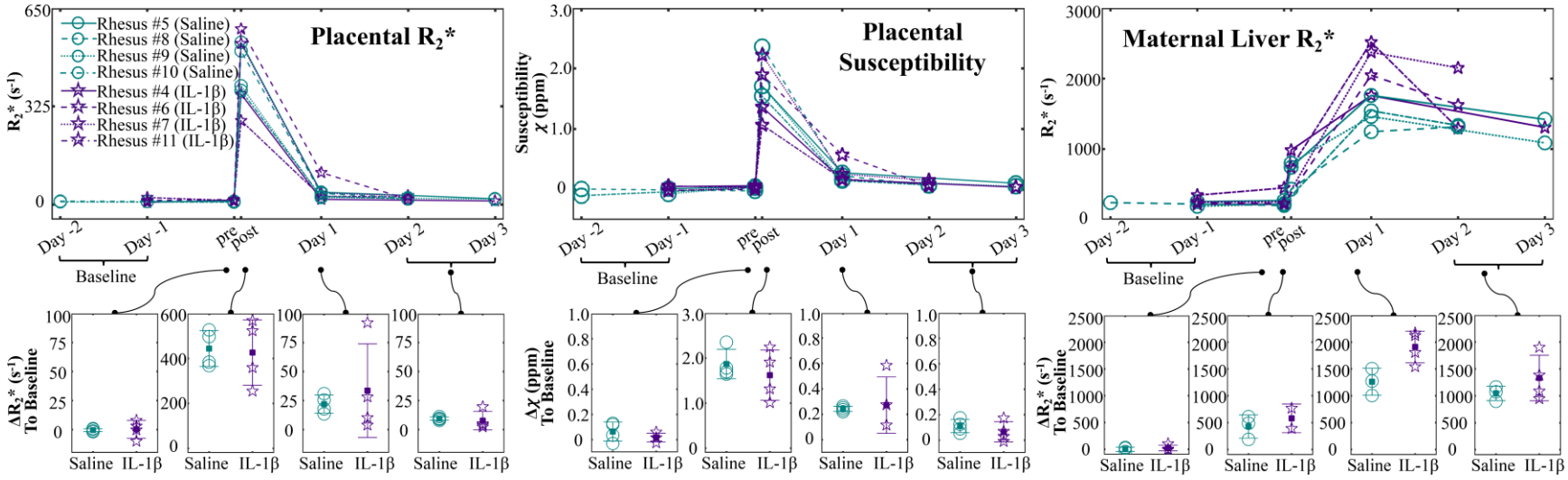

Figure 21. Longitudinal placental MRI measurements of animals in SC and IT groups. Placental R_2^* and susceptibility (χ) measurements of all animals in the saline control group and the interleukin 1 beta (IL-1β) treated group increased after ferumoxytol administration at Day 0-post and decreased back to the baseline at follow-up scans. The difference of measurements at each scan time point compared to that at baseline, i.e., ΔR_2^* and $\Delta\chi$, showed no difference between the saline control group and the IL-1β treated group. Maternal liver R_2^* in both groups immediately increased after ferumoxytol administration, further increased at Day 1, and remained elevated at Day 2 or Day 3.

Table 8. Statistical analysis on fetal MRI measurements in the UC group. Longitudinal variation of R_2^* and susceptibility measurements of the fetal liver and R_2^* measurements of the fetal lung over time in all animals.

	Estimated Change in Fetal Liver R_2^* (s^{-1})	*P* value	Estimated Change in Fetal Liver Susceptibility (ppm)	*P* value	Estimated Change in Fetal Lung R_2^* (s^{-1})	*P* value
UC Group (reference)	Intercept: 30.0 (25.1, 35.0)	<0.001	Intercept: 0.09 (0.05, 0.14)	<0.001	Intercept: 16.3 (14.0, 18.5)	<0.001
	Slope: 0.3 (0.1, 0.6)	0.008	Slope: 0.00 (-0.00, 0.00)	0.699	Slope: -0.2 (-0.4, 0.0)	0.023
SC Group	Intercept: -2.3 (-8.7, 4.2)	0.489	Intercept: -0.06 (-0.11, 0.00)	0.046	Intercept: -2.0 (-4.8, 0.8)	0.081
	Slope: 0.9 (-0.8, 2.2)	0.365	Slope: 0.00 (-0.03, 0.02)	0.886	Slope: 0.4 (-0.8, 1.6)	0.544
IT Group	Intercept: -2.7 (-9.2, 3.8)	0.411	Intercept: -0.09 (-0.15, -0.03)	0.003	Intercept: 4.5 (-0.6, 9.5)	0.081
	Slope: 0.3 (-1.5, 2.1)	0.765	Slope: 0.03 (0.00, 0.06)	0.057	Slope: 1.0 (-0.5, 2.4)	0.186

Data in parentheses are 95% confidence intervals, IL-1β=interleukin 1beta, UC=untreated control, IT= interleukin 1beta treated, SC=saline control

Table 9. Statistical analysis on placental R_2^* and susceptibility measurements. Estimated change of placental R_2^* and susceptibility measurements at scan time points after ferumoxytol administration from the baseline in the untreated control group.

	Estimated Change in Placental R_2^* (s^{-1})		Estimated Change in Placental Susceptibility (ppm)		Estimated Change in Maternal Liver[Π] R_2^* (s^{-1})	
	Intercept	*P* value	Intercept	*P* value	Intercept	*P* value
Day 0-pre vs. Day 0-post	312.8 (289.6, 335.9)	<0.001	1.1 (0.9, 1.3)	<0.001	276.8 (217.1, 301.0)	<0.001
Day 0-pre vs. Day 1	9.4 (-13.8, 32.6)	0.395	0.2 (-0.1, 0.4)	0.172	1049.4 (1013.8, 1085.0)	<0.001
Day 0-pre vs. Day 4/7	5.3 (-17.9, 28.5)	0.627	0.0 (-0.2, 0.2)	0.859	405.2 (369.6, 440.8)	<0.001
Day 0-pre vs. Day 12/14	1.3 (-21.9, 24.5)	0.905	0.0 (-0.2, 0.2)	0.974	364.7 (329.0, 400.3)	<0.001
Day 0-pre vs. Day 21/25	6.4 (-16.8, 29.6)	0.559	0.0 (-0.2, 0.2)	0.948	326.2 (290.6, 361.8)	<0.001

Data in parentheses are 95% confidence intervals, vs.=versus, [Π]Data of Rhesus #1 in the untreated control group were not available at all scan time points and thus not included.

Table 10. Statistical analysis on placental MRI measurements in the SC and UT groups. Estimated change of placental R_2^* and susceptibility (χ) measurements at scan time points before and after ferumoxytol administration from the baseline in the saline control group and the untreated control group.

	Saline control (*n*=4)		**IL-1β treated (*n*=4)**		**SC vs. IT**
	Estimated Change Placental ΔR_2^* (s^{-1})	***P* value**	**Estimated Change Placental ΔR_2^* (s^{-1})**	***P* value**	***P* value**[Π]
Day 0-pre vs. Day -1/-2	-0.5 (-47.3, 46.4)	0.984	0.2 (-82.1, 82.5)	0.996	0.867
Day 0-post vs. Day -1/-2	444.0 (397.1, 490.8)	<0.001	426.3 (343.9, 508.6)	<0.001	0.824
Day 1 vs. Day -1/-2	21.9 (-24.9, 68.8)	0.338	33.6 (-48.7, 115.9)	0.398	0.598
Day 2/3 vs. Day -1/-2	9.4 (-37.4, 56.3)	0.677	7.7 (-74.7, 90.0)	0.845	0.733
	Estimated Change Placental $\Delta\chi$ (ppm)	***P* value**	**Estimated Change Placental $\Delta\chi$ (ppm)**	***P* value**	***P* value**[Π]
Day 0-pre vs. Day -1/-2	0.06 (-0.15, 0.28)	0.541	0.02 (-0.31, 0.34)	0.917	0.339
Day 0-post vs. Day -1/-2	1.87 (1.60, 2.13)	<0.001	1.62 (1.29, 1.95)	<0.001	0.385
Day 1 vs. Day -1/-2	0.24 (-0.02, 0.51)	0.031	0.27 (-0.05, 0.60)	0.095	0.818
Day 2/3 vs. Day -1/-2	0.11 (-0.11, 0.33)	0.293	0.07 (-0.26, 0.39)	0.671	0.402
	Estimated Change Maternal Liver ΔR_2^* (s^{-1})	***P* value**	**Estimated Change Maternal Liver ΔR_2^* (s^{-1})**	***P* value**	***P* value**[Π]
Day 0-pre vs. Day -1/-2	3.5 (-211.9, 218.8)	0.972	24.6 (-317.9, 367.1)	0.879	0.591
Day 0-post vs. Day -1/-2	429.8 (214.5, 645.2)	0.001	598.9 (179.5, 1018.4)	0.009	0.534
Day 1 vs. Day -1/-2	1261.4 (1046.0, 1476.7)	<0.002	1910.3 (1567.8, 2252.8)	<0.001	0.028
Day 2/3 vs. Day -1/-2	1046.9 (831.6, 1262.3)	<0.001	1331.4 (988.9, 1673.9)	<0.001	0.320

Data in parentheses are 95% confidence intervals, IL-1β=interleukin 1beta, vs.=versus, SC=saline control, IT= IL-1β treated

[Π]Data were compared by using the Student's t-test with conservative Bonferroni correction for multiple comparison. Threshold for statistical significance was set to $P<0.0125$ after correction.

4.4 Discussion

This work demonstrated the feasibility of R_2^* mapping and QSM to measure the ferumoxytol delivery and washout from the placental tissues. Additionally, stable R_2^* and tissue susceptibility were observed in fetal tissues before and after ferumoxytol administration in nonhuman primates, indicating no increased iron deposition in the fetus after maternal exposure.

The elevated maternal liver R_2^* immediately after ferumoxytol administration and the further increase of R_2^* at one-day follow-up were likely due to the presence of ferumoxytol in the blood pool[88,103]. Maternal liver R_2^* decreased subsequently over the following three weeks, but did not return to the baseline over this time span. This suggests iron uptake in the maternal liver as expected to occur following ferumoxytol administration in treatment of anemia[103].

The elevated placental R_2^* and susceptibility immediately after ferumoxytol administration were also likely due to the presence of ferumoxytol in the blood pool[88,104]. At one-day follow-up, placental R_2^* and susceptibility remained elevated, most likely due to the remaining ferumoxytol in the blood pool[88,104]. Further, the lack of significantly elevated placental R_2^* at one-, two- or three- day follow-up, compared to the elevated maternal liver R_2^*, indicated a lack of ferumoxytol uptake in the placenta.

Importantly, the lack of significant amount of iron deposit in fetal tissues, compared to the iron uptake in the maternal liver, suggests that ferumoxytol does not cross into the amniotic cavity and may not enter the fetal circulation. This is an important observation towards evaluating the safety implications for the use of ferumoxytol in pregnancy. However, delayed effects of elevated iron content in the maternal body (as shown in maternal liver R_2^*) on the fetus are unknown. To further investigate the safety of the ferumoxytol use in pregnancy, future studies are needed to

assess iron contents in offspring with in utero exposure to ferumoxytol. In addition, ferumoxytol administration in animals at different gestation stages also need to be studied.

In the UC group, slightly elevated R_2^* measurements were observed in the fetal liver over time after maternal ferumoxytol exposure. However, a previous study has shown an increase of human fetal liver R_2^* over gestation stage in normal fetuses without maternal ferumoxytol exposure[105]. It cannot be determined from the current study whether the elevated fetal liver R_2^* is due to the normal development of the reticuloendothelial system over gestation stage[106,107], or due to the maternal exposure of ferumoxytol. Quantification of iron content in fetuses without maternal ferumoxytol exposure is under separate study[108].

Tissue R_2^* and susceptibility measurements were both obtained as potential imaging biomarkers of iron content in this study. In the placenta, both R_2^* and susceptibility measurements showed consistent behavior after ferumoxytol administration, even though R_2^* and susceptibility may have different dependence on the presence of iron[77]. The fact that R_2^* and susceptibility can be obtained as separate measurements from the same 3D SGRE data may enable a comprehensive evaluation of iron content and microscopic iron distributions[69] in a single acquisition.

This study has several limitations. The IL-1β treatment was ineffective at inducing the pathology reported in a previous study[109] where neutrophil and macrophage infiltration of the decidua parietalis was demonstrated. However, in this previous study the decidua basalis or the placenta itself was not evaluated; it is possible that the inflammatory response on the maternal side is limited to fetal membranes. With the MRI techniques in this study, it was not possible to resolve the thin fetal membranes and decidua parietalis. The potential use of ferumoxytol-enhanced MRI for the detection of macrophage homing to the decidua basalis and placenta needs further validation in an effective macrophage homing inflammation model. Additionally, a larger

population of animals is needed to capture the biological variation on the iron biodistribution after maternal ferumoxytol exposure.

4.5 Conclusion

In conclusion, this study demonstrated the feasibility of longitudinal tracking of placental iron content in ferumoxytol-enhanced MRI. Additionally, this study suggested ferumoxytol may not cross the placenta and hence enter into the amniotic cavity or into the fetal circulation after maternal ferumoxytol exposure in nonhuman primates at late second trimester. Upon successful detection of macrophage homing in an effective inflammation model and being proven safe, ferumoxytol-enhanced MRI may enable assessment of the inflammation at the maternal-fetal interface in human pregnancy.

Chapter

5. Evaluation of a Motion-robust 2D Chemical Shift-Encoded Technique for R_2^* and Field Map Quantification‡‡

5.1 Introduction

In the pathologies of preeclampsia, an inflammatory condition of pregnancy that can lead to edema, hypertension, seizures and even death, altered immune cell (e.g. macrophage) activation and distribution at the implantation site may play an important role[84]. The FDA-approved iron supplement ferumoxytol is an ultra-small superparamagnetic oxide iron nanoparticle (SPION) which is transported in blood after intravenous infusion[110], accumulates in organs like the liver and spleen, and is phagocytosed by activated macrophages over a period of days. Ferumoxytol leads to increases in R_1 and R_2^* relaxation rates, and its magnetic susceptibility effects can also be quantified through B_0 field measurement-based techniques.

---

‡‡ This work has been published in: Zhu A, Reeder SB, Johnson KM, Nguyen S, Golos TG, Shimakawa A, Muehler MR, Francois CJ, Bird IM, Fain SB, Shah DM, Wieben O, Hernando D. Evaluation of a motion-robust 2D chemical shift-encoded technique for R_2^* and field map quantification in ferumoxytol-enhanced MRI of the placenta in pregnant rhesus macaques. *J Magn Reson Imaging.* 2019. doi:10.1002/jmri.26849.

A previously proposed 3D chemical shift-encoded (CSE) MRI method has been demonstrated to enable R_2^* mapping-based and B_0 mapping-based assessment of different iron concentrations in SPION phantoms[20], ferumoxytol-enhanced brain MRI[21,22] and body iron deposition[4,20,23]. Therefore, ferumoxytol-enhanced CSE-MRI may enable non-invasive and sensitive detection of increased macrophage density in inflammation at the maternal-fetal interface, similar to what has been shown in other investigations including inflammation of the central nervous system, aortic walls, kidneys, pancreas and others[19,24].

Maternal respiratory and fetal motion in the uterus are challenges for imaging the placenta with MRI[25] and their effects should be addressed in order to minimize bias and maximize precision in CSE-MRI. Imaging acquisition in a breath-hold has been shown to reduce respiratory motion artifacts in 3D CSE-MRI[42]. However, breath-hold requirements may reduce the comfort of pregnant patients and the corresponding scan time constraints may limit the achievable spatial resolution and image signal-to-noise ratio (SNR). Respiratory-gated[111,112] and free-breathing non-Cartesian acquisition techniques[26,47] have been applied in body 3D CSE-MRI during free-breathing and shown to be motion robust.

Compared to 3D CSE-MRI which has a long temporal footprint, e.g., a typical scan time of ~5 minutes in respiratory-gated imaging and ~3 minutes in free-breathing imaging[26], 2D CSE-MRI with sequential phase encoding has a short temporal footprint. It enables acquisition of images in a single slice in ~3 seconds[27], as shown in **Figure 22**. This strategy is expected to freeze motion or contain the motion effects to a limited number of slices[28,29]. 2D MRI-based R_2^* mapping has been applied in the placenta using breath-hold acquisitions[113,114]. Free-breathing 2D CSE-MRI in the liver has been demonstrated to enable accurate measurements on proton density fat fraction (PDFF), an imaging biomarker of fat content that can be quantified simultaneously with R_2^* and

B_0 field in CSE-MRI techniques[27]. Therefore, free-breathing 2D CSE-MRI may also enable reliable R_2^* and B_0 field measurements in the presence of both maternal respiratory motion and fetal motion. Furthermore, motion-robust R_2^* mapping using 2D CSE-MRI, as evaluated in this work, may also enable reliable assessment of placental health with endogenous contrast, including blood oxygenation level dependent (BOLD)-based placental functional imaging[30].

However, the accuracy of the free-breathing 2D CSE-MRI technique for quantification of R_2^* and B_0 field in ferumoxytol-enhanced MRI of the placenta has not yet been validated and compared to the standard 3D CSE-MRI. Maternal respiratory motion and fetal motion need to be minimized in 3D CSE-MRI in order to provide a reliable reference of R_2^* and B_0 field measurements. Ferumoxytol-enhanced MRI of the nonhuman primate, who has the most similar placentation and immunology with the human reproductive system[95,96], would be an important step towards evaluating the feasibility of ferumoxytol-enhanced MRI in human pregnancy. Furthermore, the primate mother is anesthetized during the scan, which also anesthetizes the fetus, thereby minimizing fetal motion. This enables reliable imaging with the standard 3D CSE-MRI using respiratory gating, which further minimizes the effect of maternal respiratory motion. Thus, ferumoxytol-enhanced MRI of the animals under general anesthesia enables in vivo evaluation of the accuracy of 2D CSE-MRI in the presence of maternal respiratory motion, by comparing to the reference 3D respiratory-gated CSE-MRI.

In summary, the purpose of this study was to evaluate the accuracy of 2D CSE-MRI technique for quantification of R_2^* and B_0 field in ferumoxytol-enhanced MRI of the placenta in pregnant rhesus macaques as well as in ferumoxytol phantoms. The secondary purpose was to preliminarily evaluate the motion artifacts and repeatability for placental R_2^* mapping enabled by 2D CSE-MRI in pregnant women without ferumoxytol administration.

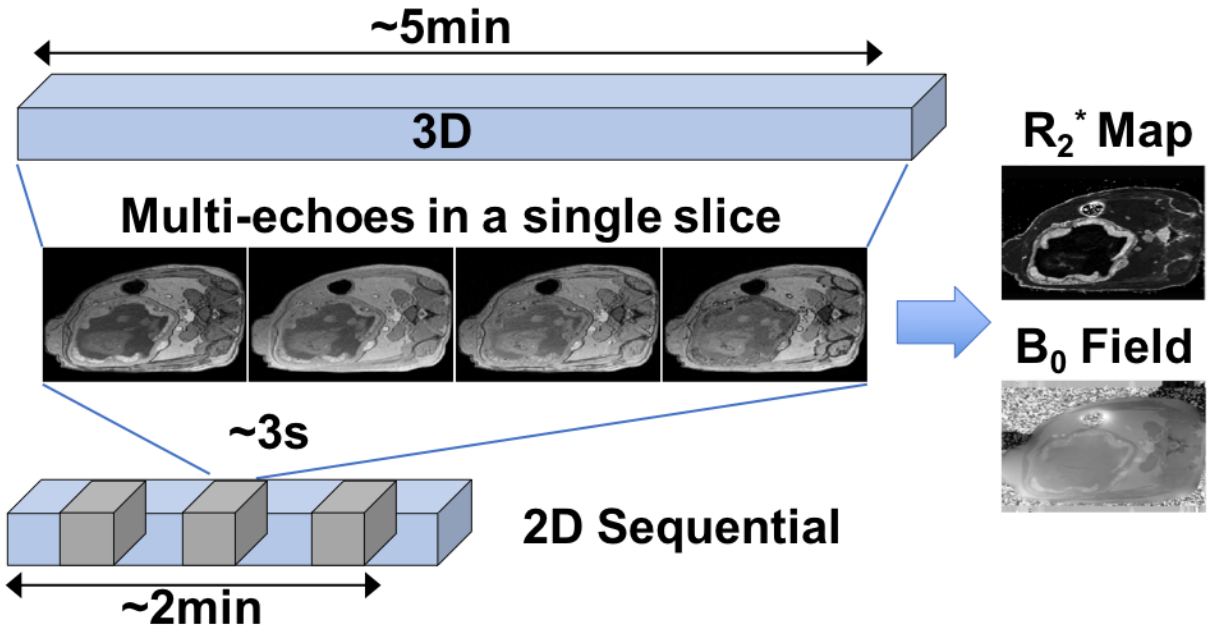

Figure 22. Temporal footprint of 2D-sequential and 3D CSE-MRI acquisitions. In the proposed 2D sequential acquisition, the scan time for one slice image is only ~ 3 seconds. In the reference 3D acquisition (including respiratory gating), however, one slice image is reconstructed in a ~5 minutes scan.

5.2 Methods

5.2.1 Materials and Subjects

Phantoms

A phantom with varying R_2^* and magnetic susceptibilities was constructed using ferumoxytol (Feraheme, AMAG Pharmaceuticals Inc., Cambridge, MA). Eight cylindrical 40 mL vials (diameter=20 mm) with varying concentrations of ferumoxytol ranging from 0 µg/mL-440 µg/mL, prepared in an agar gel (2% agar weight/volume, 3 mM sodium benzoate, 43 mM NaCl) were built and were separated into two batches, which were scanned sequentially. Four vials in each batch were placed in a holder within a cylindrical plastic container filled with distilled water.

Phantoms were placed in the scanner with the long axis of the vials parallel to the main magnetic field. A hemisphere photopolymer resin phantom with the same radius as the cylindrical plastic container was attached to the bottom wall of the cylindrical container to reduce magnetic susceptibility effects at the interface.

Animals

All procedures were approved by our institution's animal care and use committee (IACUC). In this study, 2D CSE-MRI and 3D CSE-MRI acquisitions were obtained and compared in ferumoxytol-enhanced MRI of pregnant rhesus macaques, who normally have two placental discs, one primary large disc and one secondary smaller disc[115]. The two discs are attached to the anterior and posterior uterus walls[116], separately, which were named as anterior placental disc and posterior placental disc in this study.

Eleven pregnant rhesus macaque monkeys at their late second trimester based on an average 165 days pregnancy length (gestational age=98.7±5.9 days, maternal weight=8.8±1.1kg, normal singleton) in a study of inflammation at the maternal-fetal interface[26] were scanned. Each animal was imaged at multiple time points before and after administration of ferumoxytol by intravenous infusion. In each scan session, the animal was anesthetized by administration of up to 10 mg/kg ketamine. Oxygen with 1.5% isoflurane was delivered through inhalation during the scan for prolonged sedation. Ferumoxytol was administered at a dose of 4 mg/kg diluted 5:1 with sterile saline solution. Animals were monitored during and after imaging until fully recovered from anesthesia. Detailed animal information, and details on drug dose and ferumoxytol administration are shown in **Table 4**.

Humans

Additionally, two preliminary human placental studies, including a motion assessment study and a repeatability study, were performed.

The motion artifacts of 2D CSE-MRI compared to 3D CSE-MRI were preliminarily evaluated in human scans by retrospectively analyzing images in a HIPAA compliant human placental study, approved by the local Institutional Review Board (IRB). Pregnant women with singleton in normal pregnancy were recruited. Exclusion criteria included subjects with any previous pregnancy conditions, including hypertension, preeclampsia, or diabetes. In this study, pregnant women at 20-22 weeks of gestation were scanned after obtaining informed written consent. MR images of ten human subjects were evaluated. Details on the subject information are shown in **Table 12**.

Further, the repeatability of 2D and 3D CSE-MRI for placental R_2^* mapping was also preliminarily evaluated in seven pregnant women scans at either 14-15 or 20-22 weeks of gestation in the human placental study above. Details on the subject information are shown in **Table 13**.

5.2.2 Imaging Protocol

Phantom and animals were imaged using a clinical 3.0T MRI system (GE Healthcare Discovery MR 750, Waukesha, WI) with a 32-channel phased array torso coil (Neocoil, Pewaukee, WI). Pregnant women were imaged using a clinical 1.5T MRI system (GE Healthcare Optima MR450w, Waukesha, WI) without contrast agent administration.

Phantoms

In the phantom study, a multi-echo spoiled gradient-echo (SGRE) 2D acquisition ("2D CSE-MRI") and a multi-echo SGRE 3D acquisition ("3D CSE-MRI") were used. The scan

parameters for these 2D and 3D CSE-MRI acquisitions were chosen such that SNR (SNR=35 in 2D CSE-MRI, SNR=60 in 3D CS-MRI) approximately matched that observed in the 2D and 3D CSE-MRI acquisitions, respectively, in the animal study (described below). In addition, a 3D CSE-MRI acquisition with high SNR ("3D CSE-MRI high SNR", SNR=235), obtained by increasing slice thickness, was used as reference for both R_2^* and B_0 field measurements. A second 2D CSE-MRI acquisition with relatively high SNR ("2D CSE-MRI high SNR", SNR=90), obtained by increasing the number of averages, was also performed to assess 2D CSE-MRI while diminishing SNR-related effects on measurements. Details on the acquisition parameters of the four CSE-MRI acquisitions are listed in **Table 11**.

Animals

In the rhesus study, the animal was placed in the left lateral decubitus position in the MRI scanner. Scans at each time point included an axial 2D CSE-MRI acquisition without respiratory gating, designed for motion-robust ferumoxytol-enhanced CSE-MRI and performed in each animal covering the maternal uterus cavity. An axial 3D CSE-MRI acquisition with respiratory gating using maternal respiratory bellow signals was also acquired as the reference for CSE-MRI in the placenta. Details on the acquisition parameters of the two CSE-MRI acquisitions are listed in **Table 11**.

Humans

Each subject was scanned in supine position and the field of view was prescribed to cover the maternal uterus cavity. In the motion assessment study, R_2^* and B_0 field mapping were performed from two different acquisitions: an axial 3D CSE-MRI with respiratory gating using maternal respiratory bellow signals, and a free-breathing axial 2D CSE-MRI which was acquired

approximately 20 minutes after the 3D CSE-MRI scan. In addition, a 2D multi-slice T_2-weighted single-shot fast spin-echo (SSFSE) was acquired for anatomic imaging. Details on the scan parameters are shown in **Table 11**. In the repeatability study, the 3D respiratory-gated CSE-MRI and the free-breathing 2D CSE-MRI were performed sequentially at the beginning of the exam. The two sequences were repeated 20 minutes afterwards. A 2D multi-slice T_2-weighted SSFSE was also acquired.

Table 11. Scan parameters of 2D and 3D CSE-MRI in placental MRI. Scan parameters of 2D CSE-MRI and 3D CSE-MRI in the phantom and animal studies at 3.0T and the preliminary human studies at 1.5T.

	# TE	TE_{init}/ΔTE (ms)	TR (ms)	FA (°)	FOV (mm^3)	ACQ Resolution (mm^3)	NOA	ACQ BW (kHz)	PI Acceleration Phase/Slice	Scan Time (minutes)	Temporal Footprint per Slice
Phantom Study (3.0T)											
2D CSE-MRI	16	1.8/1.0	18.9	9	220×220×69⁺	2.3×2.3×2.3⁺	1	±100	1.5 / 1.0	1:34	3.1 seconds
2D CSE-MRI high SNR	16	1.8/1.0	18.9	9	220×220×72⁺	2.3×2.3×3.0⁺	4	±62.5	1.5 / 1.0	6:13	15.5 seconds
3D CSE-MRI˟	8	1.6/1.3	12.8	9	220×220×68	1.5×1.5×1.2	1*	±62.5	1.5 / 1.0	1:40	1:40 minutes
3D CSE-MRI high SNR˟	8	1.6/1.3	12.8	9	220×220×72	1.5×1.7×8.0	1*	±143	1.5 / 1.5	0:38	0:38 minutes
Animal Study (3.0T)											
2D CSE-MRI	16	1.8/1.0	18.7	9	180×160×140⁺	1.9×1.8×3.0⁺	1	±62.5	1.5 / 1.0	2:11	2.8 seconds
3D CSE-MRI	8	1.6/1.3	12.9	9	160×140×140	1.1×1.0×2	1*	±62.5	1.5 / 1.0	4:54#	4:54 minutes#
Human Study (1.5T)											
2D CSE-MRI	12	1.5/0.8	12.7	10	420×378×224⁺	2.9×2.9×4.0	1	±62.5	1.5 / 1.0	2:14	2.4 seconds
3D CSE-MRI	6	1.2/2.0	13.9	9	420×378×228	2.2×2.2×3	1*	±83.3	2.0 / 1.5	1:48#	1:48 minutes
T_2 SSFSE	1	100/0	4000	155	380×380×210	1.5×1.5×5	1	±83.3	2.0 / 1.0	2:40	2.8 seconds

⁺Contiguous slices with slice gap=0 mm; ***** 3D corner cutting used (20% k-space reduction). ˟No respiratory gating used in phantom study. # Scan time with respiratory gating. CSE: chemical shift-encoded; FA: flip angle; FOV: field of view; ACQ: acquisition; NOA: number of averages; BW: sampling bandwidth; PI: parallel imaging; SSFSE: single-shot fast spin-echo

Table 12. Subjects' information in the preliminary motion assessment.

Subject #	Age (years)	Gestational Age (days)	Body Mass Index (kg/m^2)	Pregnancy Conditions
1	28	20 weeks 5 days	23.8	Single gestation, second pregnancy, live birth in the first pregnancy
2	32	21 weeks 4 days	31.4	Single gestation, second pregnancy, spontaneous abortion in the first pregnancy
3	30	21 weeks 1 day	28.2	Single gestation, first pregnancy
4	30	20 weeks 5 days	26.7	Single gestation, first pregnancy
5	33	21 weeks 3 days	23.3	Single gestation, second pregnancy, live birth in the first pregnancy
6	29	20 weeks 6 days	27.8	Single gestation, first pregnancy
7	32	21 weeks 1 day	27.4	Single gestation, first pregnancy
8	31	20 weeks 5 days	25.4	Single gestation, second pregnancy, indicated termination in the first pregnancy
9	31	21 weeks 3 days	21.2	Single gestation, third pregnancy, live birth in the first and second pregnancy
10	27	21 weeks 1 day	21.4	Single gestation, second pregnancy, spontaneous abortion in the first pregnancy

Table 13. Subjects' information in the preliminary repeatability study.

Subject #	Age (years)	Gestational Age (days)	Body Mass Index (kg/m^2)	Pregnancy Conditions
1	34	20 weeks 6 days	26.9	Single gestation, second pregnancy, live birth in the first pregnancy
2	27	15 weeks 5 days	24.4	Single gestation, second pregnancy, spontaneous abortion in the first pregnancy
3	31	22 weeks 0 day	25.6	Single gestation, first pregnancy
4	33	15 weeks 1 day	25.3	Single gestation, second pregnancy, live birth in the first pregnancy
5	31	14 weeks 2 days	20.2	Single gestation, first pregnancy
6	25	15 weeks 5 days	26.5	Single gestation, second pregnancy, live birth in the first pregnancy
7	34	15 weeks 1 day	21.5	Single gestation, second pregnancy, live birth in the first pregnancy

5.2.3 Imaging Reconstruction, Assessment and Measurements

In all CSE-MRI acquisitions, water and fat images, R_2^* and B_0 field maps were reconstructed through complex fitting of the multi-echo data using a multi-component signal model[97]. In phantom and animals, R_2^* and boundary B_0 measurements were obtained. The boundary B_0 field measurement, which measures the difference in the B_0 field at both sides of the boundary of two neighboring regions, is directly proportional to the magnetic susceptibility difference between the two regions and has been used as a measure of tissue magnetic susceptibility in previous works[20,117]. A reference for boundary B_0 measurements, i.e., a region with approximately constant magnetic susceptibility, was thus used in both phantom and animal studies as described below. In humans, placental R_2^* measurements were obtained, as described in detail below.

Phantoms

In each of the phantom datasets, co-localized R_2^* measurements from the 2D and 3D CSE-MRI acquisitions were obtained by placing regions-of-interest (ROIs) over each of the eight vials. Water in the plastic container was used as a reference for boundary B_0 measurements. ROIs were drawn in one slice of each vial and the adjacent water, the boundary of which was parallel to the main magnetic field. Measured B_0 field values were subtracted to obtain the boundary B_0 field difference $\Delta B_0 = B0_{Vial} - B0_{WaterBath}$. All ROIs were drawn in regions of a homogeneous field to reduce apparent B_0 inhomogeneity related bias on measurements.

Animals

In each of the animal datasets, R_2^* measurements were obtained by drawing six ROIs in the anterior placental disc and six in the posterior placental disc, co-localized in the reconstructed R_2^* and B_0 maps from both 2D and 3D CSE-MRI acquisitions. Three slices with relatively large continuous area of placental tissues in the superior, middle and inferior regions of each placental disc were chosen. Two ~0.6 cm^2 oval ROIs were drawn in two separate areas with relatively large continuous area of placental tissues in each slice. Image quality was assessed independently by three radiologists with 19, 21 and 18 years of experience in radiology (Reader-1, Reader-2, Reader-3, respectively) to either accept R_2^* map with no significant artifacts and further confirm ROI locations in the placenta, or reject R_2^* map with severe artifacts. The datasets with both 3D and 2D images accepted by at least two radiologists were used for comparison on R_2^* and B_0 measurements. R_2^* measurements in 2D versus 3D CSE-MRI were compared in anterior placental disc, posterior placental disc, and in both placental discs together. Amniotic fluid in the uterus was used as a reference for boundary B_0 measurements. B_0 field values in a ~0.1 cm^2 oval ROI drawn in the placenta and adjacent amniotic fluid, the boundary of which was approximately parallel to the main magnetic field, were measured and subtracted to obtain $\Delta B_0 = B0_{Placenta} - B0_{AmnioticFluid}$. ΔB_0 measurements in 2D versus 3D CSE-MRI were compared in all animals.

Humans

In the motion assessment study, de-identified R_2^* maps were evaluated independently by the three radiologists. Readers were blinded to image acquisition techniques (2D versus 3D) and the reading order of R_2^* maps in all subjects was randomized. A motion-related artifact score using the following scale was used: 0, non-diagnostic; 1, severe artifacts, but evaluation of some relevant anatomy is possible; 2, modest artifacts, with only mild impairment of evaluation of relevant anatomy; 3, no significant artifacts. Placental R_2^* measurements were obtained by drawing three

~2.4 cm^2 oval ROIs in the superior, middle and inferior regions of the placenta, separately, using T_2-weighted SSFSE as anatomic references. ROIs were co-localized in 2D and 3D CSE-MRI and adjusted if required. The radiologist confirmed all ROI locations in the placenta.

In the repeatability study, placental R_2^* measurements were obtained by drawing three ~2.4 cm^2 oval ROIs in the superior, middle and inferior regions of the placenta, separately, using T_2-weighted SSFSE as anatomic reference. ROIs were co-localized in all imaging series. The radiologist confirmed all ROI locations in the placenta. The within-technique mean difference (MD_{within}), within-technique standard deviation (SD_{within}), and coefficient of repeatability (CR) were calculated between the two repeated scans.

5.2.4 Data Analysis

Phantoms

Linear regression analysis (Pearson's correlation r^2 and Lin's concordance correlation coefficient ρ) and Bland-Altman analysis were used to assess the correlation and bias of both R_2^* and ΔB_0 estimated in 2D CSE-MRI compared to the measurements in 3D CSE-MRI.

Animals

Linear regression analysis (Pearson's correlation r^2 and Lin's concordance correlation coefficient ρ) and Bland-Altman analysis were used to assess the correlation of R_2^*, $\log(R_2^*)$ and ΔB_0 estimated in 2D versus 3D CSE-MRI. Moreover, a linear mixed-effects model was used to analyze the inter-animal variability of placental R_2^* and ΔB_0 measurements. R_2^* measurements in 2D were modeled as a linear function of R_2^* measurements in 3D and the model included random effects on the slope and intercept for animal and random effects on the slope and intercept for ROI

locations (i.e., in anterior or posterior placental disc). ΔB_0 measurements in 2D were modeled as a linear function of ΔB_0 measurements in 3D and the model included random effects on the slope and intercept for animal. Statistical significance was defined as $P \leq 0.05$.

Humans

In the motion assessment study, the readers' score in 2D CSE-MRI and 3D CSE-MRI were compared by using Student's t-test. Mean placental R_2^* of the three ROIs measured in 2D and 3D CSE-MRI were compared by using Student's t-test.

All statistical analysis was performed using Matlab (MathWorks, Natick, MA).

5.3 Results

5.3.1 Phantoms

Figure 23 shows the T_1-weighted structural reference image (a), R_2^* map (b) and B_0 field map (c) of a single slice in 3D CSE-MRI high SNR acquisition of four vials in one batch of the phantom. Boundary B_0 measurements ΔB_0 of one vial and the adjacent water are illustrated in yellow dashed oval ROIs in the zoomed-in B_0 field map (d). The measurements of the other seven vials were performed analogously. **Figure 23e** and **Figure 23**f show R_2^* and ΔB_0 of all eight vials with varying ferumoxytol concentrations measured in the four CSE-MRI acquisitions. Both R_2^* and ΔB_0 increase approximately linearly with increased ferumoxytol concentrations in 2D CSE-MRI high SNR and 3D CSE-MRI high SNR, throughout the entire range of ferumoxytol concentrations. In 2D CSE-MRI and 3D CSE-MRI, R_2^* and ΔB_0 also increase at moderate ferumoxytol concentrations (i.e., <176 μg/mL). Relative to the reference measurements from 3D

CSE-MRI high SNR, bias in both R_2^* and ΔB_0 measurements was observed in 3D CSE-MRI at high ferumoxytol concentrations (i.e., ≥ 220 μg/mL). Similarly, bias in R_2^* and ΔB_0 measurements was observed in 2D CSE-MRI at high ferumoxytol concentrations (i.e., ≥ 176 μg/mL).

Figure 24 shows the linear regression (a1-f1) and Bland-Altman analysis (a2-f2) of R_2^* and ΔB_0 measured in 2D CSE-MRI (a, d), 2D CSE-MRI high SNR (b, e) and 3D CSE-MRI (c, f) in comparison with the reference measured in 3D CSE-MRI high SNR in the phantom. R_2^* and ΔB_0 measurements in all three protocols at low R_2^* and ΔB_0 values are highly correlated with the reference, indicated by the distribution of measurements close to y=x in linear regression analysis (dashed line in a1-f1), and show low bias as indicated by the Bland-Altman analysis (a2-f2). In 2D CSE-MRI, particularly for reference R_2^* values below 390.0 s^{-1} (bold markers, fonts, and lines in a1, a2, d1, d2), a slope of 0.94 (r^2=0.99, ρ=0.99) in linear regression and a bias of -4.8 s^{-1} with limits of agreement of (-41.4, 31.8) s^{-1} are observed in R_2^* measurements, and a slope of 1.07 (r^2=1.00, ρ=0.99) and a bias of 11.4 Hz with limits of agreement of (-12.0, 34.8) Hz are observed in ΔB_0 measurements. However, both R_2^* and ΔB_0 are underestimated at high R_2^* and ΔB_0 values, i.e.: R_2^*>400.0 s^{-1} and a ΔB_0>300.0 Hz in 2D CSE-MRI (a, d) and a reference R_2^*>500.0 s^{-1} and a ΔB_0>400.0 Hz in 3D CSE-MRI (c, f). Bias in both R_2^* and ΔB_0 measurements is reduced at high R_2^* and ΔB_0 values by increasing SNR, i.e., in 2D CSE-MRI high SNR (b, e).

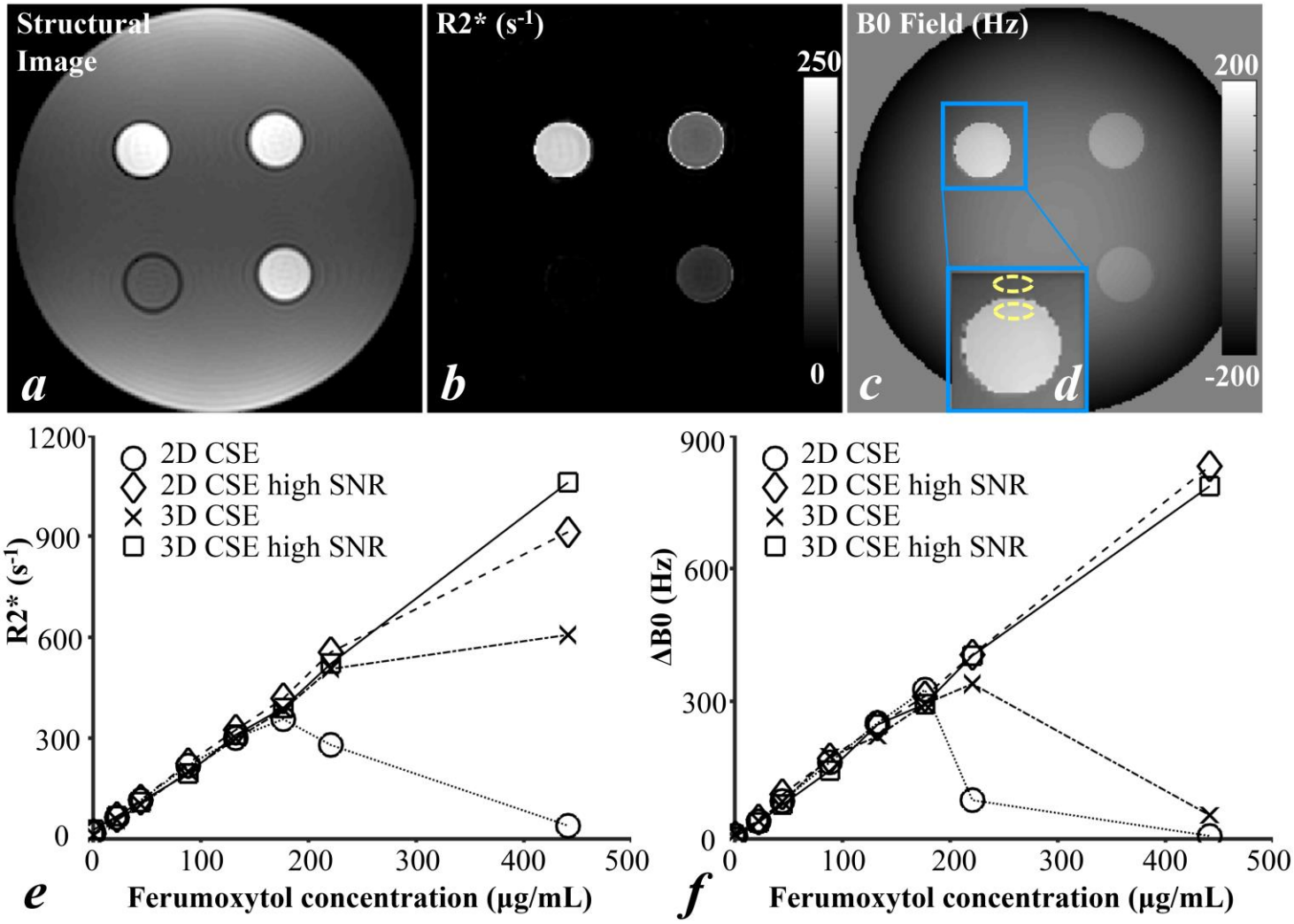

Figure 23. Phantom R_2^* and B_0 field measurements. T_1-weighted Structural reference image (a), R_2^* map (b) and B_0 field map (c) of a single slice in 3D CSE-MRI acquisition of four vials in one batch of the phantom scans, R_2^* (e) and ΔB_0 (f) of all eight vials with varying ferumoxytol concentrations measured in the four CSE-MRI acquisition. An example of boundary B_0 field measurement is indicated by two yellow dashed oval ROIs in the zoomed B_0 field map (d)

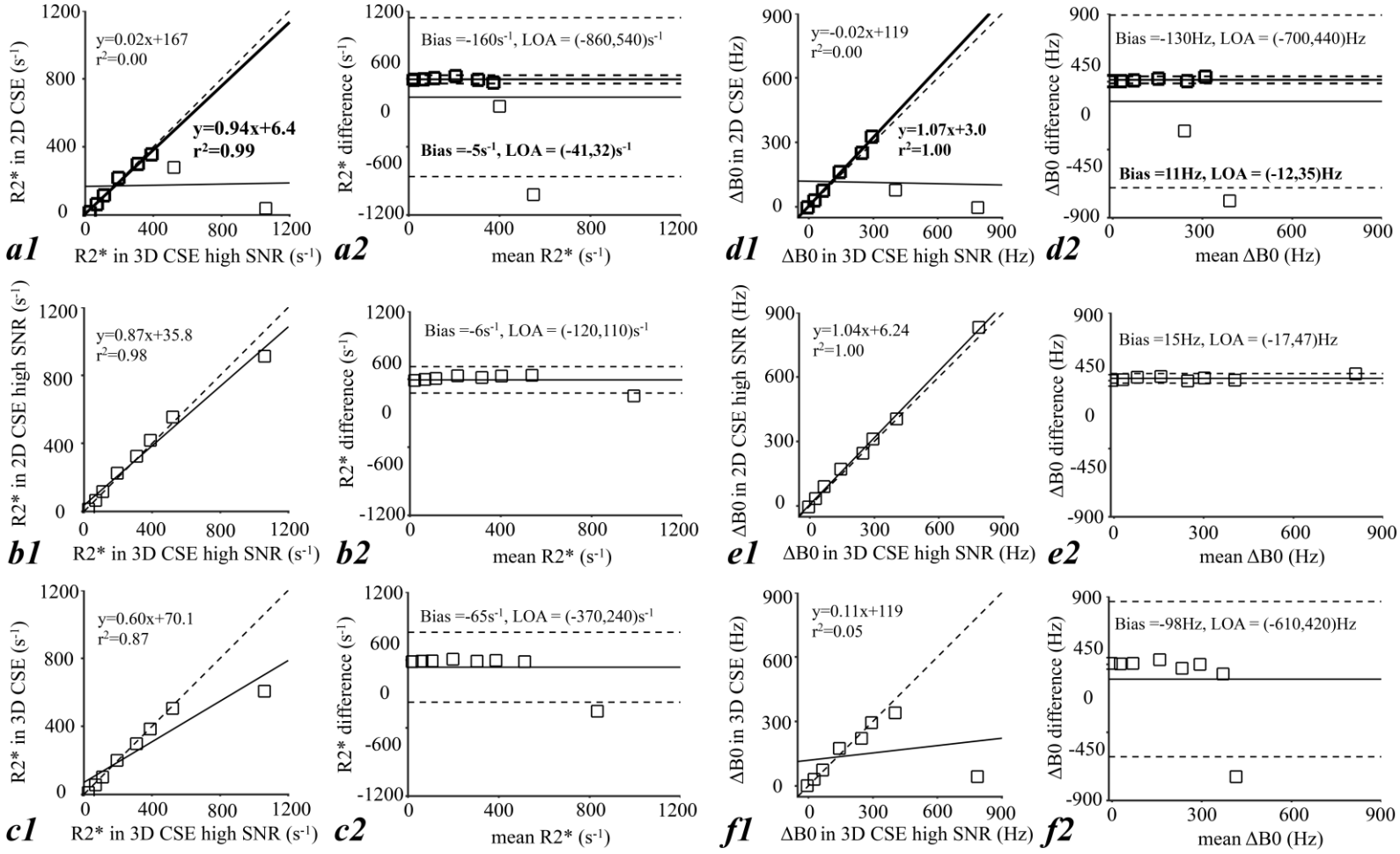

Figure 24. Linear regression and Bland-Altman analysis on phantom measurements. Results from phantom scans: linear regression analysis (a1, f1) and Bland-Altman analysis (a2-f2) of R_2^* and ΔB_0 measured in 2D CSE-MRI (a, d), 2D CSE-MRI high SNR (b, e), and 3D CSE-MRI (c, f) in comparison with the reference measured in 3D CSE-MRI high SNR. Small bias on both R_2^* and ΔB_0 measurements at relatively low R_2^* and ΔB_0 values indicates good correlation of measurements in the three CSE-MRI acquisitions and the reference CSE-MRI acquisition, while the large bias at high R_2^* and ΔB_0 values indicated limited measurable range of each CSE-MRI acquisition. Particularly in 2D CSE-MRI, high linear correlation and small bias on both R_2^* and ΔB_0 were observed for reference R_2^* values below 390.0 s^{-1} (bold markers, fonts, and lines in a1, a2, d1, d2).

5.3.2 Animals

One 3D CSE-MRI of an animal (Rhesus #1) at a scan time point was considered as having severe artifacts and rejected for R_2^* and B_0 measurements by two readers (Reader-1 and Reader-3). Two additional 3D CSE-MRI acquisitions were considered as having artifacts by one reader for each acquisition (Reader 1 and Reader 2, respectively), but were accepted by the remaining two readers (Readers 2 and 3, and Readers 1 and 3, respectively). Therefore, these MRI acquisitions were included in the analysis. All remaining 3D CSE-MRI acquisitions, as well as all 2D CSE-MRI acquisitions in animals were confirmed as without significant artifacts by all three readers. **Figure 25** shows the anatomic water images, R_2^* maps and B_0 field maps in a pregnant rhesus macaque (Rhesus #4) acquired using 2D CSE-MRI and 3D CSE-MRI, both before (upper two rows) and immediately after ferumoxytol administration (bottom two rows). The uterine cavity and two separate placental discs are delineated by orange lines and blue lines, respectively, and the amniotic fluid is indicated by the green arrow in the anatomic images. Amniotic fluid was found to be a reliable reference tissue for boundary B_0 measurements as no ferumoxytol uptake is observed, indicated by stable R_2^* measurements throughout multiple days. R_2^* and B_0 field of both placental discs are elevated after ferumoxytol administration.

Example ROIs for R_2^* measurements and B_0 measurements are shown in **Figure 26**. The linear regression analysis and Bland-Altman analysis of R_2^* and ΔB_0 measured in 2D CSE-MRI and 3D CSE-MRI are shown in **Figure 27**. R_2^* measurements from all animals at all scan time points are consistent in 2D and 3D CSE-MRI with a slope of 0.92 (r^2=0.97, ρ=0.98) in the linear regression on R_2^* (4a) and a slope of 0.90 (r^2=0.95, ρ=0.97) in the linear regression on $\log(R_2^*)$ (4c). The slope of the linear fit of ΔB_0 between 2D and 3D CSE-MRI (4e) is close to 1 (1.05 with

r^2=0.95, ρ=0.97). All correlations were statistically significant with P<0.001. The bias observed in R_2^* and ΔB_0 is small in all animals, while variations are relatively large at high R_2^* and ΔB_0 values, indicated by the relatively broad limits of agreement (4b, 4d, 4f).

The mixed-effects model analysis shows that the variability of both R_2^* (**Table 14**) and ΔB_0 (**Table 15**) measured in 2D versus 3D CSE-MRI across animals, shown as the standard deviation, is large. This analysis indicates relatively large impact of measurements from individual animals, more specifically Rhesus #1, Rhesus #4 and Rhesus #11 on R_2^* measurements and Rhesus #5 and Rhesus #11 on ΔB_0 measurements. The variability of R_2^* measured across placental discs (anterior and posterior placental) is small.

5.3.3 Humans

Preliminary Motion Assessment

Figure 28 shows the anatomic image, R_2^* map and B_0 field map from 2D CSE-MRI and 3D CSE-MRI, respectively, acquired in two adult pregnant women (Subject #1, 20 weeks and 5 days of gestation; Subject #10, 21 weeks and 1 days of gestation). In Subject #1 (upper rows), motion artifacts are observed in both R_2^* and B_0 field maps in 3D CSE-MRI (score of 1, 1 and 2 by Reader-1, Reader-2 and Reader-3, respectively), while there are no obvious artifacts in the co-localized slice from 2D CSE-MRI (score of 3 by all three readers). In Subject #10 (lower rows), there are no obvious motion artifacts in R_2^* maps and B_0 field maps from both 3D CSE-MRI (score of 2, 2 and 3 by Reader-1, Reader-2 and Reader-3, respectively) and 2D CSE-MRI (score of 2, 3 and 3 by Reader-1, Reader 2 and Reader-3, respectively)

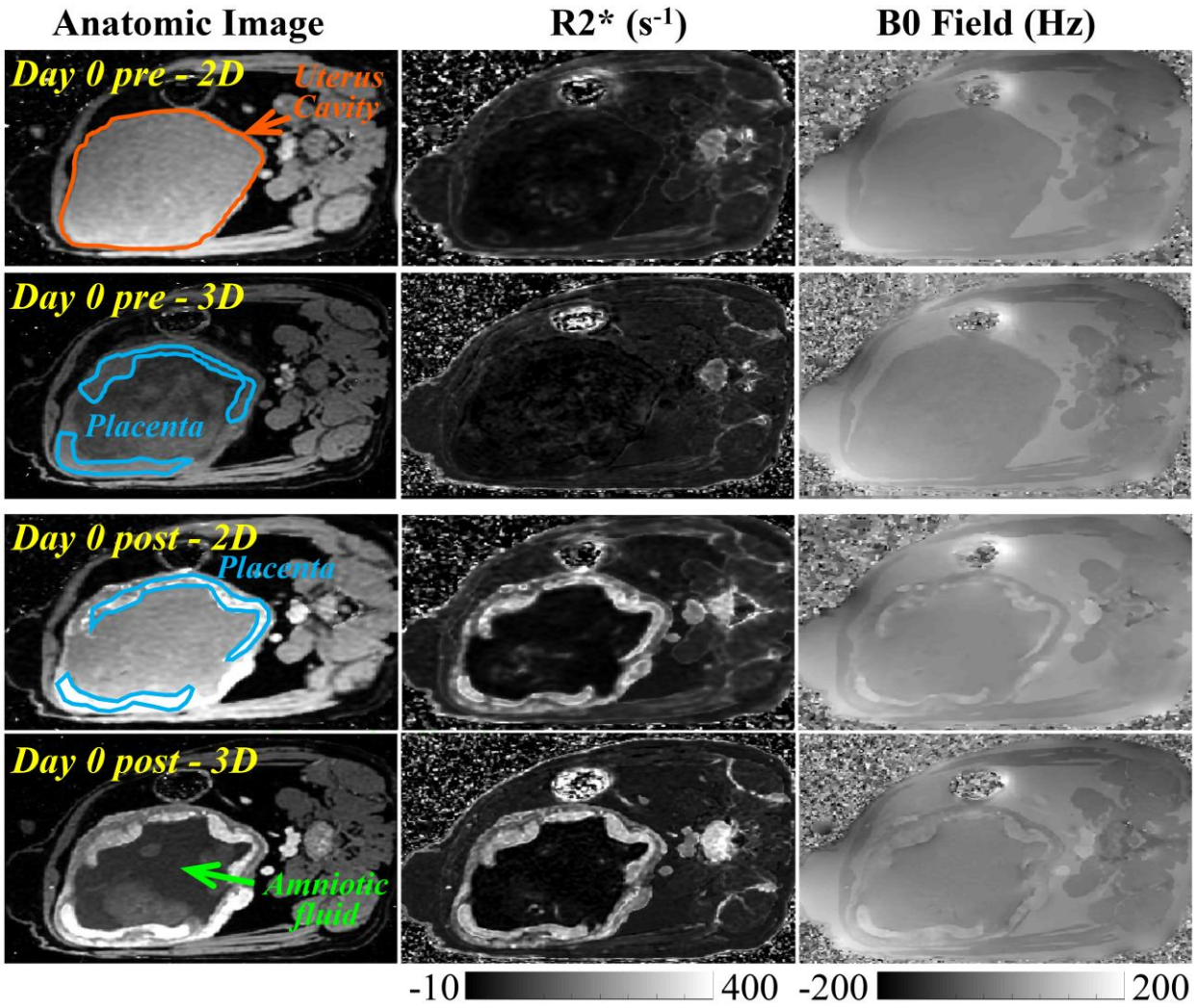

Figure 25. Representative images from 2D and 3D CSE-MRI in animals. Representative anatomic images, R_2^* maps, and B_0 field maps from 2D and 3D CSE-MRI acquisitions in a pregnant rhesus macaque (Rhesus #4) at scans before (Pre) and immediately after (Post) ferumoxytol administration. Two placental discs and the uterus cavity are delineated by blue lines and orange lines, respectively. The amniotic fluid is indicated with a green arrow on the anatomic image.

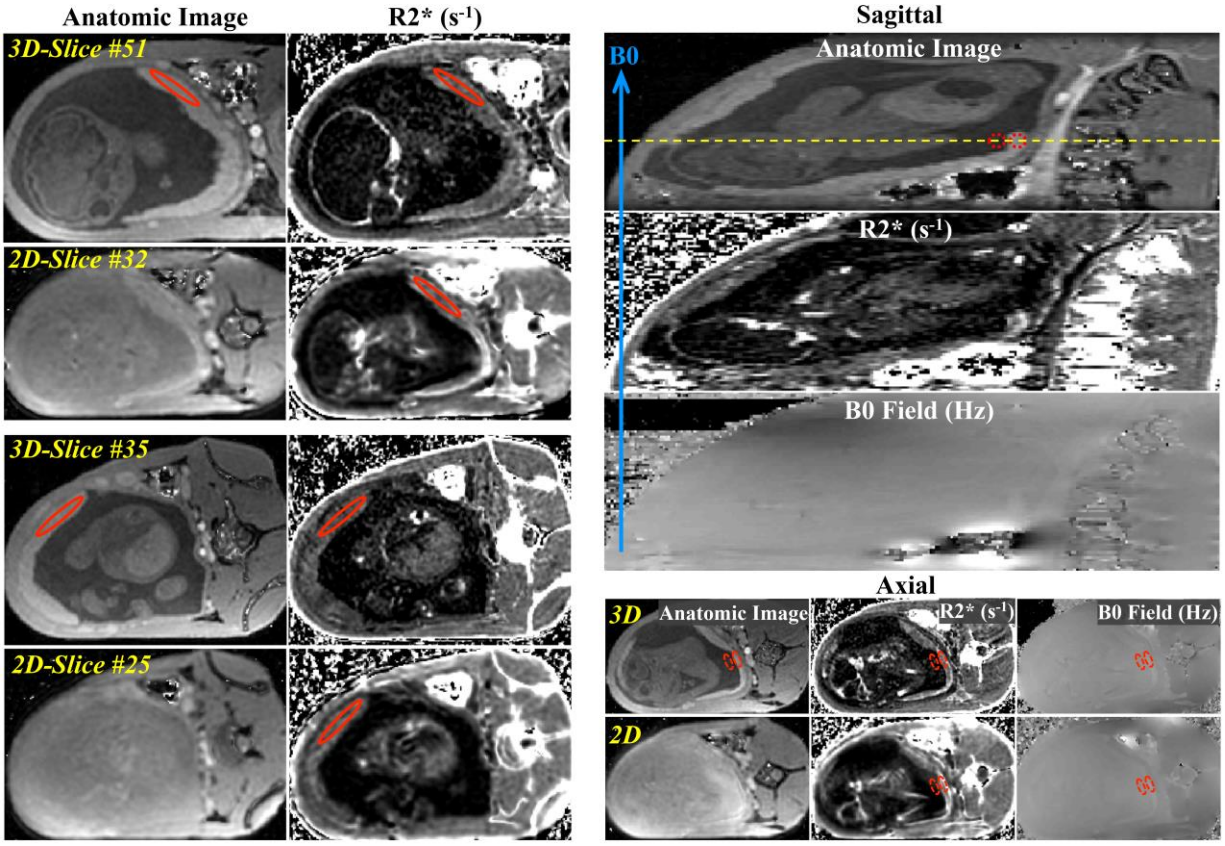

Figure 26. Example ROIs for R_2^* and B_0 field measurements. Example ROIs for R_2^* measurements, delineated by red solid lines in each of the two separate placental discs (Left) and example ROIs for B_0 measurements, delineated by red dashed lines in the placental disc and adjacent amniotic fluid (Right), in 3D and 2D CSE-MRI of Rhesus #1 at the scan one day after ferumoxytol administration. ROIs for R_2^* measurements were first drawn in the anatomic image of the respiratory-gated 3D CSE-MRI. Slices with similar anatomic structures as in 3D images were located in free-breathing 2D CSE-MRI. ROIs were then drawn in co-localized positions in the R_2^* maps of 2D CSE-MRI. For B_0 measurements, a boundary of the placenta and adjacent amniotic fluid, which was approximately parallel to the main magnetic field, was located using reformatted sagittal images (Upper right). ROIs were then drawn in the axial anatomic image of the respiratory-gated 3D CSE-MRI (Bottom right). Slices with similar anatomic structures as in 3D images were located in free-breathing 2D CSE-MRI. ROIs were then drawn in co-localized positions in the B_0 maps of 2D CSE-MRI, using the contrast of the R_2^* map for assistance.

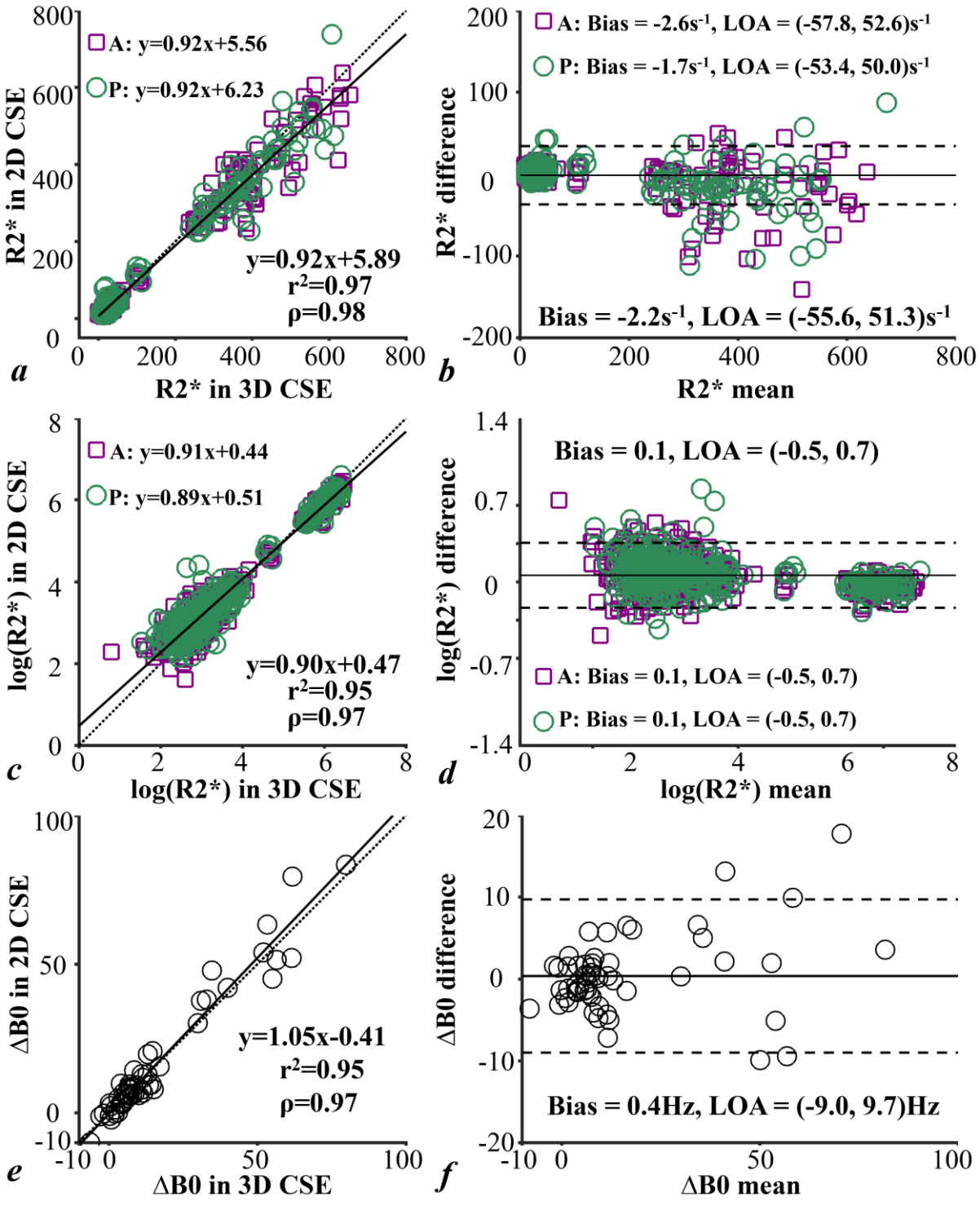

Figure 27. Linear regression and Bland-Altman analysis on animal data. Linear regression analysis (a, c, e) and Bland-Altman analysis (b, d, f) of R_2^*, $\log(R_2^*)$ and ΔB_0 measured in 2D CSE-MRI in comparison with the measurements in 3D CSE-MRI of anterior placental disc, posterior placental disc and both together in animals. R_2^* and ΔB_0 measurements are consistent in 2D and 3D CSE-MRI acquisitions.

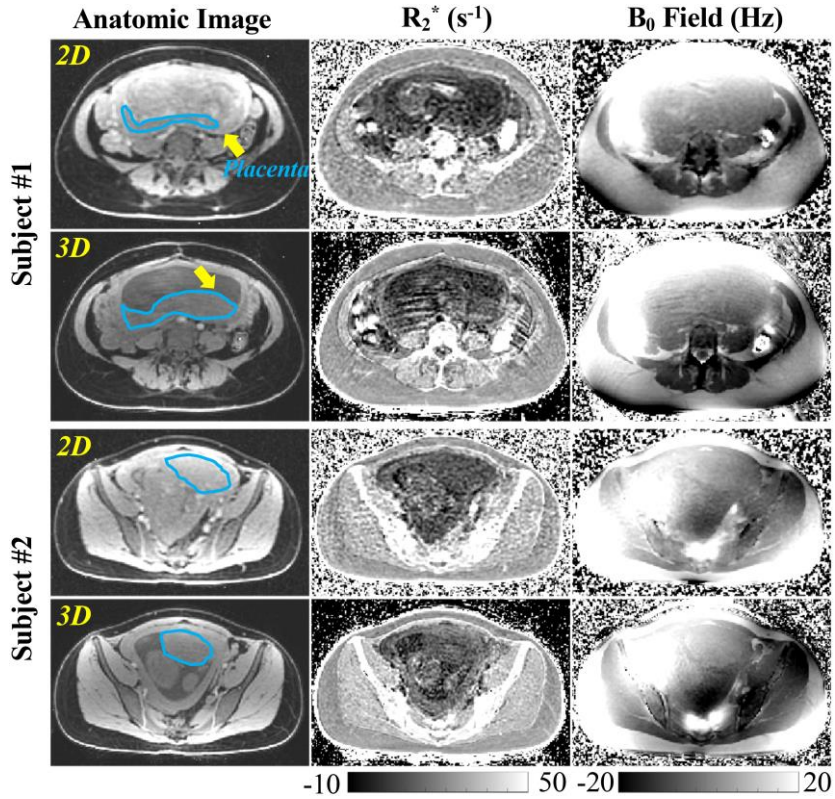

Figure 28. Example 2D and 3D CSE-MRI in pregnant women. Anatomic images, R_2^* maps, and B_0 field maps of 2D and 3D CSE-MRI in two pregnant women. Motion artifacts are observed in the R_2^* map and B_0 field map in 3D CSE-MRI of Subject #1, while no obvious artifacts are observed by the radiologist in 2D CSE-MRI. The placental disc of this subject (delineated by blue lines) was located in a different location of the maternal pelvic for 2D vs 3D CSE-MRI (see yellow arrows), suggesting the presence of fetal motion during this exam. No obvious artifacts or obvious movement of the placenta are observed by the radiologist in 3D or 2D CSE-MRI in Subject #10.

Table 14. Linear mixed-effects model analysis of R_2^* measurements in animals.

Fixed Effects	**Estimated Change in R_2^* (s^{-1})**	***P* value**
Imaging Protocols		
R_2^* from CSE 3D	reference	
R_2^* from CSE 2D	Intercept: 5.70 (3.35, 8.05); Slope: 0.92 (0.88, 0.97)	<.001; <.001
Random Effects	**Standard Deviation of R_2^* (s^{-1})**	
Individual Animal	Intercept: 2.57 (2.01, 3.29); Slope: 0.07 (0.06, 0.10)	
ROI Location	Intercept: <0.0001; Slope: <0.0001	

Note – Data in parentheses are 95% confidence intervals. CSE: chemical shift-encoded

Table 15. Linear mixed-effects model analysis of B_0 field measurements in animals.

Fixed Effects	Estimated Change in ΔB_0 (Hz)	*P* value
Imaging Protocols		
ΔB_0 from CSE 3D	reference	
ΔB_0 from CSE 2D	Intercept: -1.14 (-2.33, 0.05); Slope: 1.09 (0.97, 1.20)	.060; <.001
Random Effects	**Standard Deviation of ΔB_0 (Hz)**	
Individual Animal	Intercept: 0.89 (0.25, 3.17); Slope: 0.17 (0.10, 0.28)	

Note – Data in parentheses are 95% confidence intervals. CSE: chemical shift-encoded

Table 16. Repeatability analysis for placental R_2^* in human subjects at 1.5T.

		MD_{within} (s^{-1})	SD_{within} (s^{-1})	CR (s^{-1})
2D CSE-MRI	All (N=21)	0.7	3.4	9.5
	Superior (N=7)	1.0	2.7	7.6
	Middle (N=7)	1.6	3.4	9.4
	Inferior (N=7)	-0.7	4.1	11.3
3D CSE-MRI	All (N=21)	-0.2	3.8	10.6
	Superior (N=7)	0.5	5.1	14.1
	Middle (N=7)	-0.4	2.4	6.6
	Inferior (N=7)	-0.6	4.1	11.3

Note – CSE: chemical shift-encoded. MD_{within}=within-technique mean difference. SD_{within}=within-technique standard deviation. CR=coefficient of repeatability

A score of 2.9±0.3, 3.0±0 and 3.0±0 for motion assessment in 2D CSE-MRI is significantly higher than a score of 1.8±0.6, 1.3±0.7, 1.9±0.6 in 3D CSE-MRI in Reader-1 (P=0.001), Reader-2 (P<0.001) and Reader-3 (P<0.001). Mean placental R_2^* of all ten subjects is 10.2 s^{-1} with a range of 6.7 s^{-1} to 15.9 s^{-1} measured in 2D CSE-MRI. It is not significantly (P=0.174) different from the mean placental R_2^* of 11.3 s^{-1} with a range of 8.3 s^{-1} to 13.2 s^{-1} measured in 3D CSE-MRI.

Preliminary Repeatability Study

In the ROIs of the seven human subjects, a MDwithin of 0.7 s^{-1}, SDwithin of 3.4 s^{-1}, and CR of 9.5 s^{-1} were observed in the repeated 2D CSE-MRI, as shown in **Table 16**. A MDwithin of -0.2 s^{-1}, SDwithin of 3.8 s^{-1}, and CR of 10.6 s^{-1} were observed in the repeated 3D CSE-MRI.

5.4 Discussion

In this study, we have evaluated the accuracy of R_2^* and B_0 field measurements obtained from 2D CSE-MRI acquisitions without respiratory gating by comparing the correlation and bias to the reference 3D CSE-MRI acquisition in phantoms and pregnant rhesus macaques. High correlation and low bias of both R_2^* and boundary B_0 field measurements in 2D CSE-MRI compared to 3D CSE-MRI were observed in a phantom over a wide range of R_2^* values. Additionally, high correlation and low bias were also observed in ferumoxytol-enhanced MRI of the pregnant rhesus macaques, demonstrating the accuracy of 2D CSE-MRI in the presence of maternal respiratory motion. Further, we preliminarily evaluated motion artifacts and repeatability of 2D CSE-MRI for placental R_2^* mapping in pregnant women without ferumoxytol administration. The high score for motion assessment in 2D CSE-MRI showed no significant

artifacts, demonstrating its motion-robustness due to the short temporal footprint for each acquired slice. Preliminary assessment indicated repeatable R_2^* mapping in pregnant subjects.

The study with animals under general anesthesia enables reliable imaging with 3D CSE-MRI in the absence of fetal motion, which provides reference R_2^* and B_0 measurements. This experiment design provides a unique opportunity to perform in vivo evaluation of the accuracy of 2D CSE-MRI by comparing to the reference 3D CSE-MRI, as this reference will likely not be reliable in the presence of fetal motion.

Joint analysis of the MRI measurements for iron concentration and cell and tissue localization experiments on the animal model in this study of inflammation at the maternal-fetal interface are under separate investigation. This joint analysis will assess the feasibility of ferumoxytol-enhanced placental MRI in an inflammation model, which may potentially enable assessment of macrophage activation and localization at the maternal-fetal interface. Upon assessment of safety and regulatory approval, ferumoxytol-enhanced CSE-MRI may be applied in pregnant women to validate its potential as a non-invasive approach for identifying immune cell homing, which may enable early assessment of the developing preeclampsia.

Sixteen echo times up to 18 ms in 2D CSE-MRI in this inflammation study were optimized to capture potentially modest changes in R_2^* values. TR was thus relatively long, leading to ~3 seconds scan time for each slice. The temporal footprint for each slice can be further shortened by reducing the number of echo times, leading to a reduced TR. In 3D CSE-MRI, however, fewer echoes (i.e., eight echo times) were acquired in order to reduce the scan time, which was already lengthy due to the need for respiratory gating.

CSE-MRI acquisitions were performed at different field strengths for animals (at 3.0T) and humans (at 1.5T) in this work. The high SNR at 3.0T benefits the MRI quantification in animal

studies, which also required higher spatial resolution. When the human study started, a wide-bore 1.5T scanner in our institute was preferred based on subject comfort and research availability considerations. In addition, this was our first research MRI study in pregnant humans at our institute. Therefore 1.5T was chosen for the human studies, in consideration of potential issues like specific absorption rate (SAR) for some MRI techniques applied in this human placenta study.

The SNR in 2D sequential SGRE acquisition is generally lower than SNR in 3D SGRE[111]. The range of R_2^* and B_0 field that can be measured without bias is affected by SNR, as shown in the phantom study. Thus, high SNR may need to be achieved to provide accurate R_2^* and B_0 field estimations at high ferumoxytol concentrations especially in macrophages of the reticuloendothelial system (e.g., liver, spleen, bone marrow) where iron deposition can remain high after ferumoxytol injection[103]. In macrophages outside the reticuloendothelial system in inflammation response, however, moderate iron concentrations have been observed which can be detectable with current CSE-MRI techniques[19,89,90]. Thus, the dynamic range of the iron concentration at macrophage homing sites of inflammation at the maternal-fetal interface is expected to be moderate, although the exact range is still unknown (and is under current investigation in our ongoing projects). Therefore, the proposed 2D CSE-MRI technique is expected to be effective for potential ferumoxytol-enhanced MRI studies of inflammation at the maternal-fetal interface.

Although the proposed boundary B_0 measurements provide a measurement of magnetic susceptibility, reconstruction of magnetic susceptibility maps may be desirable. Unfortunately, quantitative susceptibility mapping requires a 3D B_0 field map, which is not readily available in 2D CSE-MRI due to potential mis-registration between slices. Nevertheless, the boundary B_0

measurements are feasible in 2D CSE-MRI and thus enable a magnetic susceptibility measure to assess iron concentration as demonstrated in previous works[20,117].

This study has several limitations. First, the evaluation of 2D CSE-MRI in the presence of fetal motion is limited in animals under general anesthesia. Comprehensive repeatability studies in ferumoxytol phantoms with aperiodic motion, animals and human subjects at different gestation states are needed to further evaluate 2D CSE-MRI for R_2^* and B_0 field mapping in placental imaging. In the presence of fetal motion, however, we expect 2D CSE-MRI to provide good image quality within slices acquired during quiescent periods without fetal motion (and possibly also with moderate motion). In addition, motion assessment needs to be performed in a large number of human subjects. Further, R_2^* of the whole placental discs in both animals and human subjects needs to be assessed in future studies to evaluate the spatial distribution of the iron concentration in the placenta and the placental oxygenation.

5.5 Conclusion

In conclusion, this study demonstrated 2D CSE-MRI as a promising technique for accurate evaluation of R_2^* and B_0 field in the placenta without the need for respiratory bellows or navigators. Further evaluation of 2D CSE-MRI for the detection and quantification of ferumoxytol in the setting of motion is warranted. Upon successful validation, the motion-robust technique may provide a reliable approach for R_2^*- and B_0 mapping-based evaluation of placental health in ferumoxytol-enhanced placental MRI, and BOLD-based placental functional imaging[30].

Chapter

6. R_2^*-Mapping Based Placental Oxygenation Imaging with Endogenous BOLD Contrast

6.1 Introduction

The placenta's vascular network is organized into cotyledons which regulate the maternal-fetal exchange of nutrients, oxygen, and waste[118]. Each cotyledon operates as a perfusion 'unit' either whole or partially separated from other cotyledons. Oxygenated blood from the maternal uterine arteries is distributed into the cotyledons through the uteroplacental spiral arteries. Dissolved oxygen percolates and exchanges across the villi within the intervillous space of the placenta thereby entering the fetal circulation. Local placental oxygenation is therefore a product of the maternal blood oxygenation level and vascular oxygen transport and delivery, as well as oxygen consumption by both the growing fetus and placenta.

Placental function depends on adequate uteroplacental and fetoplacental blood flow and oxygen extraction across the placental tissue. Deficiencies in placental function impair placental function and affect fetal growth[119,120]. Maternal obesity is associated with increased risk for hypertension and preeclampsia with resulting vascular malformation and reduced placental blood flow, leading to fetal growth restriction[32]. Therefore, assessment of placental function including

regional perfusion and oxygenation is highly desirable to detect dysfunction prior to clinical manifestation.

Current obstetric clinical standards utilize ultrasounds methods to interrogate the uterine and fetal umbilical arteries by Doppler velocimetry[121]. While capable of measuring uteroplacental blood flow, ultrasound has limited spatial resolution and tissue coverage, and is unable to identify altered oxygen states.

MRI enables high-resolution anatomic and functional imaging with multiple contrast. Quantitative MRI is capable of measuring tissue MRI properties associated with tissue biological changes. Accurate and reproducible quantitative MRI may provide potential imaging biomarkers for longitudinal tracking of placental health at different gestation stages. Placental MRI techniques, including perfusion, relaxometry and diffusing imaging, have been developed in animal model of pregnant rhesus macaques[30,31,122], who have a villous organization of the placenta similar to pregnant women. Moreover, quantitative MRI has also shown promise in assessing placental function in pregnant women[33,34,35,36,123].

Dynamic contrast enhanced (DCE) MRI is a technique previously utilized to measure maternal blood flow in the placenta of nonhuman primates[31,122]. In gadolinium-based DCE-MRI, the location of spiral arteries can be identified as the region with early contrast arrival and regional blood flow in individual cotyledons can be quantified[31]. Gadolinium-based contrast agent, however, has been shown to cross the placenta and expose in fetal tissues[91,92,124], which raises usage concerns in pregnant women. Ferumoxytol, an FDA-approved intravenous iron compound for treatment of anemia, has been shown no significant iron deposition in fetal tissues or tissue histopathology with maternal exposure[108]. Importantly, ferumoxytol is increasingly being used off-label as an alternative vascular MRI contrast agent. Ferumoxytol-based DCE-MRI has

demonstrated the ability to estimate contrast arrival time and relative blood flow to a slice within the placenta in nonhuman primates[122]. Thus, ferumoxytol-based DCE-MRI may be an alternative for evaluating maternal blood flow in the placenta.

R_2^* mapping-based measurement of the blood oxygen level-dependent (BOLD) effects have emerged in assessing placental oxygenation using endogenous MRI contrast in rhesus macaques and human[30,123,125.] The maternal blood delivered to the spiral artery is highly oxygenated and becomes more deoxygenated when oxygen exchange happens along with the local blood perfusion in the intervillous space. It results in spatial R_2^* gradients due to increased local dephasing of MR signal in the presence of paramagnetic deoxygenated hemoglobin. Previous studies on rhesus macaques have demonstrated the feasibility of identification the location of spiral arteries and individual cotyledons and quantification of regional placental oxygenation in R_2^* mapping[30]. In pregnant women, placental R_2^* mapping has shown promise for longitudinally assessing placental health and predicting pregnancy outcomes[33,34,35,36].

Further, DCE-MRI and R_2^*-mapping, taken together, provide comprehensive imaging techniques to assess placental functions, health and pathologies related to pregnancy complications. Placental hypoperfusion and hypoxia detected by MRI have strongly correlated with patterns in tissue histological analysis for different rhesus macaque cohorts including Zika virus infection[126], alcohol exposure[127], and intrauterine growth restriction[128]. It is of great interest to further develop and assess ferumoxytol-based DCE-MRI and R_2^*-mapping in characterizing placental functions globally and regionally in animal models of obstetric conditions.

In summary, developing and assessing R_2^*-mapping based placental oxygenation imaging in both animal and human studies are necessary for studying placental functions using endogenous MRI contrast. The purpose of this work was to investigate the feasibility of quantifying regional

placental oxygenation using R_2^* mapping and evaluate the spatial correspondence of oxygenation with perfusion detected by ferumoxytol DCE-MRI in the rhesus macaque. Further, the second purpose was to assess the longitudinal changes in placental R_2^* in non-obese and obese pregnant women.

6.2 Methods

6.2.1 Animals

All procedures were approved by the local institutional animal care and use committee. Six healthy, pregnant rhesus macaques (maternal weight=9.11±1.16 kg) underwent MRI in the late second trimester (day 99.5±5.3 of gestation) based on an average term pregnancy of 166-day in macaques[129]. Animals were divided into two groups and underwent different procedures: untreated control (N=2), saline control (N=4). Animals in the two groups received no injection, or an intra-amniotic injection of 0.5 mL saline, respectively. The saline infusion was applied as the control experiment for the study of inflammation at maternal-fetal interface[130], but it was not the focus of this study. For all procedures and MRI scans, rhesus macaques were anesthetized by administration of up to 10 mg/kg ketamine, and continuously sedated using oxygen with 1.5% isoflurane supplemented with a portable anesthesia system. Animals were monitored during all procedures, and subsequently until fully recovery from the anesthesia. **Table 17** summarizes the animal information in this study.

6.2.2 Humans

In this IRB-approved study, pregnant women with singleton pregnancies were recruited and scheduled for MRI at 14 and 20 weeks of gestation. Subjects with a body mass index (BMI) above 30 kg/m^2 were considered as obese.

6.2.3 MRI Acquisition

Animals

All imaging was performed one day after the saline or IL-1β intervention on a clinical 3.0T MRI system (Discovery MR750, GE Healthcare, Waukesha, WI) with a 32-channel phased array torso coil (Neocoil, Pewaukee, WI) while the animal was in a left-lateral decubitus position. R_2^* mapping was first obtained, followed by DCE-MRI with ~16 mins interval between the two acquisitions.

R_2^* mapping was acquired using a respiratory-gated 3D multi-echo spoiled gradient-echo (SGRE) acquisition. Imaging parameters include: TR=36.0 ms, 12 TEs, $TE_{init}/\Delta TE$=1.7/2.8 ms, flip angle=15°, acquisition bandwidth=±50 kHz, FOV=16×14×15 cm^3, phase/slice acceleration=1.5/1.0, acquisition/reconstruction resolution=1.1×1.1× 2.0/0.6×0.6×2.0 mm^3, total scan time=6:37 mins.

DCE-MRI data were acquired with a 3D dual-echo T_1-weighted SGRE with differential subsampling with Cartesian ordering (DISCO)[131] sequence throughout intravenous injection of 4 mg/kg ferumoxytol (FerahemeTM, AMAG Pharmaceuticals, Waltham, MA) diluted 5:1 with sterile saline over 20 seconds. Imaging parameter include: TR=4.8 ms, TE_1/TE_2=1.2/2.4 ms, flip angle=12°, acquisition bandwidth=±142.86 kHz, FOV=22×15.4×12.8 cm^3, reconstruction

resolution=0.9×0.9×1.0 mm^3, phase/slice acceleration=2.0/2.0, temporal resolution=5.0 sec, total scan time=200-300 sec.

Humans

MRI scans were performed on a wide-bore 1.5T MRI system (Optima MR 450w, GE Healthcare) using a 48-channel phased-array coil (GEM Suite) with subjects in the supine position. A respiratory-gated 3D multi-echo spoiled gradient-echo acquisition covering the entire uterus cavity was obtained for T_2^* ($=1/R_2^*$) mapping. Imaging parameters include: TR=43.0 ms, 16 TEs, $TE_{init}/\Delta TE$=1.5/2.6 ms, flip angle=9°, acquisition bandwidth=±50 kHz, FOV=42×38×14 cm^3, phase/slice acceleration=2.0/1.5, acquisition/reconstruction resolution=2.2×2.0×3.0/1.6×1.6×3.0 mm^3, total scan time=5:27 mins.

6.2.4 Image Reconstruction and Analysis

Animals

All image post-processing and analysis were performed in Matlab (Mathworks, Natick, MA) unless noted. In 3D SGRE imaging, R_2^* map, water and fat images were obtained by using a chemical shift-encoded reconstruction[97]. In DCE-MRI, water and fat images at each time point were reconstructed using two-point water-fat separation. Image registration was applied to colocalize the placenta in R_2^* map and DCE images to reduce the motion between the two acquisitions. Water images from SGRE were registered to water images from DCE-MRI using non-rigid registration (Advanced Normalization Tools[132]). The transformation matrix calculated in the registration was then applied to R_2^* maps to colocalize with DCE images. Semi-automatic segmentation of the placental volume was performed using ITK-SNAP[133] on DCE images.

Placental functional domains were segmented in R_2^* maps and DCE images, separately. Quantitative analysis on the regional oxygenation and volumetric flow of each functional domain were obtained. The flow chart of image reconstruction and analysis is illustrated in **Figure 29**.

Functional domain segmentation and regional oxygen analysis were obtained in R_2^* maps following the method prescribed by Schabel et al[30]. Local maxima of R_2^* in the placenta volume were detected in the smoothed R_2^* map and the iteration number map was calculated using the local maxima as seed points. The watershed segmentation algorithm was applied in the iteration number map to obtain functional domains. The segmentation process is illustrated in **Figure 30**. In each segmented functional domain, regional oxygenation was analyzed based on the spatial distribution of R_2^*, expressed as the radial displacement from the spiral artery source. The intrinsic R_2^* of the placenta tissue in the absence of deoxyhemoglobin R_{20}^*, the fetal oxyhemoglobin concentration $[Hb_{o,f}]$, and scaled oxygen transport to fetal blood $\frac{v_i PS}{\phi}$ were estimated based on the spatial distribution of R_2^* curve. Other parameters used include: the relaxivity of deoxyhemoglobin in human blood at 3.0T[134] assumed equal to 20.2 $s^{-1}mM^{-1}$, maternal arterial oxygen saturation read from pulse oximetry (see **Table 17**), and the maternal total hemoglobin concentration using the mean value of the three rhesus macaques reported in Schabel et al[30].

To deal with contrast dispersion and non-bolus injection, DCE contrast arrival times were estimated by following the method described by Ludwig et al[122]. A left-search of the signal enhancement curve with arrival time denoted as the time-frame with signal enhancing greater than mean±3SD of the background DCE signal (first six time-frames used as 'background'). DCE contrast-time curves were fit to a sigmoid-shaped logistic function on a voxel-wise basis to derive contrast arrival time maps; defined as the time to 50% maximum signal enhancement. Contrast

arrival time maps were smoothed and segmented into functional domain maps using a watershed algorithm, following the method prescribed by Frias et al[31].

Mean R_2^* of pixels with same contrast arrival time was calculated for different arrival times and the Pearson correlation coefficient (ρ) was used to test the correlation between mean R_2^* and arrival time. In addition, a group analysis was used to compare pixel-by-pixel correlation of R_2^* and contrast arrival time. All pixels in each placenta were divided into three groups based on contrast arrival time: <54 sec (Group 1), 54-104 sec (Group 2), >104 sec (Group 3). R_2^* measurements of pixels in each group were compared by using two-tailed Mann-Whitney U test. R_2^* measurements in each group of all animals were also compared, respectively.

Humans

T_1-weighted anatomic images and T_2^* maps of each dataset were reconstructed by using monoexponential fit of complex echo images. Image quality and diagnostic acceptability were evaluated using a 5-point Likert scale. Scores 1 to 2 were considered as non-diagnostic image quality and excluded from the quantitative analysis. Scores 3 to 5 were considered as diagnostically acceptable. Images were evaluated in OsiriX (Pixmeo SARL, Switzerland) by a radiologist with 9 years of experience in clinical MRI. 3D placental contouring was performed on the T_1-weighted anatomic image using ITK-SNAP[133]. Additionally, a ~3 cm^2 circular ROI was drawn in the gluteal muscles to measure and track the longitudinal muscle T_2^*.

Table 17. Information of animals in the placental BOLD study. Animal information including the gestational age, maternal weight, placental volume, placental surface area and arterial O_2 saturation during the MRI scans. Trimester calculations based on an average 166-day gestational cycle for rhesus macaque.

Animal Index	**Intervention**	**Gestational Age** (Trimester) [days]	**Maternal Weight** [kg]	**Placental Volume** Total (separate discs) [cm^3]	**Placental Surface Area** Total (separate discs) [cm^2]	**Arterial O_2 Saturation** (%)
1	None	106 (2nd)	10.04	61.9 (32.3, 29.6)	22.6 (12.3, 10.3)	99
2		91 (2nd)	9.90	52.7 (38.9, 13.8)	24.6 (17.7, 6.9)	99
3	Saline	100 (2nd)	9.06	34.7 (25.6, 9.1)	15.4 (10.0, 5.4)	98
4		97 (2nd)	8.56	62.2 (45.8, 16.5)	19.5 (12.9, 6.6)	99
5		99 (2nd)	10.02	65.7 (39.3, 26.5)	18.9 (10.8, 8.0)	99
6		104 (2nd)	7.09	45.4 (25.9, 19.5)	20.3 (10.4, 9.9)	99
Average		99.5±5.3	9.11±1.16	53.8±12.0	20.2±3.2	98.8±0.4

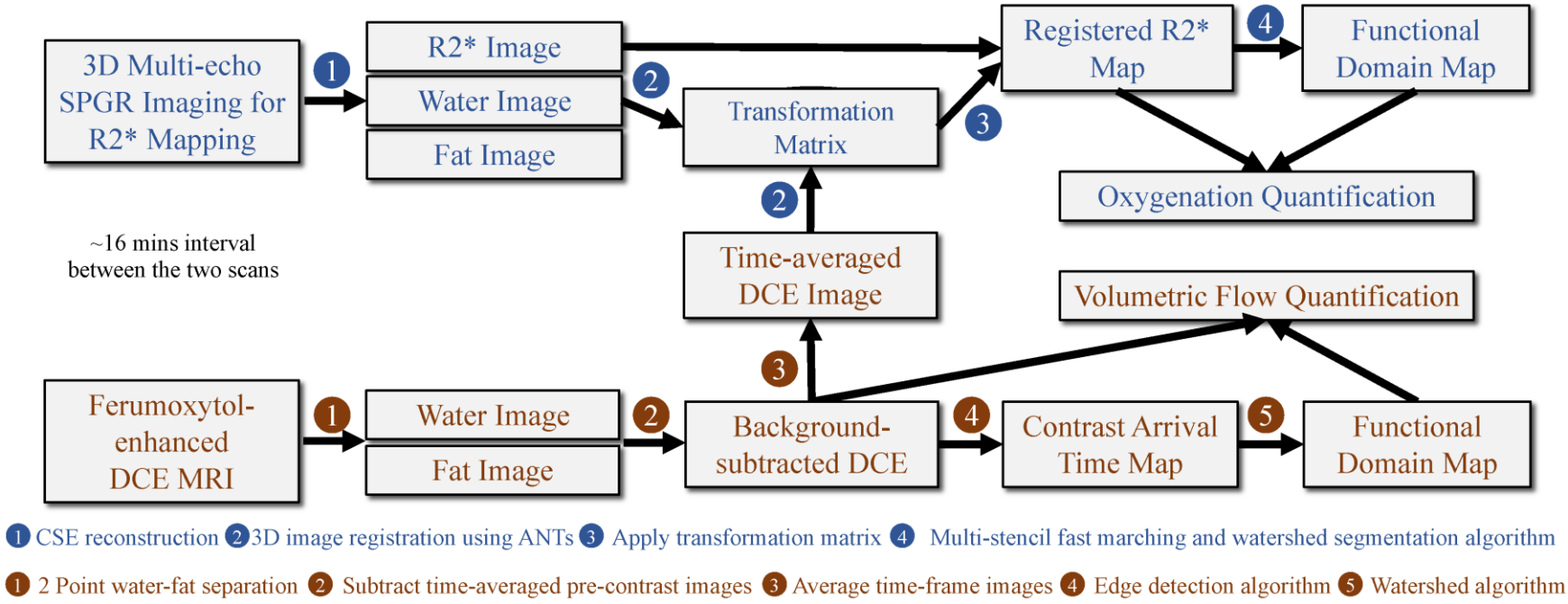

Figure 29. Flow chart of data processing in placental BOLD study. Flow chart of image reconstruction and data processing in R_2^* mapping and ferumoxytol DCE of the placenta in this study, including image registration, functional domain segmentation, and quantification of regional oxygenation and volumetric flow.

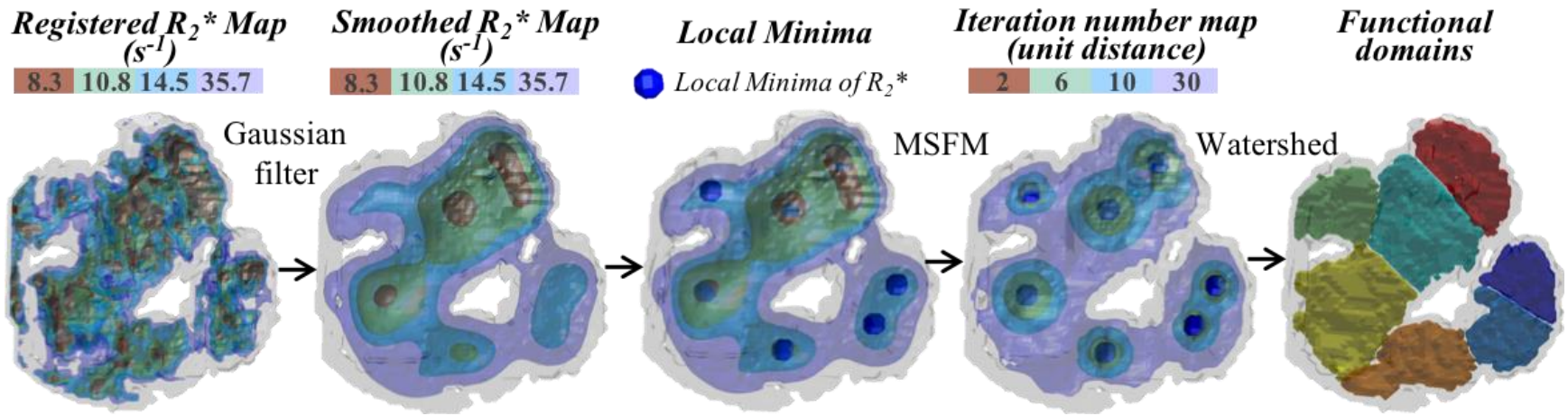

Figure 30. R_2^*-mapping based functional domain segmentations in rhesus macaques.

6.3 Results

Animals

Figure 31 shows the six echo images (**Figure 31**A) of one slice in an animal (#1), the calculated 3D R_2^* maps of the two placental discs (**Figure 31**B), the segmented functional domains using R_2^* maps (**Figure 31**C), and the spatial distribution of R_2^* in functional domains. The signal intensity of the placental tissues decays when echo times increase and it shows heterogenous distribution at long echo times, indicating R_2^* of the placental tissues vary spatially. In the R_2^* map (**Figure 31**B), placental R_2^* varies in the range of 10-80 s^{-1} and the placenta is visually divided by multiple local regions with gradually increasing R_2^* from the center to peripheral areas. In this animal, a total of 16 functional domains is segmented with 8 domains in each disc with volumes ranging from 0.2-4.7 cm^3. The locations of the segmented functional domains (**Figure 31**C) are consistent with the local regions shown in the R_2^* map. In the plots showing the example curves of the spatial distribution of R_2^* (**Figure 31**D), median R_2^* (black dots) increases as the distance to the local minimum of R_2^* increases.

Figure 32 shows the DCE analysis of the same animal (#1) as in **Figure 31**. Localized regions of contrast in-flow occurred in separate functional domains of the placental tissue as observed in serial DCE images in **Figure 32**A. Heterogeneous contrast arrival times are seen throughout the placenta tissue, differing by tens of seconds. Contrast arrival time maps (**Figure 32**B) were derived by fitting DCE data to Fermi function and then used to segment the functional domains within the placenta as shown in **Figure 32**C. A total of 18 functional domains were identified with volumes ranging from 0.3-5.8 cm^3.

Figure 33 show R_2^* maps, contrast arrival time maps, and functional domains segmented from the two imaging acquisitions in the two discs of two animals (#4, #5), respectively. R_2^* and contrast arrival time both showed heterogeneous distribution. Qualitatively, regions of locally minimum R_2^* (purple isosurfaces in **Figure 33**A and **Figure 33**D) appeared spatially correlated with regions of short arrival times (red isosurfaces in **Figure 33**B and **Figure 33**E). A total number of 8 and 16 functional domains were identified in the two animals, respectively, indicating that the number of functional domains varied in different animals at same gestation stage. In both animals, the functional domains segmented in R_2^* map (purple isosurfaces in **Figure 33**C and **Figure 33**F) showed spatial correlation with the functional domains segmented in DCE (red isosurfaces in **Figure 33**C and **Figure 33**F).

The segmented placental volume varies in the range of 35 cm^3 to 66 cm^3 and the placental surface area varies in the range of 15 cm^2 to 25 cm^2, as summarized in **Table 17**. **Table 18** summaries the number of functional domains, domain volumes, and quantitative flow and oxygenation parameters estimated in R_2^* map and DCE-MRI of all six animals in this study. In R_2^* mapping-based analysis, the number of segmented functional domains vary from 8 to 18 in all animals with domain volumes varying from 0.1 cm^3 to 8.0 cm^3. The mean of the estimated median R_{20}*, median $[Hb_{o,f}]$, and median $\frac{v_i PS}{\phi}$ varies from 7.8 s^{-1} to 10.0 s^{-1}, 4.7 mM to 6.3 mM, and 0.2 $\times 10^6$ cm^{-3} to 3.0 $\times 10^6$ cm^{-3}, respectively. In DCE-MRI analysis, the number of segmented functional domains and the domain volume are consistent with the estimates in R_2^* mapping-based analysis.

The pixel-by-pixel correlation of contrast arrival time and intrinsic placental R_2^* in one animal (#5) and all animals is shown in **Figure 34**. Mean R_2^* has a positive correlation with the arrival time in the example animal (ρ=0.72) and all animals (ρ=0.38). Placental R_2^* in tissues with

early ferumoxytol arrival (arrival time < 54 s) is significantly (P<0.05) lower and compared to placental R_2^* in tissues with late ferumoxytol arrival (arrival time > 104 s) in the example animal and all animals.

Humans

A total of 36 pregnant women, 21 non-obese subjects (mean BMI=24.3 kg/m^2) and 15 obese subjects (mean BMI=34.4 kg/m^2), were recruited and imaged at the two time points. 18 MRI datasets were non-diagnostic due to motion artifacts and thus excluded, leaving 12 non-obese and 8 obese subjects with datasets for both time points. 5 non-obese subjects and 1 obese subject had diagnosed complications in pregnancy. **Figure 35** shows the inclusion and exclusion of subjects in the study and subjects' information.

Example anatomical images and T_2^* maps of one obese subject at 14/20 weeks of gestation are shown in **Figure 36**. The segmented placental discs are contoured with blue lines. **Figure 37** shows the histogram of placental T_2^* of one non-obese subject (A), one obese subject (B), and all analyzed non-obese (black)/obese(orange) subjects (C). While the placenta of the non-obese subject has a trend of increased T_2^* with gestation (mode T_2^*: 57.0 ms to 72.9 ms), it has a trend of decreased T_2^* in the obese subject (mode T_2^*: 120.6 ms to 84.1 ms).

The placenta volume, median placental T_2^*, mode placental T_2^* and muscle T_2^* of each subject measured at two time points, and the volume ratio and the change of median/mode placental T_2^* and muscle T_2^* between the two gestational ages are shown in **Figure 38**. The placental T_2^* in the obese subjects is in similar range compared to the non-obese subjects, at both gestational ages (14 weeks: 54~155 ms; 20 weeks: 72~136 ms). In 6 non-obese subjects and 6 obese subjects, placental T_2^* has an increasing trend over gestational age (**Figure 38**F and **Figure**

38G). The muscle T_2^* measurement of all subjects is stable over gestational ages, i.e., 33.9±0.8 ms and 34.0±1.2 ms at 14 and 20 weeks of gestation, respectively.

Substantial increase in placental volume is observed between the two gestational ages, but two subjects with pregnancy complications (diabetes and hypertension, hypertension and preeclampsia) have a much smaller increase (**Figure 38**A and **Figure 38**E). Four subjects with pregnancy complications (preterm fetus, hypertension, hypertension and preeclampsia, preeclampsia) have a relatively low placental T_2^* at 20 weeks of gestation (**Figure 38**B).

6.4 Discussion

In the animal study, we have demonstrated the feasibility of using R_2^* mapping to quantify regional oxygenation in individual cotyledons in the rhesus macaque. The functional domains segmented using R_2^* maps show spatial correlation with those segmented using DCE arrival time maps, which demonstrates substantial correlation with oxygenation and perfusion functional domains. 8-19 functional domains are observed in the studied six rhesus macaques, which are similar to the anticipated number of average domains reported in rhesus macaques[135].

The number of functional domains is observed to vary in different animals at similar gestational age, independent of the placental volume. It was consistently observed in DCE-MRI and R_2^* mapping. Large number of maternal cotyledon may be associated with raised blood pressure in childhood though the association differs between the two sexes[136].

No significant DCE signal enhancement was observed within the amniotic flood, umbilical cord or fetal tissues in all ten monkeys as has been reported[122]. Additionally, previous studies have shown that ferumoxytol is not detectable by MRI in R_2^* mapping of the placenta a week after maternal administration, indicating it is washed out from the placental tissues[137]. The relative short

plasma half-life and delayed phase of ferumoxytol compared to the term pregnancy of 166-day in rhesus macaque may enable using ferumoxytol DCE-MRI for longitudinal studies at different gestation stages. This may include assessing gestational age-dependent placental perfusion changes[138] and the development of pathology-induced hypoperfusion over gestations.

We observed non-rigid motion of the placenta between R_2^* mapping and DCE-MRI. The reconstruction pipeline including the image registration was developed to address this problem. It enables pixel-by-pixel correlation of contrast arrival time and placental R_2^*. The image registration was performed using water anatomic images obtained in DCE-MRI with the dual-echo acquisition and two-point water-fat separation and in the chemical shift-encoded reconstruction in tissue R_2^* estimation. This was in consideration of that the water anatomic images obtained have similar image contrast between the two acquisitions. Furthermore, we observed that applying registration mask on the estimated R_2^* map provides less errors compared to registration signals first and then estimating R_2^*.

In R_2^*-mapping based BOLD measurements, relatively long echo times need to be acquired, leading to a long TR and consequentially a long acquisition time, which brings challenges in placental imaging in the presence of maternal and fetal motion. In this study, a respiratory-gated 3D multi-echo SGRE acquisition was used for R_2^* mapping with animals under general anesthesia. Therefore, the influence of both maternal respiratory motion and fetal motion was diminished. In human scans, free-breathing motion-robust 2D R_2^* mapping[102] and 3D non-Cartesian R_2^* mapping[34] techniques have been proposed and may enable reliable assessment of placental healthy with endogenous contrast.

This study has several limitations. First, the maternal total hemoglobin concentration used in quantifying oxygenation was not recorded and we used the values from a previous study[30]. In

addition, the number of cotyledons from direct observation of the placenta after C-section was not available. Ongoing studies include correlate MRI-detected cotyledons with tissue histology in Zika virus-infected animals and healthy controls.

In the human study, we reported placental T_2^* of non-obese and obese subjects at 14 and 20 weeks of gestation at 1.5T. The range of placental T_2^* is similar between the two subject populations at both gestational ages, respectively. In 6 non-obese subjects, a non-significant trend of increased placental T_2^* between the two gestational ages was observed. Previous studies reported on a negative correlation of placental T_2^* and gestational age (GA)[35,36], while other studies reported no significant correlation of placental T_2^* and gestational age (GA: range 21-38 weeks at 1.5T and 14-23 weeks at 3.0T)[26,139]. This suggests changes in placental oxygenation may be subject-specific at the early gestational window (14-20 weeks). This complicated process can be affected by many factors including the net result of evolving flow, perfusion, placental oxygen extraction efficiency and relative volume of intervillous blood volume and fetal villous tissue. In addition, stable muscle T_2^* measurements at the two scan times indicate that T_2^* measurements are reproducible across scan days. The reproducibility of placental T_2^* measurements, which may be affected by potential motion artifacts, needs further study. Moreover, small placental volume increases between 14 and 20 weeks of gestations and relatively low placental T_2^* values were observed in subjects with pregnancy complications. Joint analysis of the placental oxygenation and clinical indicators will be performed in future work.

6.5 Conclusion

In conclusion, T_2^* mapping provides promising approaches for evaluating regional oxygenation in the placenta of the rhesus macaque and pregnant women. Motion-robust T_2^*

mapping may provide an alternative safe technique using to endogenous MRI contrast to assess placental oxygenation and predict pregnancy outcome.

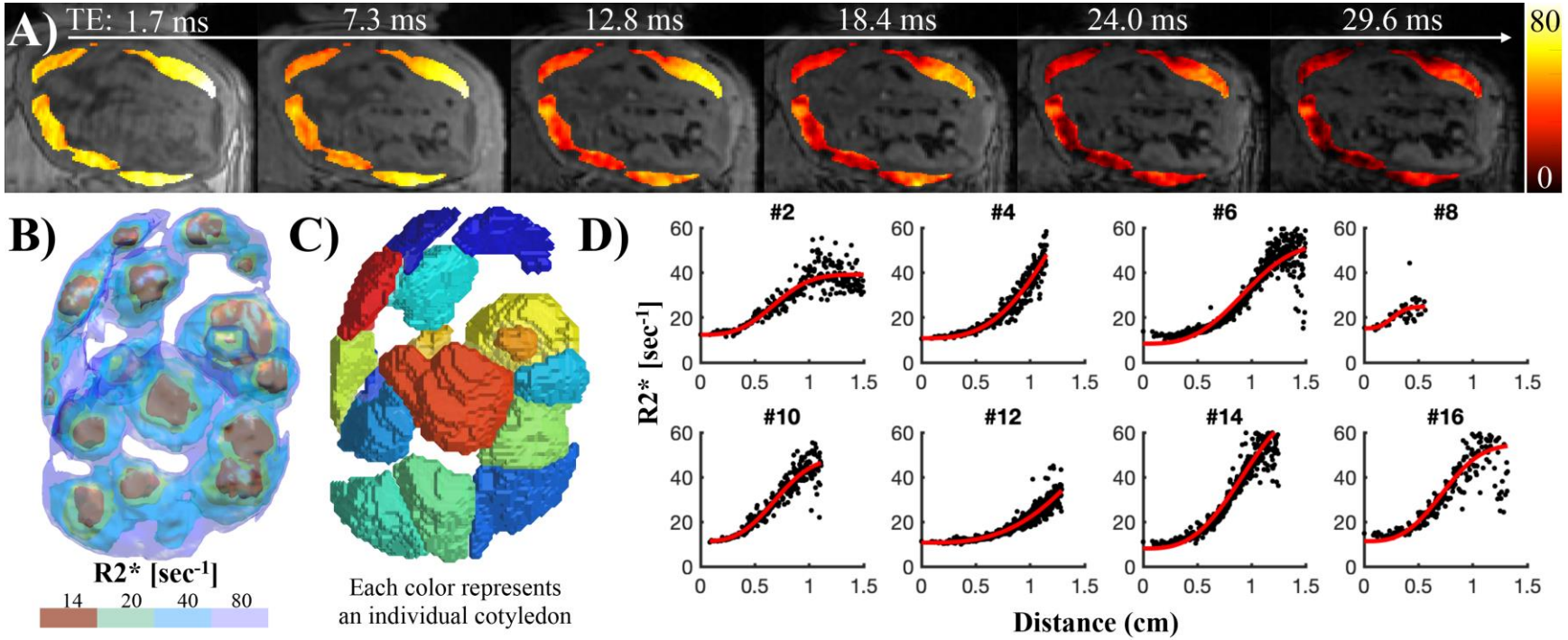

Figure 31. R_2^*-mapping based BOLD analysis in an animal. The multi-echo images of one slice (A), the estimated R_2^* map (B) and the segmented functional domains (C) of the 3D placental volume, and the spatial distribution of R_2^* in eight example domains in one animal (#1). A total of 16 domains were segmented with 8 in each placental disc in the animal.

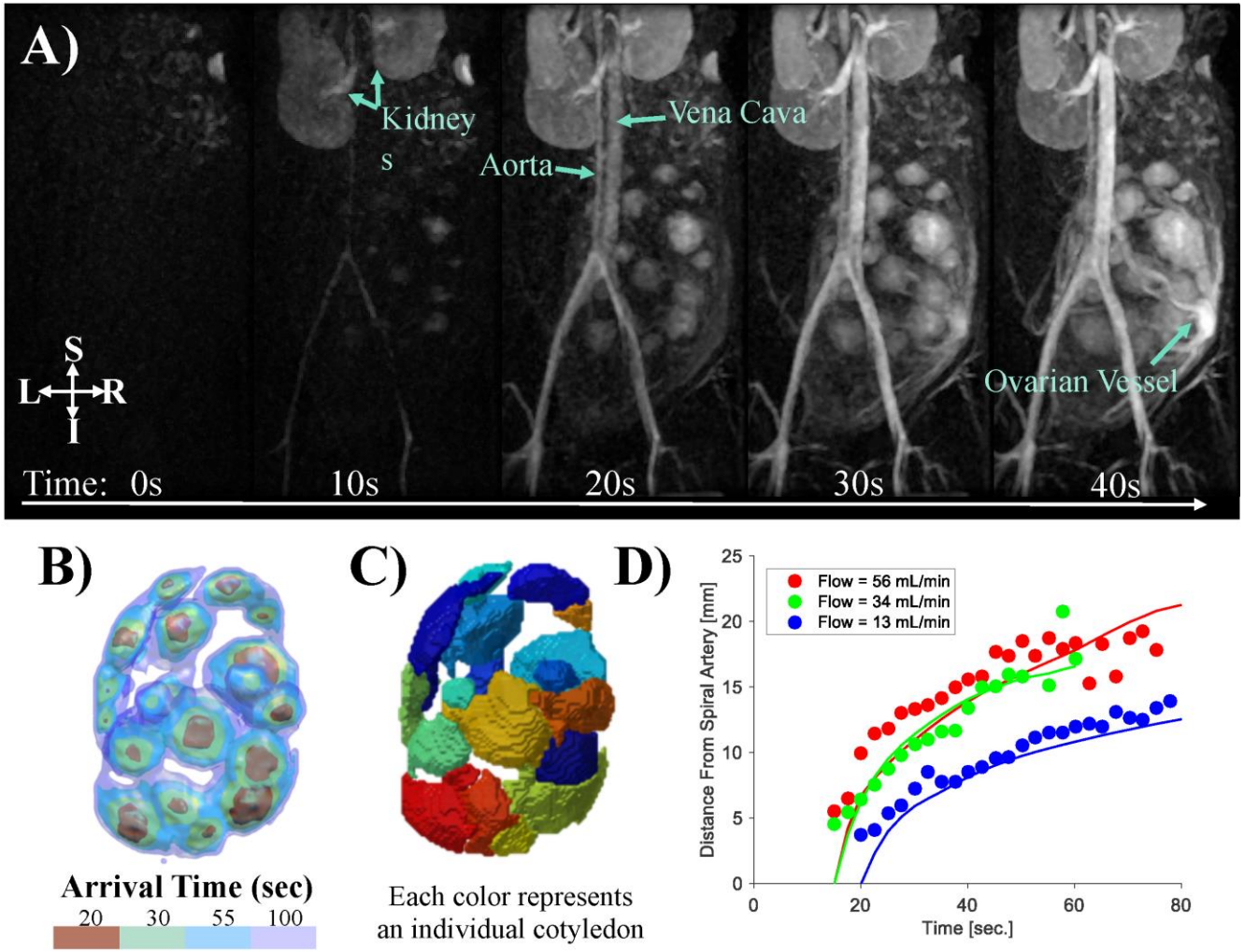

Figure 32. Ferumoxytol DCE-MRI analysis of an animal. Maximum intensity projections of T_1-weighted images at multiple time points during ferumoxytol administration (A), the contrast arrival time map (B) and the segmented functional domains (C) of the 3D placental volume, and the regional volumetric flow in three example domains (D) in the same animal in **Figure 31**. (Reprinted from Ludwig et al[140] with permission from Dr. Kai Ludwig)

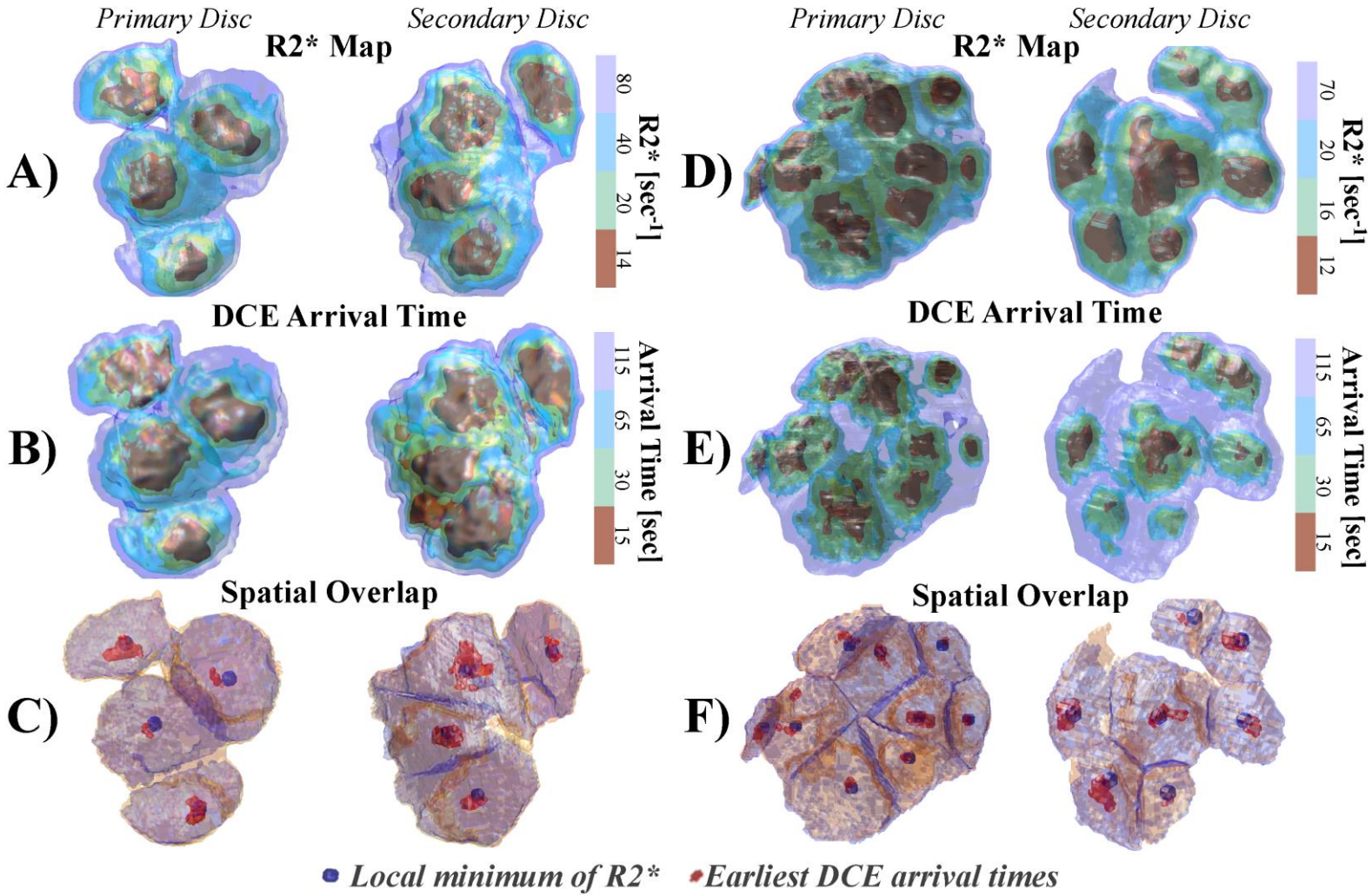

Figure 33. Example functional domain analysis of two animals. Example R_2^* maps (A and D), contrast arrival time maps (B and E), and the spatial overlapped functional domains segmented from the two maps (purple isosurfaces: R_2^* mapping; red isosurfaces: DCE-MRI in C and F) of two animals. 8 (left) and 16 (right) functional domains were identified in the two animals, respectively. The local minimum of R_2^* and early DCE arrival time identified from R_2^* maps and DCE arrival time maps were indicated by purple and red points, separately.

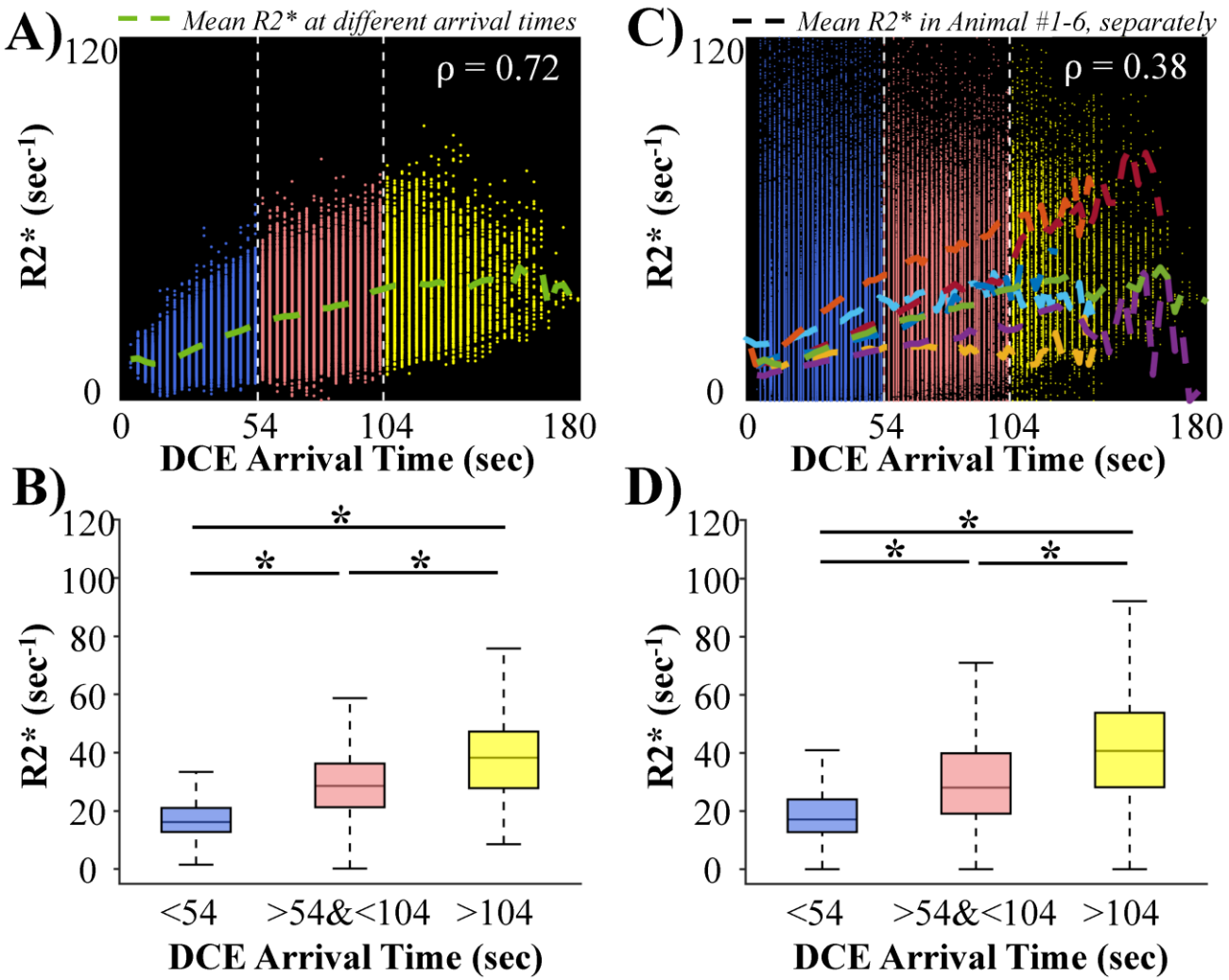

Figure 34. Comparison of ferumoxytol arrival time and R_2^* in animal placentas. Comparison of the DCE arrival time versus R_2^* in all placental voxels in example animal (A) and all N animals (C), and the corresponding Box-and-whisker plots (B and D). A Wilcoxon rank-sum test shows statistically significant differences among 3 groups with early arrival time (<54 sec), middle arrival time (>54 sec and <104 sec), and late arrival time (>104 sec). *P<.05

Table 18. Quantitative MRI measurements on functional domains.

Animal Index	Intervention	R2*-Mapping based BOLD Measurements					Ferumoxytol-enhanced DCE	
		# of Functional Domains Total	**Domain Volume** Mean ± SD (Max – Min) [cm^3]	**Median R_{20}^*** Mean ± SD (Max – Min) [sec^{-1}]	**Median [$Hb_{o,f}$]** Mean ± SD (Max – Min) [mM]	**Median v_iPS/Φ** Mean ± SD (Max – Min) [$\times 10^6$ cm^{-3}]	**# of Functional Domains** Total	**Domain Volume** Mean ± SD (Max – Min) [cm^3]
1	None	16	2.1±1.3 (0.2-4.7)	9.3±3.5 (4.8-18.7)	4.7±0.9 (2.2-6.2)	1.1±2.4 (0.1-10.1)	18	2.8 ± 1.7 (0.3 – 5.8)
2		18	1.3±0.8 (0.3-2.9)	10.0±5.5 (1.8-24.3)	5.3±1.1 (2.1, 6.5)	3.0±4.6 (0.1-16.3)	17	2.1 ± 1.4 (0.3 – 5.3)
3	Saline	9	2.5±1.9 (0.1-5.6)	9.4±1.9 (6.9-13.1)	6.3±0.2 (6.1, 6.6)	1.4±1.1 (0.1, 3.6)	13	1.8 ± 1.7 (0.1 – 5.7)
4		16	2.9±1.9 (0.6-6.6)	9.5±1.5 (7.3-13.7)	5.7±0.8 (3.5-6.3)	0.4±0.3 (0.1-1.0)	18	2.5 ± 2.3 (0.4 – 7.9)
5		8	5.0±1.7 (2.3-8.0)	8.4±0.7 (7.4-9.5)	5.6±0.6 (4.3-6.3)	0.2±0.1 (0.1-0.4)	8	6.3 ± 2.8 (3.4 – 12.5)
6		15	2.0±0.9 (0.5-4.1)	7.8±2.5 (2.1-12.7)	6.2±0.2 (6.5-5.6)	1.5±1.8 (0.1-5.8)	16	1.8 ± 1.2 (0.1 – 4.5)
Average		14.3±4.1	2.5 ± 1.3 (0.1-8.0)	9.1±0.8	5.7±0.6	1.5±1.1	15.0±3.9	2.9 ± 1.7 (0.1-12.5)

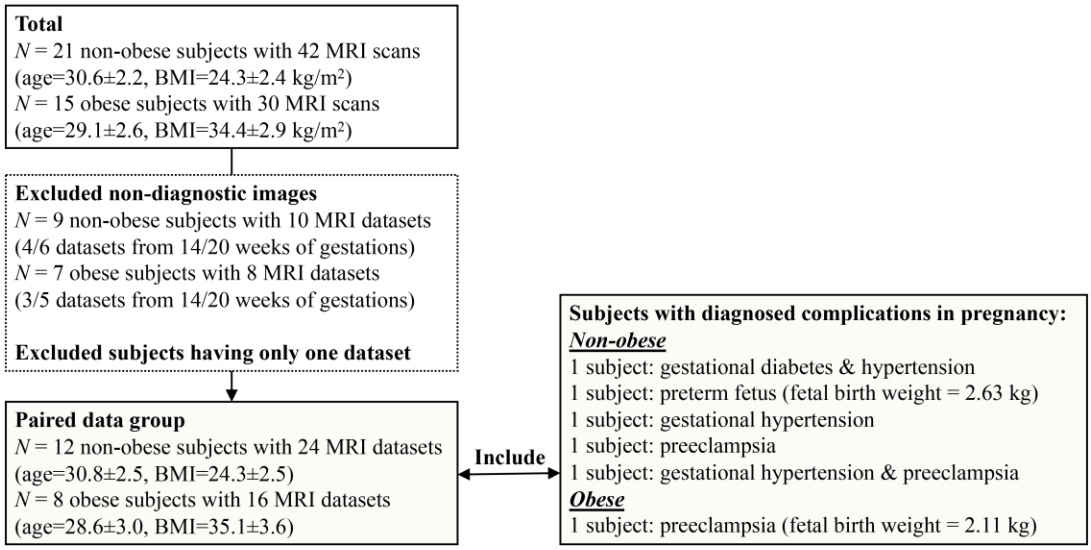

Figure 35. Flow chart shows the study design and subjects' information.

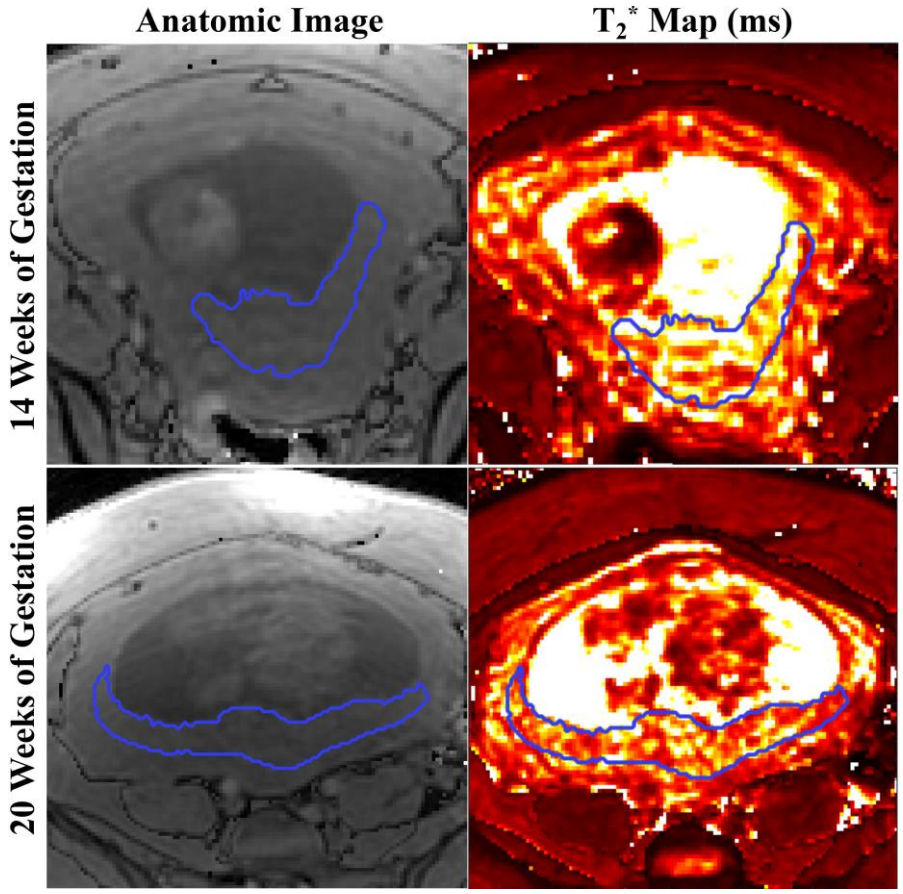

Figure 36. Example placental images of a human subject. Example anatomic images and T_2^* maps of an obese subject at 14 weeks of gestation and 20 weeks of gestation. The placenta contours are delineated with blue lines.

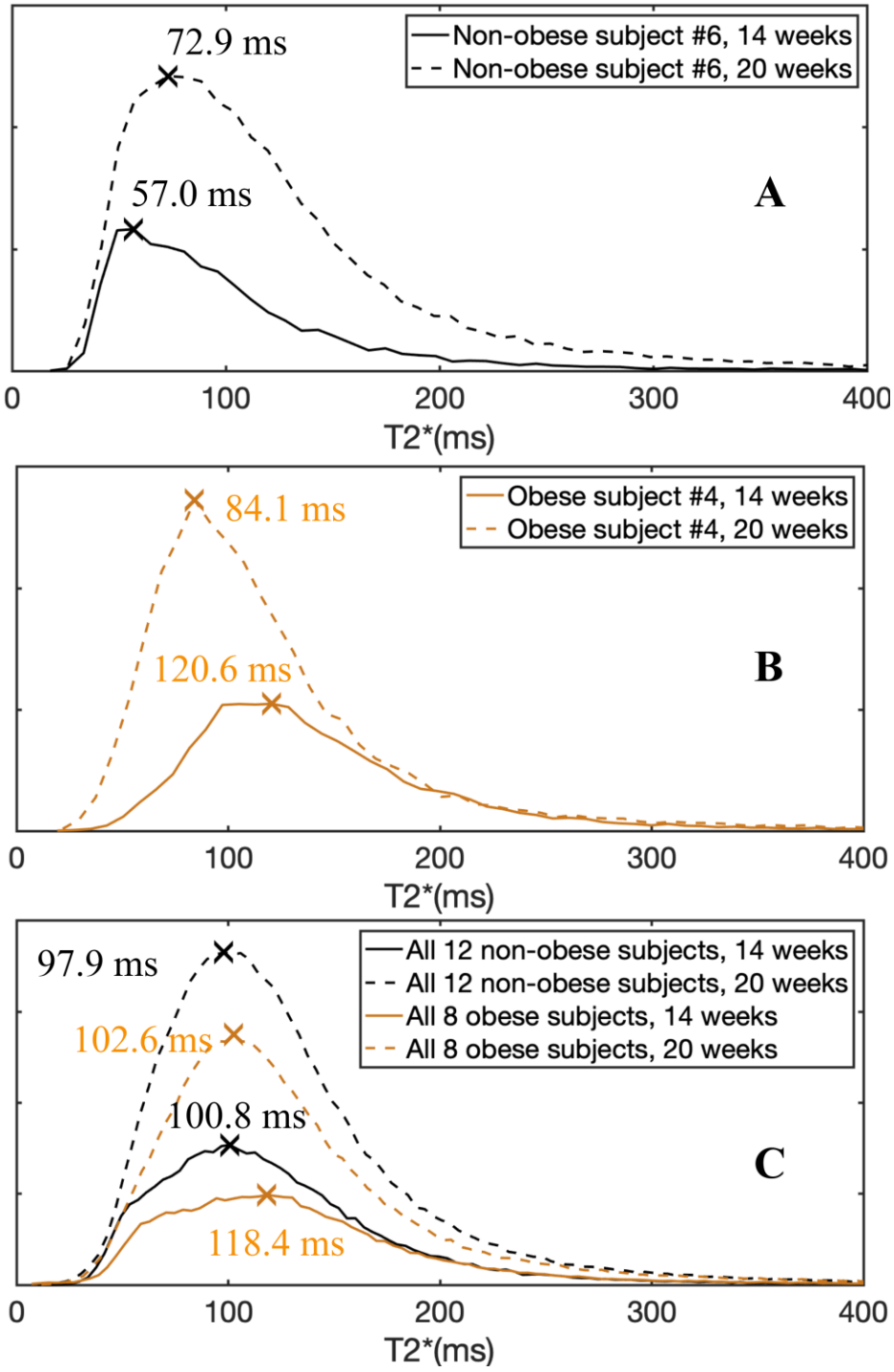

Figure 37. Histograms of placental T_2^* in human subjects. Histograms of placental T_2^* in one non-obese subject (A), one obese subject (B), and all 12 non-obese/ 8 obese subjects (C) at 14 weeks of gestation (solid lines) and 20 weeks of gestation (dashed lines). The mode of the placental T_2^* is shown with the marker "x". The histograms of all non-obese/obese subjects (C) are normalized by the number of subjects.

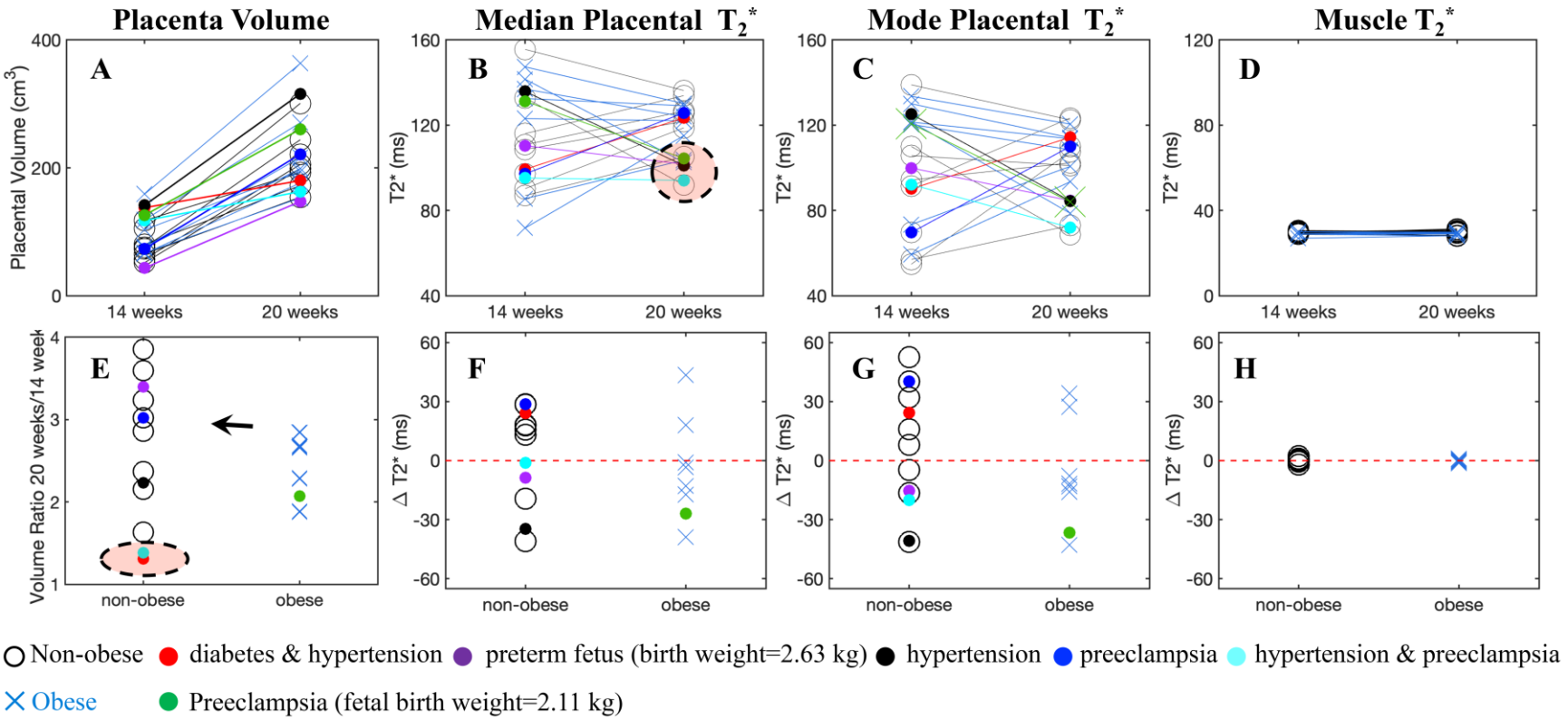

Figure 38. Measurements of MRI parameters in human placentas. Measurements of placenta volume (A), median placental T_2^* (B), mode placental T_2^* (C), and mean muscle T_2^* (D) of the 12 non-obese subjects (black circles) and the 8 obese subjects (orange circles) at 14/20 weeks of gestation, and the placenta volume ratio (E), the change of median placental T_2^* (F), mode placental T_2^* (G) and muscle T_2^* (H) between measurements at the two gestational ages. Subjects with diagnosed complications in pregnancy are indicated at the bottom of the figure. Median and mode values are both shown to provide comprehensively assessment of placental T_2^*.

Chapter

7. Summary and Future Works

7.1 Summary

This thesis incorporates development of MRI pulse sequence, signal model, image reconstruction, image post-processing and data analysis, and assessment of techniques in simulation, phantom, animal and human studies.

A multi-component liver signal model including water, fat, and the recently observed short T_2^* signal was proposed and a UTE-CSE acquisition with optimized echo time was used to quantify ST2 at both 1.5T and 3.0T. ST2 was demonstrated to consistently exist in human liver. Further, PDFF quantification in CSE acquisition with short echo times was demonstrated to be biased if the ST2 was uncounted in the liver signal model. The preliminarily quantified signal fraction and T_2^* of ST2 will guide future studies on accurate liver signal modeling at short TEs and may enable improved accuracy of PDFF estimations for the detection of NAFLD.

A numerical abdominal phantom was developed and in vivo liver CSE-MRI was analyzed to assess the bias on liver QSM with anisotropic imaging resolution. The low image resolution was shown to lead to different amounts of bias on the susceptibility contrast depending on the downsampling directions in liver QSM. This preliminary study may guide future design of liver QSM scan protocols for improving the accuracy of quantifying LIC.

Ferumoxytol-enhanced R_2^* and QSM were developed for tracking longitudinal iron deposition in the placenta. The technique feasibility was demonstrated in a nonhuman primate model. Further, stable MRI measurements indicated no evidence of iron deposition in fetal tissues of nonhuman primates after maternal ferumoxytol exposure at late second trimester. Upon successful detection of macrophage homing in an effective inflammation model and being proven safe, ferumoxytol-enhanced MRI may enable assessment of the inflammation at the maternal-fetal interface in human pregnancy.

A motion-robust 2D sequential CSE-MRI technique with a short temporal footprint for each slice was investigated for ferumoxytol-enhanced MRI of inflammation at maternal-fetal interface. The accuracy of placental R_2^* and B_0 field map boundary measurements in the proposed 2D technique was evaluated by comparing with the reference 3D CSE-MRI technique in pregnant rhesus macaques, which were anesthetized eliminating fetal motion. High correlations between the measurements from 2D and 3D-CSE-MRI were demonstrated. Further, the motion-robustness and good repeatability of 2D CSE-MRI for placental R_2^* were also demonstrated in pregnant women without ferumoxytol administration. 2D CSE-MRI provides promise for motion-robust human placental MRI.

R_2^*-mapping based BOLD contrast using 3D respiratory-gated CSE-MRI was developed to quantify regional placental oxygenation in individual cotyledons in nonhuman primates and assess longitudinal placental oxygenation changes in obese pregnant women. Placental R_2^* showed spatial correlation with ferumoxytol DCE arrival time, indicating substantial correlation between placental oxygenation and perfusion. The segmented functional domains by using R_2^* map are similar to the reported number of domains in rhesus macaques. Further, placental oxygenation in human subjects was observed to be subject-specific at the early gestational window (14-20 weeks).

Small placental volume increases between 14 and 20 weeks of gestations and relatively high placental R_2^* values were observed in subjects with pregnancy complications. R_2^*-mapping may provide an alternative safe technique using endogenous MRI contrast to assess placental oxygenation and predict pregnancy outcome.

7.2 Future Works

7.2.1 Quantification of short T_2^* signal component in the liver at 1.5T

This future work seeks to quantify liver short T_2^* signal component in patients with liver cirrhosis and compare the signal fraction with that in healthy volunteers at 1.5T. As shown in our preliminary estimation of ST2 in healthy volunteers who were imaged at both 3.0T and 1.5T (Chapter 2), a longer $T_{2,\zeta}^*$ was estimated at 1.5T compared to the estimation at 3.0T in the same subject. The longer $T_{2,\zeta}^*$ at 1.5T leads to a slow signal decay and thus more signals of ST2 can be captured for accurate quantification. Further studies on characterization of ST2 in patients with liver cirrhosis at 1.5T, which has not been performed in this work, is of great interest.

In this future work, a UTE-CSE acquisition with ~10 mins scan time will be achieved and added as clinic add-on scan after obtaining informed written consent in patients. Echo times will be optimized through Cramér-Rao lower bound[59] based on the preliminarily estimated range of the signal fraction and $T_{2,\zeta}^*$ of ST2 at 1.5T (Chapter 2). A relatively low spatial resolution, e.g., 3 mm isotropic resolution will be used in order to shorten the total scan time. SNR is also expected to increase due to the low resolution, which may stabilize the signal fitting for the estimation of ST2. Healthy volunteers will be recruited and scanned using the same imaging protocol at 1.5T. The

signal fraction and $T_{2,\zeta}^{*}$ of ST2 will be compared between patients with liver cirrhosis and healthy volunteers through statistical analysis, e.g. Student's t-test. This future work may provide comprehensive analysis of ST2 in different cohorts at 1.5T and it may also enable preliminary analysis on the variation of ST2 quantification using different protocols.

7.2.2 Further characterization of resolution effects on liver QSM

The susceptibility estimate has shown to depend on reconstruction algorithm[15] including the background field removal and dipole inversion. MEDI-based QSM reconstruction has been widely used for brain and has been increasingly used in body applications[70] in recent years. We have tested the reconstruction pipeline of liver QSM using MEDI and preliminarily results look promising in both digital phantom and in vivo data, as shown in **Figure 39**. This future work seeks to characterize resolution introduced bias on liver QSM using MEDI. Data analysis will be performed on both the numerical abdominal phantom and in vivo data (Chapter 3). The effect of resolution along different directions including liver left-right and superior-inferior directions will be characterized separately and compared with the results in Chapter 3. This future work may provide preliminary assessment of the accuracy of liver susceptibility estimations using different reconstruction algorithms.

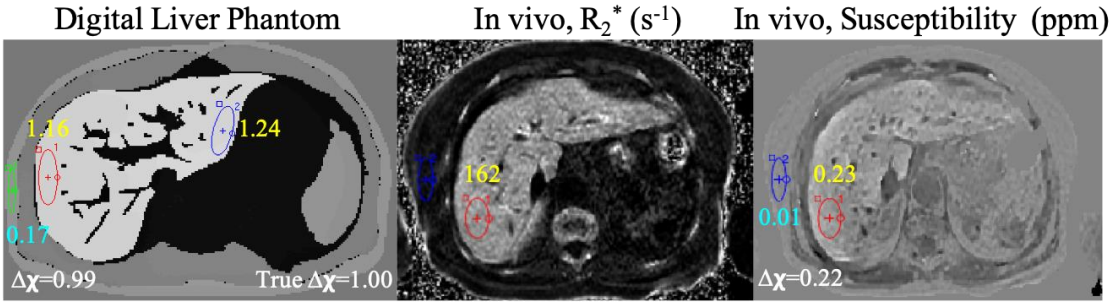

Figure 39. Liver QSM using MEDI reconstruction. Liver susceptibility measurements of a digital liver phantom and in vivo data estimated using MEDI reconstruction.

7.2.3 Further assessment of placental function and health using R_2^*-mapping

A Zika-infected rhesus macaque model was recently used to analyze placental tissue histology and its correlation with MRI biomarkers including tissue perfusion (Seiter D, et al. ISMRM 2020 abstract #3834). Cotyledon was segmented using ferumoxytol DCE-MRI and the cotyledon volume was observed to be significantly smaller in animals with pathology. This future work seeks to quantify placental oxygenation in these Zika-infected animals using the built pipeline of R_2^*-mapping based technique as stated in Chapter 6.

R_2^* map will be registered to DCE images and pixel-by-pixel correlation of R_2^* and ferumoxytol arrival time will be analyzed to study the correlation between oxygenation and perfusion. Individual cotyledon will be segmented in R_2^* map and the number and volume of cotyledons will be compared with pathology findings. Quantitative parameters including the scaled oxygen transport to fetal blood $\frac{v_i PS}{\phi}$, which has shown to correlate with pathology in previous studies[126], will also be estimated. Statistical analysis will be used to compare oxygenation between Zika-infected animals and healthy controls. This future work will provide opportunity to assess the correlation of MRI-based oxygenation with pathology and also assess the feasibility of using placental R_2^* as a biomarker to indicate placental hypoxia.

Bibliography

1. Bonny J-M. Methods and applications of quantitative MRI. *Annual Reports on NMR Spectroscopy*. 2005;56:213-229.

2. Deng J, Wang Y. Quantitative magnetic resonance imaging biomarkers in oncological clinical trials: Current techniques and standardization challenges. *Chronic Dis Transl Med*. 2017;3(1):8-20.

3. Hernando D, Levin YS, Sirlin CB, Reeder SB. Quantification of liver iron with MRI: State of the art and remaining challenges. *J Magn Reson Imaging*. 2014;40(5):1003-1021.

4. Sharma SD, Hernando D, Horng DE, Reeder SB. Quantitative susceptibility mapping in the abdomen as an imaging biomarker of hepatic iron overload. *Magn Reson Med*. 2015;74(3):673-683.

5. Pohlmann A, Arakelyan K, Hentschel J, Cantow K, Flemming B, Ladwig M, Waiczies S, Seeliger E, Niendorf T. Detailing the relation between renal T2* and renal tissue pO2 using an integrated approach of parametric magnetic resonance imaging and invasive physiological measurements. *Invest Radiol*. 2014;49(8):547-560.

6. Preiss D, Sattar N. Non-alcoholic fatty liver disease: an overview of prevalence, diagnosis, pathogenesis and treatment considerations. *Clin Sci*. 2008;115(5):141 LP - 150.

7. Reeder SB, Cruite I, Hamilton G, Sirlin CB. Quantitative assessment of liver fat with magnetic resonance imaging and spectroscopy. *J Magn Reson Imaging*. 2011;34(4):729-749.

8. Reeder SB, Hu HH, Sirlin CB. Proton density fat-fraction: A standardized mr-based biomarker of tissue fat concentration. *J Magn Reson Imaging*. 2012;36(5):1011-1014.

9. Hernando D, Reeder SB, Motosugi U. Bias in liver fat quantification using chemical shift-encoded techniques with short echo times. In: *Proc 23rd Annual Meeting ISMRM*; 2015.

10. de Jong S, Zwanenburg JJ, Visser F, van der Nagel R, van Rijen HV, Vos MA, de Bakker JM, Luijten PR. Direct detection of myocardial fibrosis by MRI. *J Mol Cell Cardiol*. 2011;51(6):974-979.

11. Tyler DJ, Robson MD, Henkelman RM, Young IR, Bydder GM. Magnetic resonance imaging with ultrashort TE (UTE) PULSE sequences: Technical considerations. *J Magn Reson Imaging*. 2007;25(2):279-289.

12. Siu AG, Ramadeen A, Hu X, Morikawa L, Zhang L, Lau JY, Liu G, Pop M, Connelly KA, Dorian P, Wright GA. Characterization of the ultrashort-TE (UTE) MR collagen signal. *NMR Biomed*. 2015;28(10):1236-1244.

13. Brittenham GM, Badman DG. Noninvasive measurement of iron: report of an NIDDK workshop. *Blood*. 2003;101(1):15-19.

14. Zhou D, Cho J, Zhang J, Spincemaille P, Wang Y. Susceptibility underestimation in a high-susceptibility phantom: Dependence on imaging resolution, magnitude contrast, and other parameters. *Magn Reson Med*. 2017;78(3):1080-1086.

15. Karsa A, Punwani S, Shmueli K. The effect of low resolution and coverage on the accuracy of susceptibility mapping. *Magn Reson Med*. 2019;81:1833-1848.

16. Faas MM, Spaans F, De Vos P. Monocytes and macrophages in pregnancy and pre-

eclampsia. *Immune Interact Dur Reprod Cycle*. 2015:33.

17. Knobloch G, Colgan T, Wiens CN, Wang X, Schubert T, Hernando D, Sharma SD, Reeder SB. Relaxivity of Ferumoxytol at 1.5 T and 3.0 T. *Invest Radiol*. 2018;53(5):257-263.

18. Liu S, Brisset J, Hu J, Haacke EM, Ge Y. Susceptibility weighted imaging and quantitative susceptibility mapping of the cerebral vasculature using ferumoxytol. *J Magn Reson Imaging*. 2018;47(3):621-633.

19. Gaglia JL, Harisinghani M, Aganj I, Wojtkiewicz GR, Hedgire S, Benoist C, Mathis D, Weissleder R. Noninvasive mapping of pancreatic inflammation in recent-onset type-1 diabetes patients. *Proc Natl Acad Sci*. 2015;112(7):2139-2144.

20. Hernando D, Cook RJ, Diamond C, Reeder SB. Magnetic susceptibility as a B0 field strength independent MRI biomarker of liver iron overload. *Magn Reson Med*. 2013;70(3):648-656.

21. Rivera-Rivera LA, Schubert T, Knobloch G, Turski PA, Wieben O, Reeder SB, Johnson KM. Comparison of ferumoxytol-based cerebral blood volume estimates using quantitative R1 and relaxometry. *Magn Reson Med*. 2018;79(6):3072-3081.

22. Christen T, Ni W, Qiu D, Schmiedeskamp H, Bammer R, Moseley M, Zaharchuk G. High-resolution cerebral blood volume imaging in humans using the blood pool contrast agent ferumoxytol. *Magn Reson Med*. 2013;70(3):705-710.

23. Stirrat CG, Alam SR, MacGillivray TJ, Gray CD, Forsythe R, Dweck MR, Payne JR, Prasad SK, Petrie MC, Gardner RS, Mirsadraee S. Ferumoxytol-enhanced magnetic

resonance imaging methodology and normal values at 1.5 and 3T. *J Cardiovasc Magn Reson*. 2016;18(1):46.

24. Neuwelt A, Sidhu N, Hu C-AA, Mlady G, Eberhardt SC, Sillerud LO. Iron-Based Superparamagnetic Nanoparticle Contrast Agents for MRI of Infection and Inflammation. *Am J Roentgenol*. 2015;204(3):W302-W313.

25. Prayer D, Brugger PC, Prayer L. Fetal MRI: techniques and protocols. *Pediatr Radiol*. 2004;34(9):685-693.

26. Armstrong T, Liu D, Martin T, Masamed R, Janzen C, Wong C, Chanlaw T, Devaskar SU, Sung K, Wu HH. 3D Mapping of the Placenta During Early Gestation Using Free-Breathing Multiecho Stack-of-Radial MRI at 3T. *J Magn Reson Imaging*. 2019;49:291-303.

27. Pooler BD, Hernando D, Ruby JA, Ishii H, Shimakawa A, Reeder SB. Validation of a motion-robust 2D sequential technique for quantification of hepatic proton density fat fraction during free breathing. *J Magn Reson Imaging*. 2018;48(6):1578-1585.

28. Keraudren K, Kuklisova-Murgasova M, Kyriakopoulou V, Malamateniou C, Rutherford MA, Kainz B, Hajnal JV, Rueckert D. Automated fetal brain segmentation from 2D MRI slices for motion correction. *Neuroimage*. 2014;101:633-643.

29. Levine D, Barnes PD, Sher S, Semelka RC, Li W, McArdle CR, Worawattanakul S, Edelman RR. Fetal fast MR imaging: reproducibility, technical quality, and conspicuity of anatomy. *Radiology*. 1998;206(2):549-554.

30. Schabel MC, Roberts VHJ, Lo JO, Platt S, Grant KA, Frias AE, Kroenke CD. Functional

imaging of the nonhuman primate Placenta with endogenous blood oxygen level–dependent contrast. *Magn Reson Med*. 2016;76(5):1551-1562.

31. Frias AE, Schabel MC, Roberts VHJ, Tudorica A, Grigsby PL, Oh KY, Kroenke CD. Using dynamic contrast-enhanced MRI to quantitatively characterize maternal vascular organization in the primate placenta. *Magn Reson Med*. 2015;73(4):1570-1578.

32. Howell KR, Powell TL. Effects of maternal obesity on placental function and fetal development. *Reproduction*. 2017;153(3):R97.

33. Slator PJ, Hutter J, Palombo M, Jackson LH, Ho A, Panagiotaki E, Chappell LC, Rutherford MA, Hajnal JV, Alexander DC. Combined diffusion-relaxometry MRI to identify dysfunction in the human placenta. *Magn Reson Med*. 2019;82(1):95-106.

34. Armstrong T, Liu D, Martin T, Masamed R, Janzen C, Wong C, Chanlaw T, Devaska SU, Sung K, Wu HH. 3D mapping of the placenta during early gestation using free-breathing multiecho stack-of-radial MRI at 3T. *J Magn Reson Imaging*. 2019;49(1):291-303.

35. Sørensen A, Hutter J, Seed M, Grant PE, Gowland P. T2* weighted placental MRI: basic research tool or an emerging clinical test of placental dysfunction? *Ultrasound Obstet Gynecol*. 2019.

36. Schabel MC, Roberts VHJ, Rincon M, Gaffney J, Lo JO, Gibbins KJ, Blue N, Morrel GR, Kroenke CD, Silver RM, Frias AE. A longitudinal multisite study of endogenous BOLD MRI in human pregnancies. In: *Proc 27th Annual Meeting ISMRM*; 2019:1075.

37. Rinella ME. Nonalcoholic Fatty Liver Disease: A Systematic ReviewNonalcoholic Fatty Liver DiseaseNonalcoholic Fatty Liver Disease. *JAMA*. 2015;313(22):2263-2273.

38. Loomba R, Sanyal AJ. The global NAFLD epidemic. *Nat Rev Gastroenterol &Amp; Hepatol*. 2013;10:686.

39. Kühn J-P, Hernando D, Mensel B, Kruger PC, Ittermann T, Mayerle J, Hosten N, Reeder SB. Quantitative chemical shift-encoded MRI is an accurate method to quantify hepatic steatosis. *J Magn Reson Imaging*. 2014;39(6):1494-1501.

40. Yokoo T, Serai SD, Pirasteh A, Bashir MR, Hamilton G, Hernando D, Hu HH, Hetterich H, Kuhn JP, Kukuk GM, Loomba R. Linearity, Bias, and Precision of Hepatic Proton Density Fat Fraction Measurements by Using MR Imaging: A Meta-Analysis. *Radiology*. 2017;286(2):486-498.

41. Liu C-Y, McKenzie CA, Yu H, Brittain JH, Reeder SB. Fat quantification with IDEAL gradient echo imaging: Correction of bias from T1 and noise. *Magn Reson Med*. 2007;58(2):354-364.

42. Hines CDG, Frydrychowicz A, Hamilton G, Tudorascu DL, Vigen KK, Yu HH, McKenzie CA, Sirlin CB, Brittain JH, Reeder SB. T1 independent, T2* corrected chemical shift based fat–water separation with multi-peak fat spectral modeling is an accurate and precise measure of hepatic steatosis. *J Magn Reson Imaging*. 2011;33(4):873-881.

43. Hernando D, Sharma SD, Kramer H, Reeder SB. On the confounding effect of temperature on chemical shift-encoded fat quantification. *Magn Reson Med*. 2014;72(2):464-470.

44. Colgan TJ, Hernando D, Sharma SD, Reeder SB. The effects of concomitant gradients on chemical shift encoded MRI. *Magn Reson Med*. 2017;78(2):730-738.

45. Ruschke S, Eggers H, Kooijman H, Diefenbach MN, Baum T, Haase A, Rummeny EJ, Hu HH, Karampinos DC. Correction of phase errors in quantitative water–fat imaging using a monopolar time-interleaved multi-echo gradient echo sequence. *Magn Reson Med*. 2017;78(3):984-996.

46. Hernando D, Motosugi U, Reeder SB. Bias in liver fat quantification using chemical shift-encoded techniques with short echo times. In: *Proc 23rd Annual Meeting ISMRM*; 2015:337.

47. Armstrong T, Dregely I, Stemmer A, Han F, Natsuaki Y, Sung K, Wu HH. Free-breathing liver fat quantification using a multiecho 3D stack-of-radial technique. *Magn Reson Med*. 2018;79(1):370-382.

48. Bauman G, Johnson KM, Bell LC, Velikina JV, Samsonov AA, Nagle SK, Fain SB. Three-dimensional pulmonary perfusion MRI with radial ultrashort echo time and spatial–temporal constrained reconstruction. *Magn Reson Med*. 2015;73(2):555-564.

49. Johnson KM, Fain SB, Schiebler ML, Nagle S. Optimized 3D ultrashort echo time pulmonary MRI. *Magn Reson Med*. 2013;70(5):1241-1250.

50. Chappell KE, Patel N, Gatehouse PD, Main J, Puri BK, Taylor-Robinson SD, Bydder GM. Magnetic resonance imaging of the liver with ultrashort TE (UTE) pulse sequences. *J Magn Reson Imaging*. 2003;18(6):709-713.

51. CA Araujo E, Azzabou N, Vignaud A, Guillot G, Carlier PG. Quantitative ultrashort TE imaging of the short-T2 components in skeletal muscle using an extended echo-subtraction method. *Magn Reson Med*. 2017;78:998-1008.

52. Du J, Ma G, Li S, Carl M, Szeverenyi NM, VandenBerg S, Corey-Bloom J, Bydder GM. Ultrashort echo time (UTE) magnetic resonance imaging of the short T2 components in white matter of the brain using a clinical 3T scanner. *Neuroimage*. 2014;87:32-41.

53. Boucneau T, Cao P, Tang S, Han M, Xu D, Henry RG, Larson PE. In vivo characterization of brain ultrashort-T2 components. *Magn Reson Med*. 2018;80(2):726-735.

54. Hernando D, Kramer JH, Reeder SB. Multipeak fat-corrected complex R2* relaxometry: Theory, optimization, and clinical validation. *Magn Reson Med*. 2013;70(5):1319-1331.

55. Hernando D, Hines CDG, Yu H, Reeder SB. Addressing phase errors in fat-water imaging using a mixed magnitude/complex fitting method. *Magn Reson Med*. 2012;67(3):638-644.

56. Walsh DM, Gmitro AB, Marcellin MW. Adaptive reconstruction of phased array MR imagery. *Magn Reson Med*. 2000;43(5):682-690.

57. Hamilton G, Middleton MS, Hooker JC, Haufe WM, Forbang NI, Allison MA, Loomba R, Sirlin CB. In vivo breath-hold 1H MRS simultaneous estimation of liver proton density fat fraction, and T1 and T2 of water and fat, with a multi-TR, multi-TE sequence. *J Magn Reson Imaging*. 2015;42(6):1538-1543.

58. Hamilton G, Yokoo T, Bydder M, Cruite I, Schroeder ME, Sirlin CB, Middleton MS. In vivo characterization of the liver fat 1H MR spectrum. *NMR Biomed*. 2011;24(7):784-790.

59. Pineda AR, Reeder SB, Wen Z, Pelc NJ. Cramér–Rao bounds for three-point decomposition of water and fat. *Magn Reson Med*. 2005;54(3):625-635.

60. Rojkind M, Giambrone M-A, Biempica L. Collagen Types in Normal and Cirrhotic Liver.

Gastroenterology. 1979;76(4):710-719.

61. Wood JC, Zhang P, Rienhoff H, Abi-Saab W, Neufeld E. R2 and R2* are equally effective in evaluating chronic response to iron chelation. *Am J Hematol*. 2014;89(5):505-508.

62. Doyle EK, Toy K, Valdez B, Chia JM, Coates T, Wood JC. Ultra-short echo time images quantify high liver iron. *Magn Reson Med*. 2018;79(3):1579-1585.

63. Krafft AJ, Loeffler RB, Song R, Tipirneni-Sajja A, McCarville MB, Robson MD, Hankins JS, Hillenbrand CM. Quantitative ultrashort echo time imaging for assessment of massive iron overload at 1.5 and 3 Tesla. *Magn Reson Med*. 2017;78(5):1839-1851.

64. Johnson E, Pauly K, Pauly J. Improved short-T2* estimation with Bloch equation-modeled concurrent excitation and relaxation. *Proc 25th Annu Meet ISMRM*. 2017:774.

65. Batts KP. Iron overload syndromes and the liver. *Mod Pathol*. 2007;20(1):S31-S39.

66. Brittenham GM, Sheth S, Allen CJ, Farrell DE. Noninvasive methods for quantitative assessment of transfusional iron overload in sickle cell disease. *Semin Hematol*. 2001;38:37-56.

67. St. Pierre TG, Clark PR, Chua-anusorn W, Fleming AJ, Jeffrey GP, Olynyk JK, Pootrakul P, Robins E, Lindeman R. Noninvasive measurement and imaging of liver iron concentrations using proton magnetic resonance. *Blood*. 2005;105(2):855-861.

68. Hankins JS, McCarville MB, Loeffler RB, Smeltzer MP, Onciu M, Hoffer FA, Li CS, Wang WC, Ware RE, Hillenbran CM. R2* magnetic resonance imaging of the liver in patients with iron overload. *Blood*. 2009;113(20):4853-4855.

69. Colgan TJ, Knobloch G, Reeder SB, Hernando D. Sensitivity of quantitative relaxometry and susceptibility mapping to microscopic iron distribution. *Magn Reson Med*. 2020;83(2):673-680.

70. Li J, Lin H, Liu T, Zhang Z, Prince MR, Gillen K, Yan X, Song Q, Hua T, Zhao X, Zhang M. Quantitative susceptibility mapping (QSM) minimizes interference from cellular pathology in R2* estimation of liver iron concentration. *J Magn Reson Imaging*. 2018;48(4):1069-1079.

71. Ghugre NR, Wood JC. Relaxivity-iron calibration in hepatic iron overload: Probing underlying biophysical mechanisms using a Monte Carlo model. *Magn Reson Med*. 2011;65(3):837-847.

72. Schenck JF. The role of magnetic susceptibility in magnetic resonance imaging: MRI magnetic compatibility of the first and second kinds. *Med Phys*. 1996;23(6):815-850.

73. Haacke EM, Liu S, Buch S, Zheng W, Wu D, Ye Y. Quantitative susceptibility mapping: current status and future directions. *Magn Reson Imaging*. 2015;33(1):1-25.

74. Sun H, Seres P, Wilman AH. Structural and functional quantitative susceptibility mapping from standard fMRI studies. *NMR Biomed*. 2017;30(4):e3619.

75. Lu X, Ma Y, Chang EY, He Q, Searleman A, von Drygalski A, Du J. Simultaneous quantitative susceptibility mapping (QSM) and for high iron concentration quantification with 3D ultrashort echo time sequences: An echo dependence study. *Magn Reson Med*. 2018;79(4):2315-2322.

76. Hernando D, Kellman P, Haldar JP, Liang Z-P. Robust water/fat separation in the

presence of large field inhomogeneities using a graph cut algorithm. *Magn Reson Med*. 2010;63(1):79-90.

77. Simchick G, Liu Z, Nagy T, Xiong M, Zhao Q. Assessment of MR-based and quantitative susceptibility mapping for the quantification of liver iron concentration in a mouse model at 7T. *Magn Reson Med*. 2018;80(5):2081-2093.

78. Chen Z, Liu J, Calhoun VD. Susceptibility-based functional brain mapping by 3D deconvolution of an MR-phase activation map. *J Neurosci Methods*. 2013;216(1):33-42.

79. Bianciardi M, van Gelderen P, Duyn JH. Investigation of BOLD fMRI resonance frequency shifts and quantitative susceptibility changes at 7 T. *Hum Brain Mapp*. 2014;35(5):2191-2205.

80. LaMarca B, Cornelius DC, Harmon AC, Amaral LM, Cunningham MW, Faulkner JL, Wallace K. Identifying immune mechanisms mediating the hypertension during preeclampsia. *Am J Physiol Integr Comp Physiol*. 2016;311(1):R1-R9.

81. Kohli S, Ranjan S, Hoffmann J, Kashif M, Daniel EA, Al-Dabet MD, Bock F, Nazir S, Huebner H, Mertens PR, Fischer KD. Maternal extracellular vesicles and platelets promote preeclampsia via inflammasome activation in trophoblasts. *Blood, J Am Soc Hematol*. 2016;128(17):2153-2164.

82. Taylor BD, Tang G, Ness RB, Olsen J, Hougaard DM, Skogstrand K, Roberts JM, Haggerty CL. Mid-pregnancy circulating immune biomarkers in women with preeclampsia and normotensive controls. *Pregnancy Hypertens An Int J Women's Cardiovasc Heal*. 2016;6(1):72-78.

83. Jonsson Y, Rubèr M, Matthiesen L, Berg G, Nieminen K, Sharma S, Emerudh J, Ekerfelt C. Cytokine mapping of sera from women with preeclampsia and normal pregnancies. *J Reprod Immunol*. 2006;70(1-2):83-91.

84. Faas MM, Spaans F, De Vos P. Monocytes and macrophages in pregnancy and pre-eclampsia. *Front. Immunol*. 2014;30(5):298.

85. Spinowitz BS, Kausz AT, Baptista J, Noble SD, Sothinathan R, Bernando MV, Brenner L, Pereira BJ. Ferumoxytol for treating iron deficiency anemia in CKD. *J Am Soc Nephrol*. 2008;19(8):1599-1605.

86. Bashir MR, Bhatti L, Marin D, Nelson RC. Emerging applications for ferumoxytol as a contrast agent in MRI. *J Magn Reson Imaging*. 2015;41(4):884-898.

87. Vasanawala SS, Nguyen K-L, Hope MD, Bridges MD, Hope TA, Reeder SB, Bashir MR. Safety and technique of ferumoxytol administration for MRI. *Magn Reson Med*. 2016;75(5):2107-2111.

88. Toth GB, Varallyay CG, Horvath A, Bashir MR, Choyke PL, Daldrup-Link HE, Dosa E, Finn JP, Gahramanov S, Harisinghani M, Macdougall I. Current and potential imaging applications of ferumoxytol for magnetic resonance imaging. *Kidney Int*. 2017;92(1):47-66.

89. Iv M, Samghabadi P, Holdsworth S, Gentles A, Rezaii P, Harsh G, Li G, Thomas R, Moseley M, Daldrup-Link HE, Vogel H. Quantification of Macrophages in High-Grade Gliomas by Using Ferumoxytol-enhanced MRI: A Pilot Study. *Radiology*. 2018(1):198-206.

90. Stirrat CG, Alam SR, MacGillivray TJ, Gray CD, Dweck MR, Raftis J, Jenkins WS, Wallace WA, Pessotto R, Lim KH, Mirsadraee S. Ferumoxytol-enhanced magnetic resonance imaging assessing inflammation after myocardial infarction. *Heart*. 2017;103(19):1528-1535.

91. Oh KY, Roberts VHJ, Schabel MC, Grove KL, Woods M, Frias AE. Gadolinium Chelate Contrast Material in Pregnancy: Fetal Biodistribution in the Nonhuman Primate. *Radiology*. 2015;276(1):110-118.

92. Prola-Netto J, Woods M, Roberts VHJ, Sullivan EL, Miller CA, Frias AE, Oh KY. Gadolinium Chelate Safety in Pregnancy: Barely Detectable Gadolinium Levels in the Juvenile Nonhuman Primate after in Utero Exposure. *Radiology*. 2017;286(1):122-128.

93. Myllynen PK, Loughran MJ, Howard CV, Sormunen R, Walsh AA, Vähäkangas KH. Kinetics of gold nanoparticles in the human placenta. *Reprod Toxicol*. 2008;26(2):130-137.

94. Golos TG. Pregnancy initiation in the rhesus macaque: towards functional manipulation of the maternal-fetal interface. *Reprod Biol Endocrinol*. 2004;2(1):35.

95. Van Esch E, Cline JM, Buse E, Wood CE, de Rijk EPCT, Weinbauer GF. Summary comparison of female reproductive system in human and the cynomolgus monkey (Macaca fascicularis). *Toxicol Pathol*. 2008;36:171S-172S.

96. Blankenship TN, Enders AC, King BF. Trophoblastic invasion and the development of uteroplacental arteries in the macaque: immunohistochemical localization of cytokeratins, desmin, type IV collagen, laminin, and fibronectin. *Cell Tissue Res*. 1993;272(2):227-236.

97. Yu H, Shimakawa A, McKenzie CA, Brodsky E, Brittain JH, Reeder SB. Multiecho water-fat separation and simultaneous R estimation with multifrequency fat spectrum modeling. *Magn Reson Med*. 2008;60(5):1122-1134.

98. Barick KC, Aslam M, Lin Y-P, Bahadur D, Prasad P V, Dravid VP. Novel and efficient MR active aqueous colloidal Fe 3 O 4 nanoassemblies. *J Mater Chem*. 2009;19(38):7023-7029.

99. Laurent S, Forge D, Port M, Roch A, Robic C, Vander Elst L, Muller RN. Magnetic iron oxide nanoparticles: synthesis, stabilization, vectorization, physicochemical characterizations, and biological applications. *Chem Rev*. 2008;108(6):2064-2110.

100. Palomba S, Russo T, Falbo A, Di Cello A, Tolino A, Tucci L, La Sala GB, Zullo F. Macroscopic and microscopic findings of the placenta in women with polycystic ovary syndrome. *Hum Reprod*. 2013;28(10):2838-2847.

101. Breeze ACG, Gallagher FA, Lomas DJ, Smith GCS, Lees CC. Postmortem fetal organ volumetry using magnetic resonance imaging and comparison to organ weights at conventional autopsy. *Ultrasound Obstet Gynecol*. 2008;31(2):187-193.

102. Zhu A, Reeder SB, Johnson KM, Nguyen SM, Golos TG, Shimakawa A, Muehler MR, Francois CJ, Bird IM, Fain SB, Shah DM, Wieben O, Hernando D. Evaluation of a motion-robust 2D chemical shift-encoded technique for R2* and field map quantification in ferumoxytol-enhanced MRI of the placenta in pregnant rhesus macaques. *J Magn Reson Imaging*. 2019.

103. Storey P, Lim RP, Chandarana H, Rosenkrantz AB, Kim D, Stoffel DR, Lee VS. MRI assessment of hepatic iron clearance rates after USPIO administration in healthy adults.

Invest Radiol. 2012;47(12):717-724.

104. Landry R, Jacobs PM, Davis R, Shenouda M, Bolton WK. Pharmacokinetic study of ferumoxytol: a new iron replacement therapy in normal subjects and hemodialysis patients. *Am J Nephrol*. 2005;25(4):400-410.

105. Morris DM, Ross JAS, McVicar A, Semple SI, Haggarty P, Gilbert FJ, Abramovich DR, Smith N, Redpath TW. Changes in foetal liver T2* measurements by MRI in response to maternal oxygen breathing: application to diagnosing foetal growth restriction. *Physiol Meas*. 2010;31(9):1137.

106. Fernández KS, de Alarcón PA. Development of the hematopoietic system and disorders of hematopoiesis that present during infancy and early childhood. *Pediatr Clin*. 2013;60(6):1273-1289.

107. Pahal GS, Jauniaux E, Kinnon C, Thrasher AJ, Rodeck CH. Normal development of human fetal hematopoiesis between eight and seventeen weeks' gestation. *Am J Obstet Gynecol*. 2000;183(4):1029-1034.

108. Nguyen SM, Wiepz GJ, Schotzko M, Simmons HA, Mejia A, Ludwig KD, Zhu A, Bruuner K, Hernando D, Reeder SB, Wieben O. Impact of Ferumoxytol Magnetic Resonance Imaging on the Rhesus Macaque Maternal-Fetal Interface. *Biol Reprod*. September 2019.

109. Presicce P, Senthamaraikannan P, Alvarez M, Rueda CM, Cappelletti M, Miller LA, Jobe AH, Chougnet CA, Kallapur SG. Neutrophil recruitment and activation in decidua with intra-amniotic IL-1beta in the preterm rhesus macaque. *Biol Reprod*. 2015;92(2):51-56.

110. Bashir MR, Bhatti L, Marin D, Nelson RC. Emerging applications for ferumoxytol as a contrast agent in MRI. *J Magn Reson Imaging*. 2015;41(4):884-898.

111. Motosugi U, Hernando D, Bannas P, Holmes JH, Wang K, Shimakawa A, Iwadate Y, Taviani V, Rehm JL, Reeder SB. Quantification of liver fat with respiratory-gated quantitative chemical shift encoded MRI. *J Magn Reson Imaging*. 2015;42(5):1241-1248.

112. Taviani V, Hernando D, Francois CJ, Shimakawa A, Vigen KK, Nagle SK, Schiebler ML, Grist TM, Reeder SB. Whole-heart chemical shift encoded water–fat MRI. *Magn Reson Med*. 2014;72(3):718-725.

113. Sinding M, Peters DA, Frøkjær JB, Christiansen OB, Petersen A, Uldbjerg N, Sørensen A. Placental magnetic resonance imaging T2* measurements in normal pregnancies and in those complicated by fetal growth restriction. *Ultrasound Obstet Gynecol*. 2016;47(6):748-754.

114. Huen I, Morris DM, Wright C, Parker GJ, Sibley CP, Johnstone ED, Naish JH. R1 and R2* changes in the human placenta in response to maternal oxygen challenge. *Magn Reson Med*. 2013;70(5):1427-1433.

115. de Rijk EPCT, Van Esch E. The macaque placenta—a mini-review. *Toxicol Pathol*. 2008;36:108S-118S.

116. MARTIN CB, RAMSEY EM. Gross anatomy of the placenta of rhesus monkeys. *Obstet Gynecol*. 1970;36(2):167-177.

117. Wang ZJ, Li S, Haselgrove JC. Magnetic resonance imaging measurement of volume magnetic susceptibility using a boundary condition. 1999.

118. Degner K, Magness RR, Shah DM. Establishment of the Human Uteroplacental Circulation: A Historical Perspective. *Reprod Sci*. 2016;24(5):753-761.

119. Caniggia I, Winter J, Lye SJ, Post M. Oxygen and placental development during the first trimester: implications for the pathophysiology of pre-eclampsia. *Placenta*. 2000;21:S25-S30.

120. Owens JA, Falconer J, Robinson JS. Effect of restriction of placental growth on oxygen delivery to and consumption by the pregnant uterus and fetus. *J Dev Physiol*. 1987;9(2):137-150.

121. Berkley E, Chauhan SP, Abuhamad A. Doppler assessment of the fetus with intrauterine growth restriction. *Am J Obstet Gynecol*. 2012;206(4):300-308.

122. Ludwig KD, Fain SB, Nguyen SM, Golos TG, Reeder SB, Bird IM, Shah DM, Wieben OE, Johnson KM. Perfusion of the placenta assessed using arterial spin labeling and ferumoxytol dynamic contrast enhanced magnetic resonance imaging in the rhesus macaque. *Magn Reson Med*. 2019;81(3):1964-1978.

123. Hutter J, Slator PJ, Jackson L, Gomes AD, Ho A, Story L, O'Muircheartaigh J, Teixeira RP, Chappell LC, Alexander DC, Rutherford MA. Multi-modal functional MRI to explore placental function over gestation. *Magn Reson Med*. 2019;81(2):1191-1204.

124. Mühler MR, Clément O, Salomon LJ, Balvay D, Autret G, Vayssettes C, Cuenod CA, Siauve N. Maternofetal Pharmacokinetics of a Gadolinium Chelate Contrast Agent in Mice. *Radiology*. 2011;258(2):455-460.

125. Sinding M, Peters DA, Frøkjær JB, Christiansen OB, Petersen A, Uldbjerg N, Sørensen A.

Prediction of low birth weight: Comparison of placental T2* estimated by MRI and uterine artery pulsatility index. *Placenta*. 2017;49:48-54.

126. Hirsch AJ, Roberts VHJ, Grigsby PL, Haese N, Schabel MC, Wang X, Lo JO, Liu Z, Kroenke CD, Smith JL, Kelleher M. Zika virus infection in pregnant rhesus macaques causes placental dysfunction and immunopathology. *Nat Commun*. 2018;9(1):263.

127. Lo JO, Schabel MC, Roberts VHJ, Wang X, Lewandowski KS, Grant KA, Frias AE, Kroenke CD. First trimester alcohol exposure alters placental perfusion and fetal oxygen availability affecting fetal growth and development in a non-human primate model. *Am J Obstet Gynecol*. 2017;216(3):302.e1-302.e8.

128. Lo JO, Roberts VHJ, Schabel MC, Wang X, Morgan TK, Liu Z, Studholme C, Kroenke CD, Frias AE. Novel Detection of Placental Insufficiency by Magnetic Resonance Imaging in the Nonhuman Primate. *Reprod Sci*. 2017;25(1):64-73.

129. Silk J, Short J, Roberts J, Kusnitz J. Gestation length in rhesus macaques (Macaca mulatta). *Int J Primatol*. 1993;14(1):95-104.

130. Zhu A, Reeder SB, Johnson KM, Nguyen SM, Fain SB, Bird IM, Golos TG, Wieben O, Shah DM, Hernando D. Quantitative ferumoxytol-enhanced MRI in pregnancy: A feasibility study in the nonhuman primate. *Magn Reson Imaging*. 2020;65:100-108.

131. Saranathan M, Rettmann DW, Hargreaves BA, Clarke SE, Vasanawala SS. DIfferential subsampling with cartesian ordering (DISCO): A high spatio-temporal resolution dixon imaging sequence for multiphasic contrast enhanced abdominal imaging. *J Magn Reson Imaging*. 2012;35(6):1484-1492.

132. Avants BB, Tustison NJ, Song G, Cook PA, Klein A, Gee JC. A reproducible evaluation of ANTs similarity metric performance in brain image registration. *Neuroimage*. 2011;54(3):2033-2044.

133. Yushkevich PA, Piven J, Hazlett HC, Smith RG, Ho S, Gee JC, Gerig G. User-guided 3D active contour segmentation of anatomical structures: Significantly improved efficiency and reliability. *Neuroimage*. 2006;31(3):1116-1128.

134. Blockley NP, Jiang L, Gardener AG, Ludman CN, Francis ST, Gowland PA. Field strength dependence of R1 and R relaxivities of human whole blood to prohance, vasovist, and deoxyhemoglobin. *Magn Reson Med*. 2008;60(6):1313-1320.

135. Myers RE. The gross pathology of the rhesus monkey placenta. *J Reprod Med*. 1972;9(4):171-198.

136. Barker D, Osmond C, Grant S, Thornburg KL, Cooper C, Ring S, Davey-Smith G. Maternal cotyledons at birth predict blood pressure in childhood. *Placenta*. 2013;34(8):672-675.

137. Zhu A, Ludwig KD, Zha W, Nguyen SM, Golos TG, Bird IM, Shah DM, Wieben O, Fain SB, Reeder SB, Hernando D, Johnson KM. Placental functional imaging with endogenous contrast: preliminary comparison of BOLD effect and ASL FAIR in rhesus macaque and human. In: *Proc 26th Annual Meeting ISMRM*; 2017:2915.

138. Yadav BK, Neelavalli J, Krishnamurthy U, Szalai G, Shen Y, Nayak NR, Chaiworapongsa T, Hernandez-Andrade E, Than NG, Haacke EM, Romero R. A longitudinal study of placental perfusion using dynamic contrast enhanced magnetic resonance imaging in murine pregnancy. *Placenta*. 2016;43:90-97.

139. Ingram E, Morris D, Naish J, Myers J, Johnstone E. MR Imaging Measurements of Altered Placental Oxygenation in Pregnancies Complicated by Fetal Growth Restriction. *Radiology*. 2017;285(3):953-960.

140. Ludwig KD, Fain SB, Adamson EB, Nguyen SM, Golos TG, Reeder SB, Bird IM, Wieben OE, Shah DM, Johnson KM. Quantitative ferumoxytol DCE MRI of the primate placenta perfusion domains. In: *Proc 26th Annual Meeting ISMRM*; 2018:4573.

141. Menditto A, Patriarca M, Magnusson B. Understanding the meaning of accuracy, trueness and precision. *Accredit Qual Assur*. 2007;12(1):45-47.